RAMAN INDUCED RESONANCE IMAGING OF TRAPPED ATOMS

by

Thomas Alan Savard

Department of Physics
Duke University

Date:____________________________
Approved:

____
Dr. John E. Thomas, Supervisor

____
Dr. Berndt Müller

____
Dr. Bob D. Guenther

____
Dr. Daniel J. Gauthier

____
Dr. Joshua E. S. Socolar

Dissertation submitted in partial fulfillment of the
requirements for the degree of Doctor of Philosophy
in the Department of Physics
in the Graduate School of
Duke University

1998

ABSTRACT

(Physics)

RAMAN INDUCED RESONANCE IMAGING OF TRAPPED ATOMS

by

Thomas Alan Savard

Department of Physics
Duke University

Date:______________________________
Approved:

Dr. John E. Thomas, Supervisor

Dr. Berndt Müller

Dr. Bob D. Guenther

Dr. Daniel J. Gauthier

Dr. Joshua E. S. Socolar

An abstract of a dissertation submitted in partial fulfillment of
the requirements for the degree of Doctor of Philosophy
in the Department of Physics
in the Graduate School of
Duke University

1998

Abstract

This dissertation describes the development of the first neutral atom trapping apparatus at Duke University and Raman induced resonance imaging of trapped atoms—an imaging technique which provides three-dimensional information about the atomic spatial distribution in the trap. The design and operating principles of the ^{6}Li atom source, laser sources, multi-coil Zeeman slower, and magneto-optic trap used in the experiment are explained. Using Raman induced resonance imaging, the atomic spatial distribution in the magneto-optic trap is imaged with $12\,\mu$m resolution. Changes to the experiment will yield a resolution of $5\,\mu$m—rivaling the best resolution achieved in previous two-dimensional imaging experiments—without the expense of large aperture optics and high resolution cameras.

The position distribution of atoms is acquired by inducing Raman transitions between lithium's ground state hyperfine levels. The quadrupole magnetic field of the MOT causes the Raman transition strength and Raman resonance frequency to vary with position. By measuring the response of the atomic distribution at different Raman pulse frequencies, a spectrum is obtained which depends on the position distribution of the atoms.

Previous images of trapped atoms used CCD cameras to record fluorescence or phase contrast images of the atomic spatial distribution. Because the CCD camera measures only two-dimensional information, the entire depth of the trap was averaged onto a single plane. In Raman induced resonance imaging of the MOT, the number of atoms in concentric ellipsoidal shells is measured. Consequently, Raman induced resonance imaging is ideally suited for probing small centrally located density variations within high density atomic spatial distributions, a regime in which two-dimensional imaging with a camera is unsuitable.

In this dissertation, Raman induced resonance imaging is used to determine the size of the atomic distribution and it's offset relative to the MOT's magnetic field zero point. The center of the atomic cloud is found to be substantially shifted from the magnetic field zero point of the trap. In addition, the work presented here significantly advances the development of single-shot Raman transient imaging techniques that will have wide applications to fundamental measurements of ultracold trapped atoms.

Acknowledgments

I would first like to thank John Thomas for all his guidance and enthusiasm in the completion of this work. John was always there with a thoughtful word of encouragement or a brilliant insight whenever I needed it. I have learned quantum mechanics, machining, mathematics, plumbing, and even some motivational psychology from John—all of which I hope to make use of in the future.

I also must thank Jack Netland, my high school physics teacher, who first introduced me to physics. The fun and enthusiasm he brought to the science classroom had a significant impact on my decision to study physics.

Dean Langley, my advisor at St. John's University, sparked my interest in optics and gave me my first significant research opportunity. Thank you for giving me the opportunity and fostering my desire to explore.

While at Duke I have had the privilege to work with many wonderful people. I would like to thank all those who graduated from my group before me: Pat, Kevin, Jeff, Allan, Carl, Mike, and Zhao. They showed me most of what I know in the lab and didn't give me too hard of a time when I did things wrong. I would especially like to thank Carl Schnurr who has been a

great friend (and sometimes counselor) over the years.

If it weren't for all the help I've had in recent years from Ken O'Hara, Mike Gehm, and especially Stephen Granade, this project would never have been completed. Ken worked with me in the early days and end days of the experiment and built the diode laser and MOT magnet controller (the *Hummer*) used in the experiment. Mike assisted in a variety of ways, either in by assembling parts of the *Hummer*, staying late with me to run the experiment, or drawing up some the figures for this dissertation. For most of the last year, Stephen assisted me daily in running the experiment (even on Christmas Eve!) or by machining some brackets for who knows what. Stephen also got the camera system working and wrote the computer programs for the data analysis. I also want to thank Chris Baird who helped me build the slower. I couldn't have had a better crew helping me with this experiment!

Adam Wax and Zehuang Lu, although not directly involved with my experiment, provided invaluable assistance in times of need. Adam's expertise in heterodyne detection was frequently called upon during the some of the initial experiments and he was always willing to lend a helping hand or optic. During my desperate attempts to fix our ailing dye laser in December, Lu gave us his own dye pump when ours went bad (yes, Coherent, they do go bad!) Their selflessness during the difficult months of the experiment is very much appreciated.

I would also like to thank the Samir Bali who provided insight into dif-

ferent aspects of the experiment, especially toward its conclusion.

Richard Poole, now retired, showed me, with great patience, how to safely use the instruments in the machine shop. With his guidance, I gained the skills to create the apparatus for my experiment. I'm sorry new students won't get to learn from him. I hope he enjoys his retirement free from the distractions of flying bits and chuck keys!

Thanks also to my friends back home—Mike, Scott, and Darin— and my friends and classmates at Duke. Thanks especially to Mike Bergmann, fellow Minnesotan, Johnnie, and Dukie, who helps keep alive the memories of comfortable summers and unbearable winters back in Minnesota.

My parents and family all deserve thanks for keeping me optimistic and encouraging me to pursue my dreams. That's two dreams accomplished, now, and many more to go!

Most importantly, I wish to thank my wife, Lynda, for all her love and support through graduate school. Her patience, faith, and music kept me sane, especially during the last few months. I look forward to spending more time with her and becoming the president of her fan club!

For Lynda, with love

Contents

List of Figures

List of Tables

Chapter 1

Introduction

In 1997, the Royal Swedish Academy of Sciences awarded the Nobel Prize in Physics to William Phillips, Stephen Chu, and Claude Cohen-Tannoudji for the development of techniques to optically cool and trap atoms. Even though their accomplishments are relatively recent—the first three-dimensional cooling was reported by Chu *et al.* in 1985 [1]—their pioneering research in optical forces [1–15] has already led to a profound impact in atomic physics and beyond.

For example, the realization of Bose condensates in trapped atoms has provided low temperature physics with a novel quantum degenerate fluid [16–22] and led to the creation of the first atom laser [23]. Optical tweezers, which are based on the light forces used to cool and trap atoms, are routinely used in the biological sciences to manipulate intracellular objects being examined under microscope. In addition, optical lattices, which confine atoms in the periodic potentials created by optical standing waves, demonstrate long range order and may improve our understanding of more complex systems in solid state physics [24–27]. Moreover, in nuclear physics, the measurement of parity nonconserving transition rates in trapped francium isotopes will explore the electroweak interaction [28,29]. Because trapped atoms provide high density samples, small inhomogeneous broadening, and long interaction times to the researcher, they are an excellent medium for the study of fundamental interactions.

Regardless of the context in which trapped atoms are being studied, one of the most important properties to measure is the atoms' position distribution. For a practical application, consider atoms trapped in a conservative potential. The atoms' position distribution determines the mean energy and temperature of the atoms. In another application, at low enough temperatures, the position distribution provides an interesting means of exploring the quantum statistics of fermions and bosons [30–36]. Thus, the position distribution can be a simple diagnostic or a highly physical means of observing some of the deepest features of quantum mechanics.

This dissertation describes Raman induced resonance imaging of trapped atoms—a technique which provides three-dimensional information about the sample of trapped atoms. A combination of laser beams and magnetic fields is used to create a magneto-optic trap (MOT) [9]. The magnetic field used to create the trap is, in turn, used to create spatially dependent Raman transition strengths and resonance frequencies. When the trapped atoms are probed with a laser beam that induces Raman transitions, the response of the sample depends on the atomic spatial distribution. During the imaging experiment described herein, this response is measured and is used to describe the atomic spatial distribution with 12 μm resolution. Changes to the experiment will yield a resolution of 5 μm—rivaling the best resolution achieved in previous two-dimensional imaging experiments—without the expense of large aperture optics and high resolution cameras. Raman induced resonance imaging is ideally suited for probing small centrally located density variations within high density atomic spatial distributions, a regime in which two-dimensional imaging with a camera is unsuitable. Moreover, since Raman induced resonance imaging measures the atomic spatial distribution with respect to the magnetic field zero of the trap, the technique should prove useful in experiments which are sensitive to magnetic fields.

1.1 Motivation for the Current Work

Currently, the spatial distributions of trapped atoms are measured with charge-coupled device (CCD) cameras. In traps which make use of the spontaneous photon scattering force, the atoms emit a considerable amount of fluorescence which provides a simple mechanism for measuring the spatial distribution. The fluorescence is imaged onto a CCD camera which generates a two dimensional plot of intensity. For low atomic densities, the intensity measurement of each pixel represents the density of atoms integrated along the pixel's line of sight. Density measurements of this type have been performed in a number of experiments [37–43]. However, under certain circumstances, these techniques possess a number of disadvantages.

First, at densities of 10^{11} atoms/cc such as those acquired in magneto-optic traps (MOT) [9, 13, 37, 39, 41, 43, 44] the distribution in the MOT can become optically thick and significantly attenuate the lasers that provide the trapping force. Under these conditions, the fluorescence of the atoms in the center of the distribution will be less intense than that of the atoms at the edge. As a result, the atoms in the center of the trap will not contribute equally to the line of site density measured by the pixel. When the densities become so high that the MOT is noticeably optically thick, the most interesting spatial distributions develop [37, 41, 43].

Townsend *et al.* review the three density regimes attainable in standard MOTs [41]. At low densities, the MOT behaves like an ideal gas confined in a harmonic potential with two different spring constants. As such, the MOT possesses a Gaussian density distribution. The two spring constants are due to the quadrupole magnetic field that is used to create a MOT. Along one axis of the MOT, the quadrupole magnetic field creates a magnetic field gradient that is twice as steep as it is along the other two axes. Using the equipartition theorem, the nominal radius r of the atomic distribution along a particular axis is predicted and measured [37, 39, 41] to go as

$$r = \sqrt{\frac{k_B T}{\kappa}} \tag{1.1}$$

where k_B is the Boltzmann constant, T is the temperature of the distribution, and κ is the spring constant. Thus, in this regime, the trap should have an ellipsoidal shape with the minor and major axes related by $\sqrt{2}$. In this regime, the size of the cloud remains the same regardless of the number of trapped atoms. This low density behavior has been observed by two groups [37, 41].

The low densities described above rarely occur in a typical MOT. Under most circumstances, the density in the MOT is high enough that interactions between the atoms diminish the ideal gas behavior. The interactions are caused by radiation trapping forces [37] which occur when photons are scattered from multiple atoms in the trap. Because the scattered photons from one atom exert radiation pressure on nearby atoms, the atomic density cannot increase indefinitely. As more and more atoms are added to the trap, the trap size increases with an approximately uniform maximum density. Rather than having a Gaussian spatial distribution, the distribution has a flat profile and is approximately spherical. Sesko *et al.* [37] used fluorescent imaging to measure this type of distribution, but Townsend *et al.* [41] noted that the atomic distribution is well approximated by a Gaussian unless small magnetic gradients are applied and trap laser frequency detunings are small. At low trap detunings, however, the condition that photons scatter multiple times in the medium is equivalent to the atoms possessing a minimum amount of optical thickness. Consequently, CCD fluorescence measurements in this regime with small trap detunings may be unreliable.

The third regime for MOT spatial distributions occurs at high densities, large magnetic field gradients and large trap frequency detunings. Using numerical analysis, two groups [45, 46] predicted that a two component distribution will exist in the MOT in this regime. A spatially narrow and dense distribution which arises from strong polarization gradient [14] forces should exist in the low magnetic field region at the center of the trap, surrounded by a large distribution with a much lower density. Two-dimensional fluorescence measurements by Townsend *et al.* [41] and Petrich *et al.* [43] indicated the two-component behavior of the distributions at large detunings and magnetic field gradients.

The size of the central distribution along an axis of the MOT is determined by the frequency dependence of the polarization gradient force which peaks sharply as a function of detuning. In the presence of the magnetic field of the MOT, the Zeeman shift of the cooling transitions determines the detuning at a particular point in space. Thus, at some small distance from the trap center, there is a sharp peak in the confining force of the MOT. If the polarization gradient force peaks at a detuning of Δ_p, the radius of the narrow distribution in that direction will be given by

$$\mu_B \frac{dB_i}{dx_i} x_i = \hbar \Delta_p \tag{1.2}$$

where μ_B is the Bohr magneton, dB_i/dx_i is the magnetic field gradient along the $\hat{\boldsymbol{\imath}}$ axis, and x_i is the displacement. In this regime, since the gradient along one axis of the MOT is twice as high as along the others, the minor and major axes of the atomic distribution are related by a factor of two. Townsend *et al.* observed the appropriate scaling between the axes of the central feature in a MOT over a limited set of data. This regime is characterized by high densities and optical thickness which Townsend *et al.* cited as a limit in their theory and measurement methods.

The problems of optical thickness in fluorescence measurements may be somewhat alleviated by the phase contrast techniques [47] implemented in imaging optically thick Bose condensates [19, 48, 49]. However, this method still uses a CCD camera which integrates the depth of the atomic distribution onto a single plane of information. Small centrally located features may be indistinguishable when averaged in this way.

Helmerson *et al.* [50] performed the only known previous imaging experiment in which the atomic distribution was not measured using line of sight averaging and a CCD camera. They used laser spectroscopy to measure a one-dimensional distribution of atoms in a superconducting magnetic trap. The atoms in the large 25 cm long trap had Zeeman shifts which varied over 600 MHz. By measuring the absorption of a weak probe laser as a function of frequency, the spatial distribution of the atoms was measured. In this technique, the doppler shift limits the resolution to approximately 3.5 mm. While this method provided adequate resolution for the large trap in their experiment, the resolution is clearly inadequate for most traps in use today which have diameters less than their resolution.

Raman induced resonance imaging possesses high resolution and over-

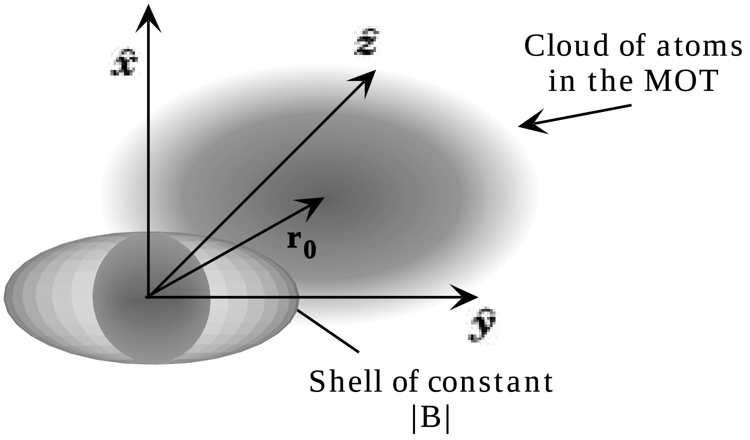

Figure 1.1: The atomic distribution is sampled in shells of constant magnetic field strength. The center of the atomic distribution may be offset from the center of the shells.

comes both the limitations imposed by optically thick samples and line of sight averaging. Resonance imaging is performed with a series of pulses and only a small fraction of the atoms interact with a given pulse. Thus, the effective depth of the atoms is considerably reduced so that optical thickness becomes negligible. In addition, the shape of the atomic distributions that are sampled by each pulse need not be planar. Rather, the sampling shape may be implemented to more accurately match the symmetry of the distribution being measured.

In this dissertation, an optically thick sample of atoms in a magneto-optic trap is imaged using Raman induced resonance imaging. Because the quadrupole magnet field of the MOT is used for the imaging, the atoms are sampled in ellipsoidal shells, as shown in Figure 1.1. This new method of imaging trapped atoms allows one to measure spatial distributions that are inaccessible to fluorescence measurements and inconvenient to measure using line of sight methods. In addition, the atomic spatial distribution is measured with respect to the magnetic field zero of the trap thereby providing important information for experiments which are sensitive to magnetic fields.

The resolution of the technique demonstrated here is $12\,\mu$m which is equivalent to the best resolution [41] obtained in the fluorescence measurements. Changes to the experiment described in this dissertation should yield resolutions of $5\,\mu$m which is limited by the motion of atoms in the trap. With colder atoms, the resolution reaches a limit of 510 Å which can only be improved by increasing the magnetic field gradient in the MOT. In contrast, the best resolution obtained using the phase contrast imaging techniques [19, 48, 49] is $4 - 5\,\mu$m which is near the practical resolution limit imposed on aperture-limited classical optical techniques.

The resonance imaging technique presented in this dissertation can be directly applied to other traps with quadrupole magnetic fields. In particular, a new high-field-gradient quadrupole magnetic trap developed by Vuletic *et al.* adiabatically compresses the atoms in a MOT into a ball less than $200\,\mu$m in diameter [51]. Because of the extremely large magnetic fields used in this trap, absorptive and fluorescence measurements with a CCD camera are not feasible. In the 3×10^5 G/cm gradient of their trap, the resonance imaging would have a resolution of 157 nm immediately after the atoms are adiabatically compressed into the trap. For cooled atoms in their trap, the Raman induced resonance imaging resolution approaches 30 nm. Moreover, the spatial extent of the wavefunction for atoms confined in the ground state of their trap is much less than an optical wavelength. Consequently, if most of the atoms are cooled to the ground state, spatial imaging will require the sub-optical resolution attainable by the techniques developed in this dissertation.

1.2 Raman Induced Resonance Imaging

Previous experiments by our group demonstrated Raman Induced Resonance Imaging (RIRI) in a number of atomic beam experiments [52–54]. Three theoretical papers [36, 55, 56] as well as two review papers [34, 35] have been published on RIRI as well.

1.2.1 Description of Raman Induced Resonance Imaging

To understand how RIRI works, it is worthwhile to review standard resonance imaging techniques. In resonance imaging, an atomic spatial distribution is initially in one initial state $|i\rangle$, as shown in Figure 1.2. The energy of another state, called the final state $|f\rangle$ is shifted using a force field. For example, in the figure, the final state is shifted by a magnetic field gradient. This causes the transition frequency between $|i\rangle$ and $|f\rangle$, $\omega_0(x)$, to vary in space. If an excitation pulse of frequency ω with the appropriate intensity and duration interacts with the atoms, the atoms located at the place where $\omega = \omega_0(x)$ can be placed into the final state. In the figure, this location is denoted by

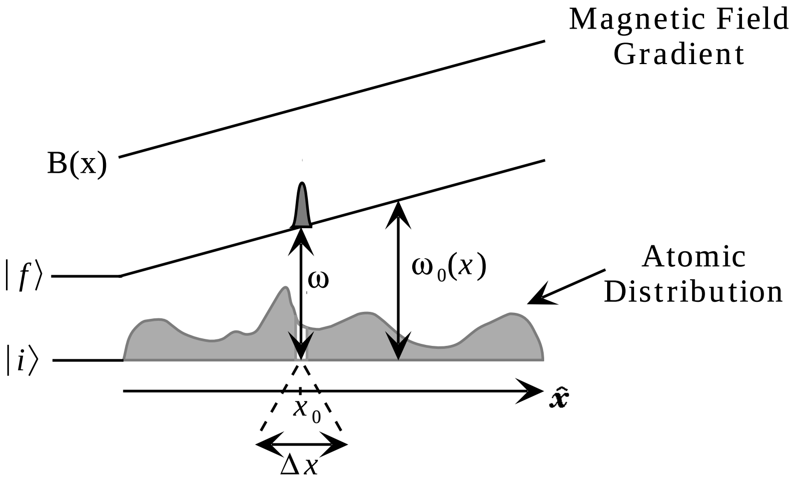

Figure 1.2: Schematic of Raman induced resonance imaging.

x_0. The number of atoms in the final state is detected after the excitation pulse. The number of atoms detected corresponds to the number of atoms in the initial state at x_0 before the pulse. If the atomic distribution is recreated in the initial state, and the excitation pulse is repeated with a different ω, a different set of atoms will be detected in the final state corresponding to a different resonant location x_0.

By repeatedly measuring the sample at different excitation frequencies, the number of atoms that originated in the initial state can be expressed as a function of excitation frequency. Since the resonant location is a well-defined function of excitation frequency, $x_0(\omega, \omega_0)$, the spatial distribution of the atoms can be determined. As shown in Figure 1.2, the resolution of the imaging technique is given by Δx which is simply the width of the distribution that is excited at a particular x_0. The resolution is discussed in

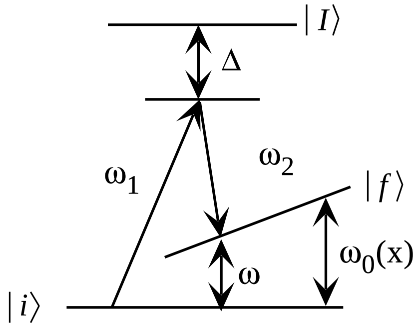

Figure 1.3: Energy level diagram of the Raman transition.

Section 1.2.2.

Raman induced resonance imaging operates with the same principles. Essentially, the only difference between Raman and standard resonance imaging is the method used to create the excitation pulse. As shown in Figure 1.3, the excitation pulse is created by combining two optical fields of frequency ω_1 and ω_2. The difference in the frequency of the two fields, called the Raman difference frequency, acts as the excitation frequency ω of the pulse. In the figure, the difference frequency is given by $\omega = \omega_1 - \omega_2$. The Raman transition, a two-photon process, proceeds through state $|I\rangle$ which is off-resonant with ω_1 and ω_2 by the detuning Δ.

Like most forms of resonance imaging, Raman induced resonance imaging uses a series of Raman pulses with different ω to map out a spatial distribution. We "scan" the Raman transition frequency ω in order to measure the spatial distribution. Scanning is straightforward in an atomic beam because the spatial distribution in the beam remains essentially constant in the lab frame. Perturbations applied to the distribution as a result of the measurement process are carried downstream. New atoms continually repopulate the interesting spatial distribution.

Raman induced resonance imaging may be used in a MOT because the MOT possesses a large trap depth and can also be rapidly recycled. In the lithium MOT, the trap depth is at least 0.5 K. Although the atoms absorb photons during the measurement process, the perturbation is on the order of a few microkelvin, and is negligible compared to the depth of the trap. Consequently, the MOT recycles nearly instantaneously, in a few microseconds.

1.2.2 Spatial Resolution

Three factors limit the spatial resolution of RIRI: spectral resolution, motion of atoms during the Raman transition, and diffraction of the atoms due to localization. I will present heuristic derivations for each of these limits in this section. The precise results depend on the specifics of the particular experiment.

Spectral Resolution

The *spectral* resolution of the Raman transition is one of the three factors limiting the spatial resolution, Δx, of RIRI. The effective linewidth of the Raman transition and the bandwidth of the Raman fields determine the spectral resolution. Because we choose long-lived ground states for $|i\rangle$ and $|f\rangle$, the transition is free from traditional radiative broadening. However, if the detuning from the excited state, Δ, is too small, thus allowing incoherent transitions from the ground states to the excited states, this long lifetime reduces to the incoherent transition time. Usually, we make the detuning large enough to prevent significant population of the excited state. In this limit, the bandwidth of the Raman transition is negligible.

We reduce the bandwidth of the Raman fields using three techniques. First, because the Raman fields copropagate, the Doppler shift due to the atomic motion cancels in ω, the Raman difference frequency. Secondly, we use the same light source and nominal path lengths for both Raman fields so that frequency jitter from the laser source cancels in the Raman difference frequency. Finally, to create the difference frequency, we use standard stable acousto-optic modulators which have a typical stability of 1 kHz in 100 MHz [57]. Because the difference frequency is so stable, the duration T of the Raman pulse usually determines the spectral resolution $\Delta\omega$ as a consequence of Fourier's theorem. Thus,

$$\Delta\omega \approx 1/T \tag{1.3}$$

The spatial resolution due to the spectral resolution can be determined by noting that when the energy shift of $|f\rangle$ varies linearly with position, as shown in Figure 1.2, the energy gradient exerts a uniform force F on $|f\rangle$. Thus, the spatial tuning rate of the Raman resonance frequency is given by the quantity F/h which has units of Hz/cm. It describes how quickly the Raman transition resonance frequency changes as a function of position along the measurement axis. By noting that

$$\Delta\omega = \frac{F}{\hbar}\Delta x, \tag{1.4}$$

the spatial resolution for a pulse of length T can be written as

$$\Delta x = \Delta x_{sp} = \frac{\hbar}{FT}. \tag{1.5}$$

Velocity-Limited Resolution

Atomic motion during the Raman pulses also affects the spatial resolution. If the atoms have a velocity v_x along the measurement axis during the Raman pulse, they will move a distance $v_x T$ during the the measurement. Atoms which were initially out of the resonant region may move into the resonant region during this time. Consequently, the minimum velocity limited resolution Δx_{vel} is given by $\Delta x_{vel} = v_x T$. In this limit, lower velocities and shorter measurement times produce better resolution. However, (1.5) shows that T cannot be made arbitrarily short because the spectral resolution limit will eventually dominate the spatial resolution. By setting $\Delta x_{vel} = \Delta x_{sp}$, one can solve for the ideal measurement time T_{vel} to determine the actual velocity limited resolution.

$$T_{vel} = \left(\frac{\hbar}{v_x F}\right)^{1/2}. \tag{1.6a}$$

Using (1.6a) in the expression for Δx_{vel} gives

$$\Delta x_{vel} = \left(\frac{v_x \hbar}{F}\right)^{1/2}. \tag{1.6b}$$

Acceleration-Limited Resolution

The third limiting factor in the spatial resolution occurs due to diffraction. The diffraction limit is caused by the acceleration of the atoms due to F during the measurement process. By localizing the atoms, we necessarily perturb them with a force. During the measurement time T the atom moves a distance due to acceleration given by $FT^2/2m$, where m is the mass of the atom. Again, the shorter we make T the better, until the spectroscopic resolution is reached. Following the same analysis used in the velocity limit,

$$T_{acc} = \left(\frac{2\hbar m}{F^2}\right)^{1/3} \tag{1.7a}$$

$$\Delta x_{acc} = \left(\frac{\hbar^2}{2mF}\right)^{1/3}. \tag{1.7b}$$

The most fundamental limit to the spatial resolution is the acceleration limit. For a given spatial tuning rate, the acceleration limit is determined for a particular atom. The velocity limited resolution also depends on the spatial tuning rate but may be improved using an atomic beam with better collimation or by additional cooling of atoms in a trap.

In the acceleration limit, Raman Induced Resonance Imaging can, under certain circumstances, be uncertainty-principle limited. To see this, consider the case when the spatially varying potential only shifts one state in the transition; in this case, assume only $|f\rangle$ is shifted. Consequently, the force F will act only on the atom after it is has made the transition from $|i\rangle$ to $|f\rangle$. Because the atom can make the transition to $|f\rangle$ anytime during the duration, T, of the measurement, there is a net uncertainty in the atom's momentum after the measurement, given by $\Delta p = FT$. If the resolution is given by the spectroscopic limit which has been set equal to the velocity- and diffraction-limited resolutions in (1.6) and (1.7), the uncertainty in the position is given by $\Delta x = \hbar/FT$. Thus, the uncertainty product is

$$\Delta p\,\Delta x \approx FT\,\frac{\hbar}{FT} = \hbar. \tag{1.8}$$

For Gaussian Raman pulses, the full quantum mechanical calculation in Ref. [55] shows that (1.8) reduces to $\Delta p\,\Delta x = \hbar/2$ in the ideal case.

1.2.3 The Spatial Resolution Function

For Raman Induced Resonance Imaging, the probability for the atom to be in the final state P_f after the Raman pulse takes a general form. If $\hat{\boldsymbol{x}}$ is the measurement axis, this probability is given by [52, 53, 56]

$$P_f(\omega) = \int dp_x \int dx R(\omega, x, p_x) W_i(x, p_x) \tag{1.9}$$

where ω is the Raman difference frequency, $W_i(x, p_x)$ is the phase space distribution of the atoms in the initial state, and $R(\omega, x, p_x)$ is the resolution function. For each ω, there is some $x = x_0$ where the resolution function peaks sharply. The frequency distribution of the Raman pulses and the shape of the potential gradient determines the exact shape of $R(\omega, x, p_x)$. Since the resolution of the technique may be limited by either the velocity of the atoms or the acceleration of the atoms during the measurement, the momentum of the atoms is necessarily included in R and the complete phase space density $W_i(x, p_x)$ is needed.

Experimentally, we measure the the final state population as a function of the Raman difference frequency. Through careful characterization of the gradient potential, we can relate the Raman difference frequency to the spatial measurement axis. Since the final state population is proportional to the probability $P_f(\omega)$, the measurements of the final state represent this probability as ω is scanned through the possible resonance frequencies.

Given the potential gradient, we can calculate the resolution function, $R(\omega, x, p_x)$. With this resolution function, we can find $W_i(x, p_x)$ with a resolution determined by $R(\omega, x, p_x)$ by fitting the calculated $P_f(\delta)$ to the data.

1.3 Overview of the Current Work

In the current work, Raman Induced Resonance Imaging (RIRI) is used to measure the spatial distribution of lithium atoms in magneto-optic trap.

The atoms originate in an atomic beam with a most probable velocity of 1680 m/s. The atoms with velocities below 1100 m/s are decelerated using counterpropagating radiation to a final velocity near 40 m/s. The slow atoms propagate into a magneto-optic trap (MOT) which binds and cools them to approximately 350 μK and an average velocity of 1 m/s. When the number of trapped atoms reaches an equilibrium, the atomic distribution is measured using resonance imaging in the quadrupole magnetic field provided by the MOT.

While imaging the atoms, the laser beams used in the MOT are momentarily turned off. After the atoms are placed into the initial imaging state, the $|F = 1/2\rangle$ ground state, a Raman pulse with a particular difference frequency induces Raman transitions to the final state, the $|F = 3/2\rangle$ ground state. Due the magnetic field dependence of the Raman transitions, described in Chapter 2, only atoms in the region with the appropriate magnetic field strength make the transition to the final state.

The quadrupole magnetic field of the MOT creates ellipsoidal shells of constant field strength in position space as shown in Figure 1.1. Imbalances between the laser beams used to make the (MOT) frequently cause the atomic cloud to be offset from the magnetic field zero of the MOT as shown. The thickness of each shell corresponds to the resolution, Δx. After the atoms in the shell are placed in the final state, they are detected using resonance fluorescence. Immediately after the fluorescence of the final state is recorded, the MOT trapping beams are turned back on to recycle the trap and the

MOT quickly returns to it's original shape. This measurement process is repeated for different Raman difference frequencies, thereby measuring the fluorescence corresponding to the number of atoms in each ellipsoidal shell in the MOT.

The spectrum of the final state fluorescence as function of Raman difference frequency is compared to a calculated expression for the spectrum. This calculated expression is in the form of the final state probability (1.9) defined in Section 1.2.3. The resolution function defined by (1.9) is derived for an arbitrary magnetic field in Chapter 2 and determined specifically for the quadrupole field of the MOT in Chapter 6. Based on the operating parameters of the magneto-optic trap, the expected form of the atomic density function is used to calculate the theoretical spectrum. Then, this calculated spectrum is fit to the experimentally measured Raman spectrum to obtain spatial information about the atomic cloud. The sensitivity of the Raman spectrum to the atomic spatial distribution allows the size and offset of the trapped atom cloud to be determined. The offset of the cloud is measured relative to the magnetic field zero of the trap.

Our group was required to learn and apply a significant amount of technology to accomplish this experiment. These technologies included:

ultra-high vacuum (UHV) systems A UHV system with ultimate pressures near 5×10^{-11} torr provides long trap decay times for this and future experiments.

a non-standard laser dye Since the cooling transition in lithium occurs at 671 nm, an initially troublesome, yet eventually worthwhile, non-standard dye is required to achieve significant power (over 700 mW) at this wavelength.

a multi-coil Zeeman slower A Zeeman slower permitted deceleration of a lithium beam for loading into a magneto-optic trap. The slower decelerates atoms from 1100 m/s to 40 m/s.

a magneto-optic trap (MOT) The MOT, the workhorse of almost every trapping experiment, captures $\approx 10^8$ atoms and cools them to a few hundred microkelvin and average velocities of 1 m/s.

The work presented here represents an excellent technique for imaging traps which can be recycled quickly like the MOT. Since the technique may be applied to optically thick atomic distributions, Raman induced resonance imaging offers a method of probing dense traps for which traditional fluorescence trap imaging is unsuitable. In addition, resonance imaging allows one to measure the atomic distribution by sampling with a resolution function that matches the trap symmetry. Since this avoids averaging the image across the depth of the trap, Raman induced resonance imaging is particularly useful in exploring small density variations at the center of the atomic distribution.

1.4 Organization of the Dissertation

This dissertation is comprised of seven chapters and one appendix. In Chapter 2, the final state probability (1.9) is calculated for a distribution of ^{6}Li atoms in an arbitrary magnetic field. This is the first calculation of a resolution function that includes multiple Raman transitions and the prospect of three-dimensional imaging. Chapter 3 explains why we chose lithium, specifically ^{6}Li, to use in the experiment. Then, the relevant thermodynamic and electromagnetic properties of lithium and their implications are discussed. In Chapter 4, the cooling and trapping apparatus is described. The chapter details the vacuum system, laser systems, multi-coil Zeeman slower, and magneto-optic trap used in the experiment. The apparatus and procedures used in the imaging phase of the experiment are described in Chapter 5. The results of the imaging experiment are presented and analyzed in Chapter 6. There, the general expression for the final state probability derived in Chapter 2 is applied to the specific quadrupole field of the MOT. An expression for the atomic density distribution is found by fitting the calculated spectra to the data. In Chapter 7, the results of the dissertation are summarized and future applications of Raman induced imaging are discussed. Finally, Appendix A details how the transition dipole moment matrix elements presented in Chapter 3 were calculated.

Chapter 2

Raman Transitions in Magnetic Fields

In the experiment described in Chapter 5, Raman induced resonance imaging is used to measure the spatial distribution of atoms in a magneto-optic trap (MOT). The quadrupole magnetic field of the MOT, described in Section 4.5.2, creates spatially varying Zeeman shifts which correlate the Raman transition frequency of a particular atom with it's location in the magnetic field. Before the measurement, all of the atoms are in one internal state, denoted the initial state. Then, a Raman pulse induces transitions in some atoms from the initial state to a final state. The Raman pulse contains two optical frequencies, the difference of which is called the Raman difference frequency. Only those atoms with a Raman transition frequency near the Raman difference frequency make the transition to the final state. After the Raman pulse, the number of atoms in the final state is detected using resonance fluorescence. This process is repeated for several Raman difference frequencies, creating a Raman spectrum.

The Raman spectrum contains information about the atomic spatial distribution. The number of atoms in the final state at each Raman difference frequency is proportional to the probability that an atom made the transition. The general form for this probability is

$$P_f(\omega) = \int dp_x \int dx R(\omega, x, p_x) W_i(x, p_x) \tag{2.1}$$

as described in Section 1.2.3. The specific expression depends on the magnetic field strength and direction, the bandwidth of the Raman pulse, and the spatial distribution of the atoms. In this chapter, an explicit expression for the final state probability is derived. As a function of Raman difference frequency, this probability is the Raman spectrum measured in the experiment.

This theory chapter consists of two sections. In the first section, the semiclassical amplitude equations for a Raman transition are derived. I treat the center of mass motion of the atom classically because the experiment is operated in the spectral resolution limit in which the bandwidth of the Raman pulse and the Raman transition linewidth determine the resolution. Thus, the atom's motion during the Raman pulse has a negligible effect on its final state probability. At the end of the first section, an approximate expression for the three-level atom Raman spectrum is obtained. The second section of this chapter extends the probability derived in the first section to account for the nonuniform magnetic field of the MOT and the spatial distribution of the atoms. The result is Raman spectrum in the form of (2.1).

2.1 Raman Transitions in a Three level Atom

Figure 2.1 depicts the energy levels and optical frequencies involved in the Raman transition. The atom is initially in state $|i\rangle$. The Raman pulse contains two optical fields with frequencies ω_1 and ω_2 and couples $|i\rangle$ to $|f\rangle$ through the intermediate state $|I\rangle$. As shown, the optical fields are detuned from resonance with $|I\rangle$ by Δ_1 and Δ_2, respectively, which are approximately equal. The initial and final state internal energies are given by $\hbar\omega_i$ and $\hbar\omega_f$, respectively. The notation ω_{nm} implies $\omega_n - \omega_m$. Thus,

$$\omega_{fi} = \omega_f - \omega_i \tag{2.2}$$

$$\omega_{12} = \omega_1 - \omega_2. \tag{2.3}$$

Using this picture, an approximate solution for the atom's final state probability is calculated. The resulting probability, expressed as a function of the optical field strengths and the Raman detuning, $\delta = \omega_{12} - \omega_{fi}$, can be viewed as an expression of a three-level atom Raman spectrum.

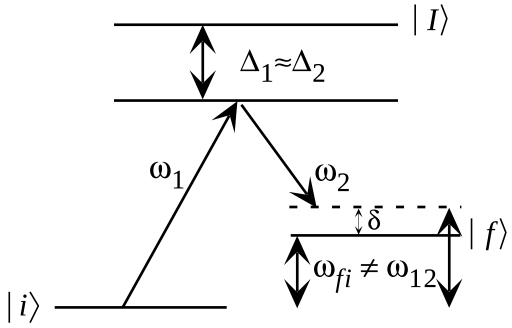

Figure 2.1: Non-resonant Raman transitions in a three-level atom.

2.1.1 The Three-Level Amplitude Equations

The atomic wavefunction $|\psi(t)\rangle$ may be expressed generally as

$$|\psi(t)\rangle = \sum_{m=\{i,f,I\}} A_m(t)e^{-i\omega_m t}|m\rangle \tag{2.4}$$

where $|m\rangle$ is an internal atomic state and $\hbar\omega_m$ is the internal energy of $|m\rangle$. This section determines the amplitude evolution equations for A_i, A_f, and A_I for the three-level atom during the Raman pulse.

The semi-classical Hamiltonian describing the internal states of the atom $|m\rangle$ and their coupling to Raman electric field $\boldsymbol{E}$ is given by

$$H = H_0 - \boldsymbol{\mu} \cdot \boldsymbol{E} \tag{2.5}$$

where $H_0|m\rangle = \hbar\omega_m|m\rangle$ and $\boldsymbol{\mu}$ is the dipole moment of the atom induced by

$\boldsymbol{E}$. The electric field is described by

$$\boldsymbol{E} = \frac{\boldsymbol{E_1}}{2} e^{-i\omega_1 t} + \text{c.c.} + \frac{\boldsymbol{E_2}}{2} e^{-i\omega_2 t} + \text{c.c.} \tag{2.6}$$

Due to a combination of selection rules and detuning, $|i\rangle$ and $|f\rangle$ are only coupled to $|I\rangle$ via $\boldsymbol{E_1}$ and $\boldsymbol{E_2}$, respectively.

The wavefunction for the internal state of the atom must evolve according to the Schrödinger equation:

$$H|\psi(t)\rangle = i\hbar \frac{\partial}{\partial t} |\psi(t)\rangle. \tag{2.7}$$

By projecting the state $\langle n|$ onto (2.7) and making the rotating wave approximation, we get the following equations of motion for the amplitudes:

$$\dot{A}_i(t) = -\frac{\Omega_1^*}{2i} A_I(t) e^{i\Delta_1 t} \tag{2.8a}$$

$$\dot{A}_f(t) = -\frac{\Omega_2^*}{2i} A_I(t) e^{i\Delta_2 t} \tag{2.8b}$$

$$\dot{A}_I(t) = -\frac{\Omega_1}{2i} A_i(t) e^{-i\Delta_1 t} - \frac{\Omega_2}{2i} A_f(t) e^{-i\Delta_2 t} - \frac{\Gamma}{2} A_I(t). \tag{2.8c}$$

Here, $\Delta_1 = \omega_1 - \omega_{Ii}$ and $\Delta_2 = \omega_2 - \omega_{If}$. Also in (2.8) are the optical Rabi frequencies $\Omega_1 = \boldsymbol{\mu_{Ii}} \cdot \boldsymbol{E_1}/\hbar$ and $\Omega_2 = \boldsymbol{\mu_{If}} \cdot \boldsymbol{E_2}/\hbar$. The $\Gamma/2$ term was added heuristically in (2.8c) to provide a linewidth for the optical transitions and to allow the population in the intermediate (excited) state to decay.

2.1.2 Reduction to a Two-Level System

To reduce the three amplitude equations to two, we first assume a solution to (2.8c) of the form $A_I(t) = a_1(t)e^{-i\Delta_1 t} + a_2(t)e^{-i\Delta_2 t}$. Inserting this into (2.8c) and separating the different frequency components gives

$$\boxed{\dot{a}_1(t)} + a_1(t)\left(\frac{\Gamma}{2} - i\Delta_1\right) = -\frac{\Omega_1}{2i}A_i(t) \tag{2.9a}$$

$$\boxed{\dot{a}_2(t)} + a_2(t)\left(\frac{\Gamma}{2} - i\Delta_2\right) = -\frac{\Omega_2}{2i}A_f(t) \tag{2.9b}$$

We assume that $\Delta_1, \Delta_2 \gg \Omega_n, \Gamma$. Since a_1 and a_2 vary at rates on the order of Ω_n, the optical Rabi frequencies, $\Delta_1 a_1 \gg \dot{a}_1$ and $\Delta_2 a_2 \gg \dot{a}_2$. Thus, we may neglect the boxed terms to obtain an approximate expression for $A_I(t)$. This approximate solution is

$$A_I(t) \approx -A_i(t)\frac{\Omega_1}{2i\left[\frac{\Gamma}{2} - i\Delta_1\right]}e^{-i\Delta_1 t} - A_f(t)\frac{\Omega_2}{2i\left[\frac{\Gamma}{2} - i\Delta_2\right]}e^{-i\Delta_2 t}. \tag{2.10}$$

Inserting this approximate solution for $A_I(t)$ into (2.8a) and (2.8b) gives

$$\dot{A}_i(t) = \frac{-|\Omega_1|^2}{\Gamma^2 + 4\Delta_1^2}\left[\frac{\Gamma}{2} + i\Delta_1\right]A_i(t) - \frac{\Omega_1^*\Omega_2}{\Gamma^2 + 4\Delta_2^2}\left[\frac{\Gamma}{2} + i\Delta_1\right]A_f(t)e^{-i(\Delta_2 - \Delta_1)t} \tag{2.11a}$$

$$\dot{A}_f(t) = \frac{-|\Omega_2|^2}{\Gamma^2 + 4\Delta_2^2}\left[\frac{\Gamma}{2} + i\Delta_2\right]A_f(t) - \frac{\Omega_2^*\Omega_1}{\Gamma^2 + 4\Delta_1^2}\left[\frac{\Gamma}{2} + i\Delta_2\right]A_i(t)e^{-i(\Delta_1 - \Delta_2)t}. \tag{2.11b}$$

The $\Gamma/2$ terms in (2.11) describe spontaneous transitions from off resonant excitation of $|I\rangle$. Because we have assumed that $\Delta_1, \Delta_2 \gg \Gamma$, we will neglect these terms in the calculation of the Raman spectrum.

The light shift ν_m [58] and Raman Rabi frequency β are defined as

$$\nu_m = \frac{|\Omega_m|^2 \Delta_m}{\Gamma^2 + 4\Delta_m^2} \tag{2.12}$$

$$\beta = -\frac{2\Omega_1^* \Omega_2 \Delta_2}{\Gamma^2 + 4\Delta_2^2}. \tag{2.13}$$

In the limit where $\Delta_1 \approx \Delta_2 \equiv \Delta \gg \Gamma$ these reduce to

$$\nu_m = \frac{|\Omega_m|^2}{4\Delta} \tag{2.14}$$

$$\beta = -\frac{\Omega_1^* \Omega_2}{2\Delta}. \tag{2.15}$$

Using (2.14) and (2.15), we can rewrite (2.11) as

$$\dot{A}_i(t) = -i\nu_1 A_i(t) + \frac{i\beta}{2} A_f(t) e^{i\delta t} \tag{2.16a}$$

$$\dot{A}_f(t) = -i\nu_2 A_f(t) + \frac{i\beta^*}{2} A_i(t) e^{-i\delta t} \tag{2.16b}$$

where $\Delta_1 - \Delta_2 = \omega_{12} - \omega_{fi} \equiv \delta$, the Raman detuning.

The light shift terms in (2.16) simply cause a change in the Raman resonance frequency, as seen by replacing $A_i(t)$ with $a_i(t)e^{-i\nu_1 t}$ and $A_f(t)$ with $a_f(t)e^{-i\nu_2 t}$. After we perform this substitution, the amplitude equations become

$$\dot{a}_i(t) = \frac{i\beta}{2} a_f(t) e^{i(\delta - \boxed{\nu_2 - \nu_1})t} \tag{2.17a}$$

$$\dot{a}_f(t) = \frac{i\beta^*}{2} a_i(t) e^{-i(\delta - \boxed{\nu_2 - \nu_1})t}. \tag{2.17b}$$

For imaging experiments, the two light shifts be made equal everywhere in the sample, making the boxed terms zero. This is accomplished by using an intensity ratio for the optical fields in the Raman pulse such that $\nu_1 = \nu_2$. Without balanced light shifts in the sample, the finite size of the Raman pulse beam would lead to an unwanted spatial dependence in the Raman transition frequency, in addition to the desired spatial dependency provided by the applied potential.

Now that the intermediate state $|I\rangle$ has been adiabatically eliminated, the Raman transition can be viewed in a two-level atom picture. Neglecting the boxed terms in (2.17), the Hamiltonian which describes the two level system is given by

$$H = H_0 - \left\{ \frac{\hbar\beta}{2} e^{-i\omega_{12}t} |i\rangle\langle f| + \text{H.C.} \right\} \tag{2.18}$$

where H_0 is still the internal atomic Hamiltonian as defined in (2.5). In this expression for the two-level Hamiltonian, we see the Raman transition operator. In Section 2.2, we consider rotations to this operator due to a rotating quantization axis. The varying magnetic field direction in the MOT's quadrupole field leads to this rotation.

2.1.3 The Final State Probability

With (2.17), we may solve for the final state probability after the Raman pulse, $|A_f(t \to \infty)|^2$. First, we will solve the resonant $\delta = 0$ case to determine how the final state probability depends on the Rabi frequency and pulse duration. Then, using first order perturbation theory, we will solve the non-resonant case to determine how the final state probability depends on the detuning δ. A combination of the two results provides an approximate solution for the final state probability that simplifies the numerical analysis.

If we set $\delta = 0$ in (2.17), the equations reduce to a simple set of differential equations. Taking the time derivative of (2.17) with $\delta = 0$, we get

$$\ddot{a}_i(t) = i\frac{\beta}{2}a_f'(t) \tag{2.19a}$$

$$\ddot{a}_f(t) = i\frac{\beta^*}{2}a_i'(t). \tag{2.19b}$$

Combining (2.17) and (2.19), the differential equation for the final state amplitude becomes

$$\ddot{a}_f(t) + \frac{|\beta|^2}{4}a_f(t) = 0. \tag{2.20}$$

With the initial condition that $a_f(t) = 0$, the solution is $a_f(t) = \sin(|\beta|t/2)$. For a square Raman pulse of length τ in the interval $(-\infty < t < \infty)$, the final state probability is given by

$$P_f(t \to \infty) = |A_f(t \to \infty)|^2 = \sin^2 \frac{|\beta|\tau}{2}. \tag{2.21}$$

The quantity $|\beta|\tau$ is known as the *pulse area* and quantifies the coherent transitions from $|i\rangle$ to $|f\rangle$. A pulse area of $\pi/2$ transfers half the population of $|i\rangle$ to $|f\rangle$ while a π pulse transfers all of it. For Raman Induced Resonance Imaging, a π pulse is usually used to transfer all of the atoms to $|f\rangle$ at the resonant location.

The nonresonant solution may be solved exactly, but to simplify the analysis, we use perturbation theory and assume that $a_i(t) \approx 1$. Then, (2.17b) may be integrated. For a square Raman pulse of length τ (centered at $t = 0$ for convenience), the solution is:

$$a_f(t \to \infty) = \int_{-\tau/2}^{\tau/2} dt' \frac{i\beta^* t'}{2} e^{-i\delta t'} = \frac{i\beta^*}{\delta} \sin \frac{\delta\tau}{2}. \tag{2.22}$$

so that

$$P_f(t \to \infty) = \frac{\tau^2 |\beta|^2}{4} \operatorname{sinc}^2 \frac{\delta\tau}{2} \tag{2.23}$$

where

$$\operatorname{sinc} x = \frac{\sin x}{x}. \tag{2.24}$$

As one would expect, the nonresonant solution evaluated at $\delta = 0$ approximately equals the resonant solution when $|\beta|\tau \ll 1$. Thus, for small pulse areas, we may view (2.23) as the product of (2.21) with a sinc lineshape function that depends on the detuning δ. However, Marable and Welch [59, 60] found that for pulse areas as large as 4π, the lineshape remains approximately constant. Therefore, we will combine the resonant and nonresonant solutions to form an approximate general solution given by

$$P_f(\delta) = \sin^2 \frac{|\beta|\tau}{2} \operatorname{sinc}^2 \frac{\delta\tau}{2} \tag{2.25}$$

Only the magnitude of the Raman Rabi frequency determines the value of the final state probability. Rather than continuing to write the magnitude notation, henceforth $|\beta|$ will be replaced by β to denote the Rabi frequency magnitude.

As a function of the Raman detuning, δ, the final state probability in (2.25) represents a Raman spectrum. We now have an approximate solution for the final state probability as a function of pulse area and detuning. In the next section, we will modify (2.25) for multilevel atoms in a spatially varying magnetic field.

2.2 Raman Transitions of ^{6}Li Atoms in a Magnetic Field

So far we have only considered the Raman transition in a simple three-level atom. To image the atoms, perpendicular linearly polarized Raman fields are used to induce Raman transitions within ^{6}Li's $J = 1/2$ ground state in the quadrupole magnetic field of the MOT. In this section, I modify the final state probability (2.25) to account for the multiple levels in lithium and the presence of the magnetic field.

2.2.1 Multiple Two-Level Systems

The two levels in the ^{6}Li ground state, as shown in Figure 2.2, are split by 228 MHz. Each F-level contains $2F + 1$ degenerate m_F-levels. Thus, the initial state $|i\rangle$ contains two levels and the final state $|f\rangle$ contains four levels. The presence of a magnetic field removes the degeneracy of the m_F levels through the Zeeman shift as shown. The arrows denote the possible Raman transitions from $|i\rangle$ to $|f\rangle$.

The intermediate state $|I\rangle$ is the excited state $J' = 3/2$ level which contains three F'-levels. In this section, we will consider only how the multiple initial and final states affect the final state probability. The effect of the multiple intermediate states is treated in Section 3.3 where the Raman Rabi frequencies and light shifts are calculated.

In general, the selection rule $\Delta m = 0, \pm 1, \pm 2$ governs a Raman transition

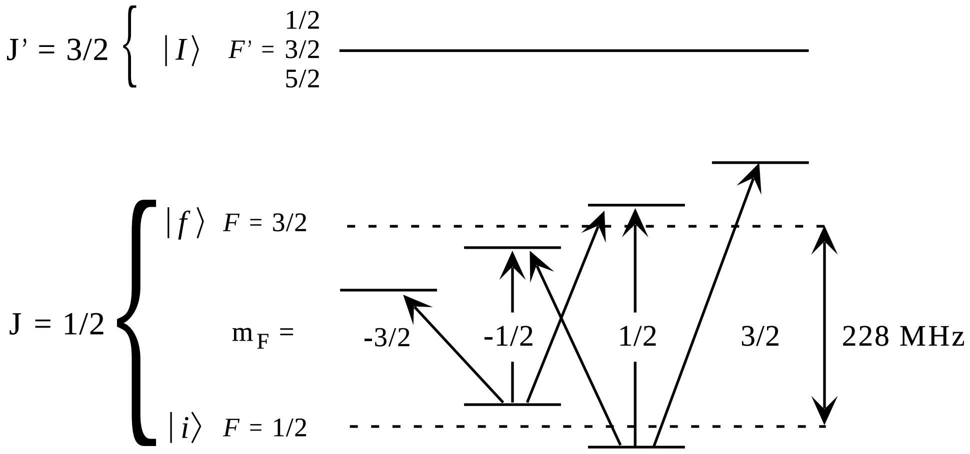

Figure 2.2: Possible Raman transitions within the $J = 1/2$ ground state of ^{6}Li in the presence of a magnetic field.

since it is a two photon process where one photon is absorbed and one is emitted. To understand why $\Delta m = \pm 2$ transitions are not allowed in ^{6}Li (as well as other $J = 1/2$ ground state atoms), we can consider the two-photon process in terms of tensor operators. The combination of two one-photon processes creates three possible tensor operators. The overall interaction is a product of atom operators and fields that yields either a scalar, vector, or outer product operator. The scalar operator which is proportional to to $\boldsymbol{E_1} \cdot \boldsymbol{E_2^*}$ is identically zero in this case since the polarizations of the electric fields are perpendicular. However, the rank-one vector operator is proportional to $\boldsymbol{E_1} \times \boldsymbol{E_2^*}$ and is nonzero, leading to the Raman transitions shown in Figure 2.2. In addition, a rank-two operator may also be formed which is proportional to the outer product $\boldsymbol{E_1} \otimes \boldsymbol{E_2^*}$. However, because the Raman transition occurs within the $J = 1/2$ ground state, the rank two Raman transition is not allowed. The Raman Rabi frequency, as calculated in Section 3.3, for the $\Delta m = \pm 2$ transitions is identically zero. This occurs because no vector combination of 1/2 and 2 results in 1/2. Consequently, only $\Delta m = 0, \pm 1$ transitions occur in the $J = 1/2$ ground state.

In the experiment, Raman transitions from $|i\rangle = |F = 1/2\rangle$ to $|f\rangle = |F = 3/2\rangle$ are induced. As shown in the Figure 2.2, in the presence of the magnetic field, these transitions occur at different frequencies. If the magnetic field splits the Raman transition by more than the Raman transition linewidth, only one transition is resonant for each atom at any particular Raman difference frequency. In this limit, we may treat each Raman transition as a separate two-level atom process.

In deriving (2.25), we made a number of assumptions about the two-level process, most notably that the boxed light shift terms in (2.17) cancel over the sample. In the multi-level picture shown in Figure 2.2, the Raman fields couple two initial states to four final states. To assure that the final state probability only depends on the atom's position in the magnetic field, the light shifts for each level must be equal. Since the experiment uses linearly polarized optical fields in the Raman pulse, this is remarkably easy to accomplish.

The light shift of ^{6}Li's ground states in the presence of linearly polarized light is a scalar quantity and is independent of m. We can understand why this occurs by exploring the physical mechanism of the light shift. The expressions for the light shift (2.14) and Raman Rabi frequency (2.15) show the similarity of the two processes. Whereas a Raman transition uses stimulated absorption from one electric field and stimulated emission into another field to couple two different states, the light shift describes the effect of stimulated absorption and emission from the same field on one state. Both Raman transitions and the light shift occur as a result of two-photon processes.

If we consider the light shift in the tensor operator viewpoint, the scalar behavior of the light shift is easily understood. As explained when we considered the rank-two Raman tensor operator, the rank-two light shift operator cannot operate in the $J = 1/2$ basis. Since the light shift results from a two-photon process from the same linearly polarized electric field, the rank-one operator proportional to $\boldsymbol{E_m} \times \boldsymbol{E_m^*}$ is identically zero. Thus, only the scalar operator formed from the dot product produces the light shift. Consequently, the light shift is independent of m_F. Thus, the light shifts of all the final states are identical and the light shifts of all the initial states are identical. To create equal light shifts for all of the final and initial states, the ratio of the intensities of $\boldsymbol{E_1}$ and $\boldsymbol{E_2}$ are adjusted as described in Sections 2.1.2 and 3.3.

Since the light shifts of each state in every possible Raman transition cancel, the two-level probability (2.25) describes each transition independently as long as the magnetic field is large enough to resolve each transition. For an individual atom, this corresponds to the condition the Raman transitions are separated in frequency more than the linewidth of the Raman transitions. Since the magnitude of the MOT's quadrupole field continually increases over the range of the atomic distribution from a central magnetic field zero point, the multiple two-level approximation holds as long as the atom is sufficiently removed from the magnetic field zero.

In our experiments, atoms more than $18\,\mu$m from the magnetic center may be treated by this approximation. Note that the magnetic field center does not necessarily correspond to the center of atomic distribution. Since the radius of the atomic distribution is approximately $350\,\mu$m, the fraction of atoms that may not be treated in this approximation goes as $(18/350)^3$ which is less than one percent. Consequently, the contribution these atoms make to the final state population may be neglected in the calculation of the Raman spectrum.

2.2.2 Magnetic Field Dependence of the Raman Spectrum

The previous section explained why each of the Raman transitions shown in Figure 2.2 may be treated independently. Before the measurement, the initial state is prepared by equally populating both $|F = 1/2, m_F = -1/2\rangle$ and $|F = 1/2, m_F = 1/2\rangle$. Depending on the atom's position in the quadrupole magnetic field, it may make any one of the Raman transitions shown in Figure 2.2. Each transition has a separate Raman Rabi frequency and detuning which depend on the atom's position in the magnetic field. Thus, the

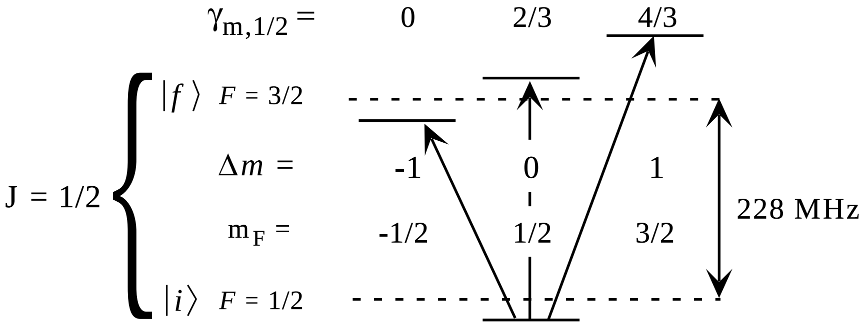

Figure 2.3: Tuning of the Raman transitions in a magnetic field.

probability expressed in (2.25) may be rewritten as

$$P_f(t \to \infty, \delta) = \frac{1}{2} \sum_i \sin^2(\frac{\beta_i(\boldsymbol{r})\tau}{2}) \operatorname{sinc}^2(\frac{(\delta - \delta_i^B(\boldsymbol{r}))\tau}{2}) \tag{2.26}$$

where i is summed over each of the transitions. The factor of one-half occurs because the atom may be in either initial state. The Raman Rabi frequencies $\beta_i(\boldsymbol{r})$ depend on the *direction* of the magnetic field and the detunings $\delta_i^B(\boldsymbol{r})$ depend on the *magnitude* of the magnetic field. Since the number of atoms that make the transition to the final state depends on both magnetic field direction and strength, the Raman spectrum contains more than one-dimensional information.

The sum in (2.26) contains contributions from both initial states. To explore the features of (2.26), it is instructive to first look at the contribution to the final states from just one of the initial states. For now, consider only atoms in the initial state $|F = 1/2, m_F = 1/2\rangle$ as shown in Figure 2.3. The possible transitions correspond to changes in m_F of

$\Delta m = -1, 0, +1$. From this initial state, atoms can make transitions to $|F = 3/2, m_F = -1/2,\ 1/2,\ 3/2\rangle$. Thus, the contribution to the final states from $|F = 1/2, m_F = 1/2\rangle$ may be written as

$$P_f(\boldsymbol{r}, \delta) = \frac{1}{2} \sum_{m=-\frac{1}{2},\frac{1}{2},\frac{3}{2}} \sin^2(\frac{\beta_{m,1/2}(\boldsymbol{r})\tau}{2}) \operatorname{sinc}^2(\frac{(\delta - \delta^B_{m1/2}(\boldsymbol{r}))\tau}{2}) \tag{2.27}$$

where m represents the m_F of the final state.

The shifts of the Raman transitions in the presence of a magnetic field, $\delta^B_{m,1/2}(\boldsymbol{r})$, are calculated inSection 3.3 and may be expressed as

$$\delta^B_{m,1/2}(\boldsymbol{r}) = \gamma_{m,1/2}\mu_B B(\boldsymbol{r})/\hbar \tag{2.28}$$

where $\gamma_{m,1/2}$ is given in Figure 2.3, μ_B is the Bohr magneton, and $B(\boldsymbol{r})$ is the magnitude of the magnetic field. From Figure 2.3, we can see that there is one magnetic field independent Raman transition for $m = -1/2$. This Raman transition maximizes its contribution to the spectrum (2.27) at $\delta = 0$. The other two Raman transitions maximize their contributions to the spectrum when the Raman detuning, δ, is positive.

The effect of the magnetic field on the Raman Rabi frequencies, $\beta_{m,1/2}(\boldsymbol{r})$, in (2.27) is a bit more subtle than the effect on the transition frequencies. In the lab frame, the Raman field polarizations are defined as $\{\hat{\boldsymbol{x}},\ \hat{\boldsymbol{y}}\}$. The rank one operator that forms from the cross product of these two fields is proportional to $\hat{\boldsymbol{x}} \times \hat{\boldsymbol{y}} = \hat{\boldsymbol{z}}$ which corresponds to the T^1_0 operator. Thus, in

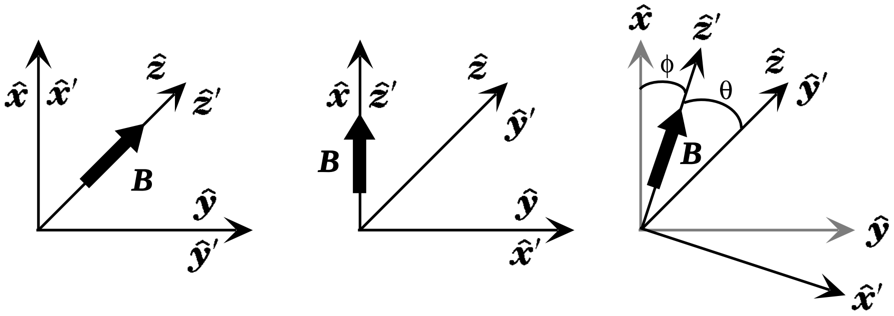

Figure 2.4: The effect of the magnetic field on the quantization axis in the atom's frame.

the absence of a magnetic field, this polarization combination causes $\Delta m = 0$ transitions in the lab frame. However, the atoms may view these polarizations as any perpendicular combination of fields, such as $\{\hat{\boldsymbol{x}}, \hat{\boldsymbol{z}}\}$ which causes both $\Delta m = -1$ and $\Delta m = +1$ transitions. Regardless of how the atom sees the polarizations, the number of atoms that make the transition from $F = 1/2$ to $F = 3/2$ will be the same because the lab and atom frames are equivalent in the absence of a magnetic field.

The presence of a local magnetic field serves to define a quantization axis. Figure 2.4 shows how the magnetic field determines the quantization axis in the atom frame. The lab frame coordinates are unprimed and the atom frame coordinates are primed. In the lab frame, the Raman fields are polarized $\{\hat{\boldsymbol{x}}, \hat{\boldsymbol{y}}\}$ and propagate along the $\hat{\boldsymbol{z}}$ axis. If the local magnetic field $\boldsymbol{B}$ points along $\hat{\boldsymbol{z}}$, the atom experiences the Raman fields as defined in the lab. Thus, an atom in this magnetic field is coupled to $|f\rangle$ by a $\Delta m = 0$ transition. However, if the local magnetic field points along the lab $\hat{\boldsymbol{x}}$ direction, the atom views the Raman field polarizations as $\{\hat{\boldsymbol{z}}$', $\hat{\boldsymbol{x}}$'$\}$. In this local field,

$|i\rangle$ is coupled to $|f\rangle$ by $\Delta m = \pm 1$ transitions. At an arbitrary local field direction, the atoms make a combination of $\Delta m = 0, \pm 1$ transitions.

The angles $\theta(\boldsymbol{r})$ and $\phi(\boldsymbol{r})$ in Figure 2.4 are defined with respect to the lab frame coordinate system and depend on the direction of the local field at the point of interest. The following expressions define the the angles:

$$\cos\theta(\boldsymbol{r}) = \frac{B_z(\boldsymbol{r})}{\sqrt{(B_x(\boldsymbol{r})^2 + B_y(\boldsymbol{r})^2 + B_z(\boldsymbol{r})^2)}} \tag{2.29a}$$

$$\sin\theta(\boldsymbol{r}) = \frac{\sqrt{B_x(\boldsymbol{r})^2 + B_y(\boldsymbol{r})^2}}{\sqrt{B_x(\boldsymbol{r})^2 + B_y(\boldsymbol{r})^2 + B_z(\boldsymbol{r})^2}} \tag{2.29b}$$

$$\cos\phi(\boldsymbol{r}) = \frac{B_x(\boldsymbol{r})}{\sqrt{B_x(\boldsymbol{r})^2 + B_y(\boldsymbol{r})^2}} \tag{2.29c}$$

$$\sin\phi(\boldsymbol{r}) = \frac{B_y(\boldsymbol{r})}{\sqrt{B_x(\boldsymbol{r})^2 + B_y(\boldsymbol{r})^2}}. \tag{2.29d}$$

While the Raman fields remain constant in the lab, the quantization axis rotates by the angles defined in (2.29). Thus, we can determine the effective $\beta_{i,1/2}(\boldsymbol{r})$ for the transitions in the atom frame by considering rotations of the Raman transition operator as expressed in (2.18). Since we define the Raman polarizations as $\{\hat{\boldsymbol{x}},\ \hat{\boldsymbol{y}}\}$ in the lab, the unrotated operator makes $\Delta m = 0$ transitions. For this $\Delta m = 0$ transition the Raman Rabi frequency, as shown in Section 3.3, is given by $\beta_{1/2,1/2} = 2\sqrt{2}\beta_0/9$ where β_0 is defined in (3.18).

Using the spherical tensor operator notation $T(k, q)$ where l describes the operator's rank and q describes the $\hat{\boldsymbol{z}}$-component of the operator's angular momentum, we define $T(1, 0) = \beta_{1/2,1/2}$. In terms of the matrix elements in the rotated basis, $T'(1,q)$, $T(1,0)$ may be expressed as [61]

$$T(1,0) = \sum_q T'(1,q)\mathcal{D}^1_{q,0}(\boldsymbol{r}) \tag{2.30}$$

where

$$\mathcal{D}^1_{q,0}(\boldsymbol{r}) = (-1)^q \left(\frac{4\pi}{3}\right)^{1/2} Y_{1,q}(\theta(\boldsymbol{r}), \phi(\boldsymbol{r})) \tag{2.31}$$

and the $Y_{1,q}$ are the spherical harmonics. The angles $\theta(\boldsymbol{r})$ and $\phi(\boldsymbol{r})$ represent the rotation of the quantization axis as shown in Figure 2.4 and are defined by (2.29). Expanding (2.30) using (2.31), we get

$$T(1,0) = T'(1,0)\cos\theta + \frac{1}{\sqrt{2}}T'(1,-1)\sin\theta + \frac{1}{\sqrt{2}}T'(1,1)\sin\theta. \tag{2.32}$$

Since only the magnitude of the Raman Rabi frequency determines the final state probability, all phase terms in $\phi(\boldsymbol{r})$ are left out of the expression. Each of the terms in (2.32) are operators which couple the initial state to one of the three final states as shown in Figure 2.3. Since (2.32) must be true for all θ, setting $\theta = 0$ gives $T'(1,0) = T(1,0) = \beta_{1/2,1/2} = 2\sqrt{2}\beta_0/9$.

The Wigner-Eckart Theorem (A.1) can be used to determine the remaining matrix elements of the rotated $T'(1,q)$ operator that couple $|F = 1/2, m_F = 1/2\rangle$ to the appropriate state in $F = 3/2$. Using (A.1) with the known matrix element $T'(1,0) = 2\sqrt{2}\beta_0/9$, the reduced operator can be determined and is given by $\langle F = 3/2||T'(1)||F = 1/2\rangle = 4\sqrt{3}\beta_0/9$. By reapplying (A.1) with the reduced matrix element, we find that $T'(1,-1) = 2\beta_0/9$ and $T'(1,1) = 2\sqrt{3}\beta_0/9$.

Using the results of the (2.32), expressions for the $\beta_{i,1/2}(\boldsymbol{r})$ in the rotated frame may be written as

$$\beta_{-1/2,1,2}(\boldsymbol{r}) = \frac{1}{\sqrt{2}}T'(1,-1)\sin\theta = \frac{\sqrt{2}}{9}\beta_0\sin\theta \tag{2.33a}$$

$$\beta_{1/2,1,2}(\boldsymbol{r}) = T'(1,0)\cos\theta = \frac{2\sqrt{2}}{9}\beta_0\cos\theta \tag{2.33b}$$

$$\beta_{3/2,1,2}(\boldsymbol{r}) = \frac{1}{\sqrt{2}}T'(1,1)\sin\theta = \frac{\sqrt{6}}{9}\beta_0\sin\theta. \tag{2.33c}$$

Expressions (2.27), (2.28) and (2.33) completely specify the contributions to the final state from $|F = 1/2, m_F = 1/2\rangle$. The contributions from the other initial state can be treated similarly using the results of Section 3.3 contained in Tables 3.1 and 3.2.

2.2.3 Raman Spectrum of ^{6}Li in a Magnetic Field

Combining the contributions from both initial states gives the single atom final state probability as a function of position:

$$
\begin{aligned}
P_f^{sa}(\boldsymbol{r},\delta) = {} & \sin^2(\frac{\sqrt{2}}{9}\frac{\beta_0\tau}{2}\sin\theta(\boldsymbol{r}))\,\mathrm{sinc}^2(\delta\tau/2) \\
& + \frac{1}{2}\sin^2(\frac{\sqrt{6}}{9}\frac{\beta_0\tau}{2}\sin\theta(\boldsymbol{r}))\left\{\mathrm{sinc}^2\left[\frac{(\delta - \frac{4\mu_B}{3\hbar}B(\boldsymbol{r}))\tau}{2}\right]\right. \\
& \left. + \,\mathrm{sinc}^2\left[\frac{(\delta + \frac{4\mu_B}{3\hbar}B(\boldsymbol{r}))\tau}{2}\right]\right\} \\
& + \frac{1}{2}\sin^2(\frac{2\sqrt{2}}{9}\frac{\beta_0\tau}{2}\cos\theta(\boldsymbol{r}))\left\{\mathrm{sinc}^2\left[\frac{(\delta - \frac{2\mu_B}{3\hbar}B(\boldsymbol{r}))\tau}{2}\right]\right. \\
& \left. + \,\mathrm{sinc}^2\left[\frac{(\delta + \frac{2\mu_B}{3\hbar}B(\boldsymbol{r}))\tau}{2}\right]\right\}
\end{aligned}
\tag{2.34}
$$

where

$$
\mathrm{sinc}\,x = \frac{\sin x}{x}. \tag{2.35}
$$

The expression for the final state probability (2.34) is given for one atom at a particular position in the magnetic field. To determine the contribution to the probability from the entire spatial distribution, we must multiply (2.34) by the atomic density $n(\boldsymbol{r})$ and integrate over the volume of the trapped atoms. Thus, the number of atoms that are detected in the final state is proportional to

$$P_f^{tot}(\delta) = \int d^3\boldsymbol{r}\, n(\boldsymbol{r}) P_f^{sa}(\boldsymbol{r}, \delta) \tag{2.36}$$

This expression for the spectrum is in the form of (2.1). By comparing (2.36) and (2.1), we see that the resolution function for this experiment is given by (2.34). Unlike the resolution function in previous Raman Induced Imaging Experiments [52–54], (2.34) is dependent on two features of the spatially varying magnetic field—direction and magnitude. This result will be used in Chapter 6 to obtain three-dimensional information about the spatial distribution of atoms in the MOT.

Chapter 3

Properties of Lithium

Before any trapping or imaging experiment could be designed, a suitable atom had to be chosen for study. In addition to meeting the needs of the current experiment, the chosen atom had to have the potential for accomplishing the long term goals of the laboratory, most notably the investigation of ultracold neutral fermions. Considering both present and future experiments, an atom was sought with the following properties:

- a transition easy to use for trapping and cooling with a wavelength within the range of the lab's dye laser and commercial diode laser technology
- a fermionic isotope readily and cheaply available,
- a relatively low melting point (<700°C) suitable for an atomic beam,
- a relatively simple energy level structure.

Because the alkali atoms possess a closed two level cooling transition, they are among the easiest atoms to cool and trap. In searching for a (radioactively) stable fermionic isotope of one of the alkali atoms, it was quickly determined that lithium, enriched to 95% ^{6}Li, was the cheapest available at $37 per gram. Since lithium has a melting point of 179 °C, a cooling transition at 671 nm within the range of our dye and commercial diode lasers, and a fairly simple level structure, ^{6}Li became the clear choice for the atom to use in this and future experiments.

3.1 Physical Properties

Lithium is a silver colored alkali metal with atomic number 3. It is the lightest of all metals and is very malleable at room temperature. Since lithium is an alkali metal, it is a strong reducing agent and reacts violently with water. In lithium's natural form, it is 92.5% ^{7}Li (nuclear spin $I = 3/2$) and 7.5% ^{6}Li ($I = 1$). The ^{6}Li is purchased in ingot form, submerged in oil to protect it from oxidation and moisture[1]. Before use, the surface coating of oil is removed with petroleum ether. Once the lithium is clean, flowing argon gas over it prevents significant contact with air until it is placed into the vacuum system.

Although lithium has been used as a drug in a chloride form for treatment of depression, in it's metal form it reacts strongly with skin moisture and is toxic if ingested. Consequently, latex gloves were worn whenever it was handled.

---

[1] The 95% enriched ^{6}Li was purchased from U. S. Services, Inc., 19 Ox Bow Lane, Summit, New Jersey 07001.

3.2 Thermodynamic Properties

Creating a *vapor cell* MOT for lithium was initially considered. The vapor cell MOT works by capturing atoms from a vapor without the need of a slowed atomic beam. Only atoms in the Maxwell-Boltzmann speed distribution with velocities below v_c, the maximum capture velocity of the MOT, are trapped. The thermodynamic properties of the lithium vapor prohibited this simplification of the experiment as I will now show.

At low densities, we can model the number of trapped atoms, N, in a vapor cell MOT using $\dot{N}(t) = R - \gamma N$, where R is the loading rate and γ is the loss coefficient. The solution to this equation is

$$N(t) = \frac{R}{\gamma}(1 - e^{-\gamma T}). \tag{3.1}$$

If the atoms in the vapor are in a Maxwell-Boltzmann speed distribution, the loading rate is given by [62]

$$R = \frac{n_0 V^{2/3} v_c^4}{2 v_{mp}^3} \tag{3.2}$$

where V is the trapping volume, n_0 is the number density, and v_{mp} is the most probable speed of an atom, given by

$$v_{mp} = \sqrt{\frac{2kT}{m}}. \tag{3.3}$$

Because the losses in a vapor cell MOT at low densities are primarily due to collisions with the untrapped atoms in the vapor [13], the loss coefficient is given by

$$\gamma \approx n_0 \sigma v_{mp} \tag{3.4}$$

where σ is the cross section for the atom-ejecting collision to occur.

Using (3.1), (3.2), and (3.4), we can solve for the steady state number of trapped atoms, N_{ss}:

$$N_{ss} = \frac{R}{\gamma} = \frac{V^{2/3}}{2\sigma}\left(\frac{v_c}{v_{mp}}\right)^4 \tag{3.5}$$

Surprisingly, N_{ss} is independent of n_0, the number density of the atoms in the vapor. This occurs because both the loading rate, R, and the loss coefficient, γ, are proportional to n_0.

Figure 3.1 shows the steady state number of trapped atoms for different alkalis as a function of temperature (above their respective melting points) using (3.5). For each alkali, $V = 4.2\,\text{cm}^3$ corresponding to 2 cm diameter laser beams, $v_c = 35\,\text{m/s}$, and $\sigma = 6.3\times10^{-13}\,\text{cm}^2$ [13]. While the cross sections, σ, are not exactly equal for the different atoms, they are approximately the same order of magnitude.

The differences between the results for different alkalis in this approximation are solely due to their different thermal velocities at the same temperature. For instance, at 200 °C, the thermal speed of ^{6}Li is 1145 m/s, while

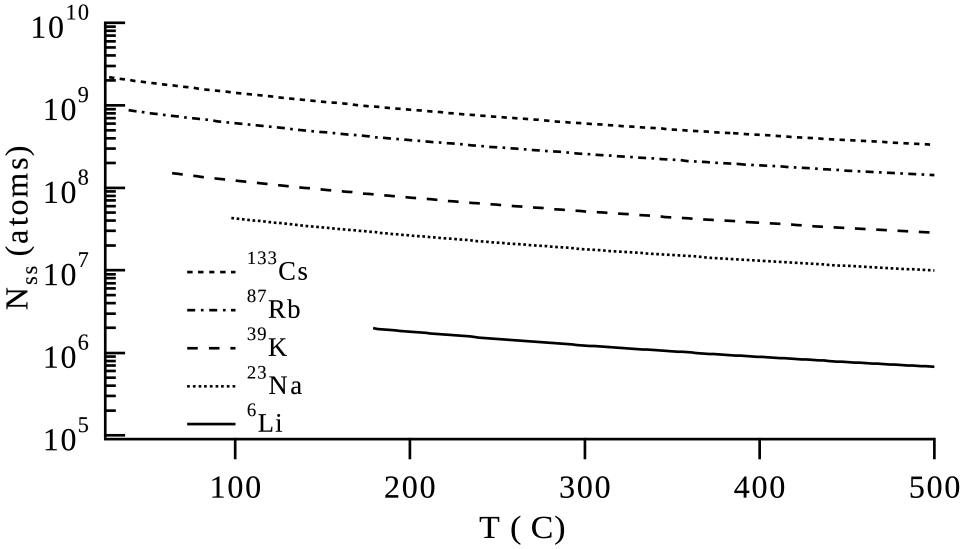

Figure 3.1: Steady state number of trapped atoms for alkalis in a vapor cell MOT.

the thermal speed of ^{133}Cs is 243 m/s. Since the difference in thermal speed is due to the dependence on mass, the number of steady atoms scales as the square of the atom's mass. Because ^{6}Li is so light and consequently has a high thermal velocity even at it's melting point, it does not make a good candidate for a vapor cell MOT. All other parameters equal, a vapor cell lithium MOT would capture all most three orders of magnitude fewer atoms than a cesium vapor cell MOT.

Achieving the maximum density possible in a standard MOT is desirable to maximize the imaging signal. The density maximizes near 10^{11} atoms/cc in a standard MOT due to density dependent loss mechanisms [44]. Although the capture volume can be a few cubic centimeters, once the atoms are trapped, they are cooled and compressed to volumes on the order of

$1\,\mathrm{mm}^3$. Thus, in order to achieve the maximum density, the MOT must capture approximately 10^8 atoms. A lithium vapor cell MOT would not be adequate.

A Zeeman slower allows one to decelerate an atomic beam and load the slow atoms into a MOT. This increases the loading rate R without a proportional increase in the loss rate γ, thus increasing the number of steady state trapped atoms. The details of the slower are explained in Section 4.4.

3.3 Electromagnetic Properties

The electromagnetic properties of ^{6}Li determine the wavelength of light required in the experiment, the intensities of the different laser beams, the magnetic field strengths for the slower and MOT, and the interpretation of the imaging data.

3.3.1 Energy Level Structure

Figure 3.2 shows the energy level structure of ^{6}Li [63]. The D_1 and D_2 lines are separated by 10.05 GHz. In this experiment, only the D_2 line transitions are used. The hyperfine splitting of the ground state is 228.2 MHz while the D_2 excited state levels are split by only 4.4 MHz. Since the excited state lifetime, τ, is 27.2 ns and the linewidth is thus $1/(2\pi\tau) = 5.8\,\mathrm{MHz}$, the excited state energy levels are approximately degenerate.

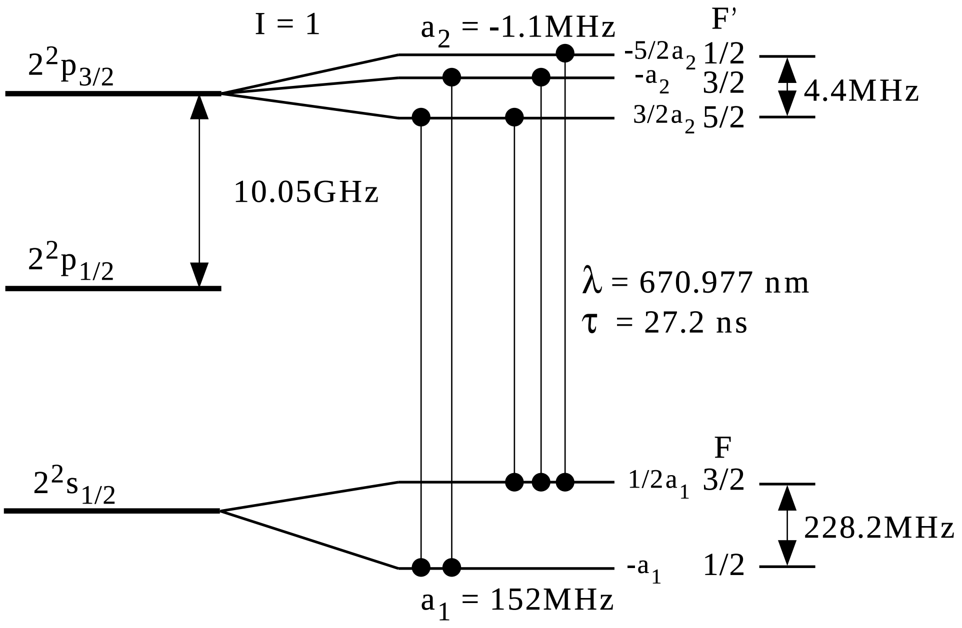

Figure 3.2: Energy level diagram of ^{6}Li.

The closed cooling cycles in the level structure of ^{6}Li are the

$$|F' = 5/2, m_{F'} = \pm 5/2\rangle \leftrightarrow |F = 3/2, m_F = \pm 3/2\rangle$$

transitions. Atoms in the endstates of the $F' = 5/2$ excited state can only decay to the respective endstate of the $F = 3/2$ ground state. Once in the $m_F = \pm 3/2$ state, excitation by $\sigma\pm$ circularly polarized light can only return the atoms to the $m_{F'} = \pm 5/2$ endstate. Atoms can cycle between these two levels indefinitely, limited only by the purity of the circularly polarized light and the local magnetic field direction.

3.3.2 Optical Transition Strength

The optical transition strength is characterized by the transition dipole moment, μ. For the closed endstate transitions, $\mu \equiv \mu_0$ can be calculated using its relationship to the excited state lifetime, $1/\tau = 4k^3\mu_0^2/3\hbar$, where $\hbar$ is Planck's constant and $k = 2\pi/\lambda$ is the wavenumber for the atomic transition. Solving for μ_0 and using $\lambda = 671\,\mathrm{nm}$, we get

$$\mu_0 = \sqrt{\frac{3\hbar}{4k^3\tau}} = 5.9\times10^{-18}\,\mathrm{esu{\cdot}cm} \text{ or } 5.9\,\mathrm{Debye}. \tag{3.6}$$

3.3.3 Optical Rabi Frequency

Using the transition dipole moment, μ we can calculate the optical Rabi frequency Ω which is the rate at which the atoms are coherently cycled between the excited and ground states when driven by resonant light. For ground state $|a\rangle$ and excited state $|b\rangle$ coupled by resonant light with field strength E, the Rabi frequency is given by[2]

$$\begin{aligned}\Omega &= \frac{\langle b|\mu E|a\rangle}{h}\\ &= \frac{\mu_{ba}E}{h}.\end{aligned} \tag{3.7}$$

Here E is the electric field strength corresponding to the intensity

$$I = \frac{c}{8\pi}|E|^2\,\mathrm{erg/cm^2{\cdot}s}. \tag{3.8}$$

---

[2] Unless otherwise indicated, all frequencies in this chapter will have units of Hz.

Using $c = 3\times10^{10}\,\mathrm{cm/s}$ and $1\,\mathrm{mW/mm^2} = 10^6\,\mathrm{erg/cm^2{\cdot}s}$, the Rabi frequency can be written in the more laboratory friendly form given by

$$\Omega\,(\mathrm{MHz}) = 4.37\,\mu\,[\mathrm{Debye}]\,\sqrt{I\,[\mathrm{mW/mm^2}]}. \tag{3.9}$$

With $|b\rangle = |F' = 5/2, m_{F'} = \pm5/2\rangle$ and $|a\rangle = |F = 3/2, m_F = \pm3/2\rangle$ for the closed cooling transition, the Rabi frequency is

$$\begin{aligned}\Omega_0\,(\mathrm{MHz}) &= \frac{\mu_0 E}{h} = 4.37\,\mu_0\,[\mathrm{Debye}]\,\sqrt{I\,[\mathrm{mW/mm^2}]}\\ &= 25.8\,\sqrt{I\,[\mathrm{mW/mm^2}]}.\end{aligned} \tag{3.10}$$

When the Rabi frequency Ω_0 is much larger than the spontaneous decay rate $\Gamma = 1/\tau = 36\times10^6\,\mathrm{s^{-1}}$ the transition is said to be saturated because the atoms will spend approximately half their time in each state despite the effect of spontaneous decay. In this regime, stimulated transitions repopulate the excited state much faster than spontaneous emission can deplete it.

In the closed cooling cycle the atoms cannot decay to the lower hyperfine ground state so they remain coupled to the circularly polarized light. When the transition is saturated, the fluorescence from the excited state decay is constant for several lifetimes, resulting in an easily detectable signal. The bright fluorescence is a characteristic of all alkalis (since they have a closed cooling cycle) and is called *photon bursting.* The power per ^{6}Li atom radiated during the photon burst is

$$P_0 = \frac{\hbar\omega}{2\tau} = \frac{hc}{2\lambda\tau} = 5.5\times10^{-9}\,\mathrm{mW}. \tag{3.11}$$

The factor of 2 in the denominator occurs because the atom only spends half of its time in the excited state. By measuring the fluorescence emitted by the atoms during photon bursting and by dividing this by P_0 we can approximately determine the number atoms interacting with a resonant laser beam.

3.3.4 Dipole Moment Matrix Elements

To determine Raman Rabi frequencies in the next section, the transition dipole moments for all the transitions must be known. The dipole moment for the cycling transition is calculated using (3.6). Because the other excited states are optically coupled to multiple ground states, (3.6) cannot be used to determine their transition dipole moments. To calculate the arbitrary matrix element

$$\langle (J' = 3/2, I = 1)F', m_{F'}|\mu^1_q|(J = 1/2, I = 1)F, m_F\rangle$$

the Wigner-Eckart Theorem and momentum recoupling theory are used. The details of the calculations are presented in Appendix A.

The results of the calculations are presented in Figures 3.3 and 3.4. All of

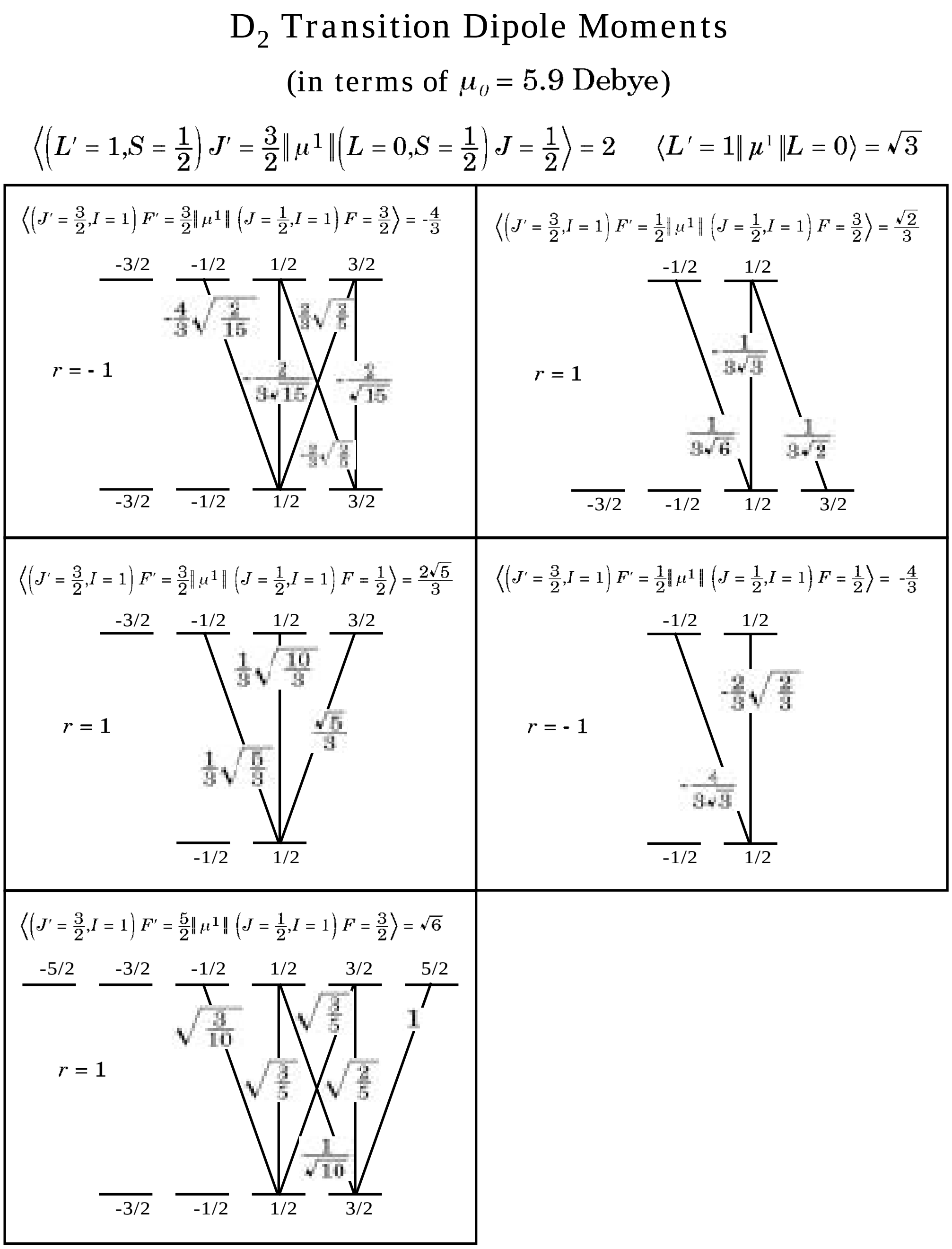

Figure 3.3: Transition dipole moments of the D_2 line in ^{6}Li.

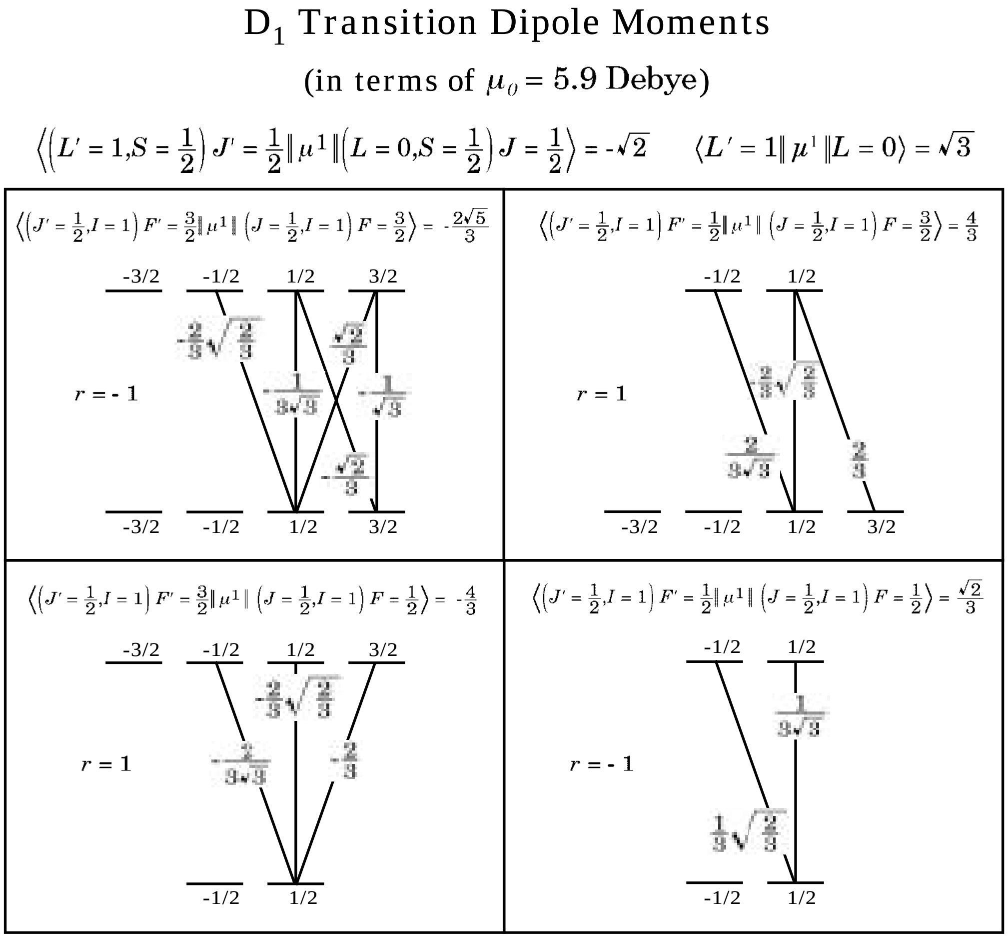

Figure 3.4: Transition dipole moments of the D_1 line in ^{6}Li.

the matrix elements, including the reduced elements, are expressed in units of $\mu_0 = 5.9\,\text{Debye}$. Due to symmetry, only half the matrix elements are shown. The other half are related by r, which is either 1 or -1, depending on the particular F-levels involved. For instance, from Figure 3.4 we see that

$$\begin{aligned}
&\langle (J' = \frac{1}{2})F' = \frac{1}{2}, m_{F'} = \frac{1}{2}|\mu^1_1|(J = \frac{1}{2})F = \frac{1}{2}, m_F = -\frac{1}{2}\rangle \\
&\quad = (-1)\langle (J' = \frac{1}{2})F' = \frac{1}{2}, m_{F'} = -\frac{1}{2}|\mu^1_{-1}|(J = \frac{1}{2})F = \frac{1}{2}, m_F = \frac{1}{2}\rangle \\
&\quad = -\frac{1}{3}\sqrt{\frac{2}{3}}\mu_0 = -\frac{1}{3}\sqrt{\frac{2}{3}}\,5.9\,\text{Debye} = -1.61\,\text{Debye}
\end{aligned}$$

These matrix elements make it possible to calculate the Raman Rabi frequencies.

3.3.5 Raman Rabi Frequencies

A three level atom theory for Raman transitions is presented in Section 2.1. To calculate the Raman Rabi frequencies for a multi-level atom, one must sum the Raman transition strength over the possible paths through all of the intermediate states. The Raman Rabi frequency (2.15) becomes

$$\beta = -\sum_I \frac{\langle f|\boldsymbol{\mu}\cdot\boldsymbol{E_2}|I\rangle\langle I|\boldsymbol{\mu}\cdot\boldsymbol{E_1}|i\rangle}{2h^2\Delta_I}. \tag{3.12}$$

where $|f\rangle$ is the final state, $|i\rangle$ is the initial state, $|I\rangle$ are the intermediate states, and Δ_I is the detuning from $|I\rangle$.

In the experiment, Raman transitions are made within the ground state

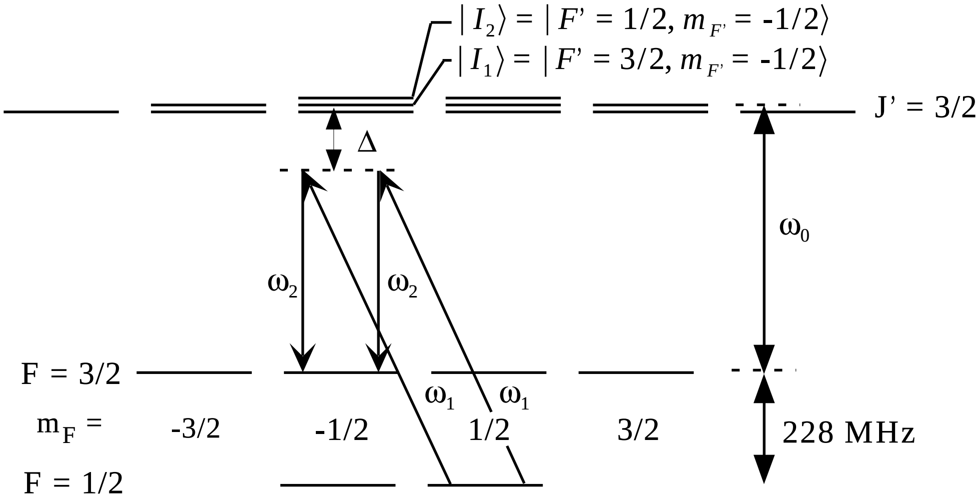

Figure 3.5: Energy level diagram of a ^{6}Li Raman transition.

hyperfine structure of ^{6}Li, from $|F = 1/2\rangle$ to $|F = 3/2\rangle$. The nearly degenerate $J' = 3/2$ levels act as intermediate states so all the Δ_I are equal. The contribution from the intermediate states in the $J' = 1/2$ level is negligible because the Raman fields are detuned 10 GHz from the D_1 line while only approximately 118 MHz from the D_2 line.

Figure 3.5 shows an energy level diagram of a Raman transition between $|F = 1/2, m_F = 1/2\rangle$ and $|F = 3/2, m_F = -1/2\rangle$. The optical frequencies in the Raman beam are ω_1 and ω_2 and $\hbar\omega_0$ is the energy difference between the final and intermediate state. Thus,

$$\begin{aligned}\Delta &= \omega_1 - (\omega_0 + 228\,\mathrm{MHz}) = \omega_2 - \omega_0 \\ &\approx -118\,\mathrm{MHz}\text{ in our experiments.}\end{aligned}$$

In this example, the electric field polarizations are given by $\boldsymbol{E_1} = E_1\hat{\boldsymbol{x}}$ and $\boldsymbol{E_2} = E_2\hat{\boldsymbol{z}}$. We assume that a magnetic field along $\hat{\boldsymbol{z}}$ prevents Raman transitions to $|F = 3/2, m_F = 3/2\rangle$, a condition explained later in this section. For this transition, the Raman Rabi frequency is

$$\begin{aligned}
\beta_{\frac{1}{2},\frac{-1}{2}} &= -\sum_I \frac{\langle F=\frac{3}{2}, m_F=-\frac{1}{2}|\boldsymbol{\mu}\cdot\boldsymbol{E_2}|I\rangle\langle I|\boldsymbol{\mu}\cdot\boldsymbol{E_1}|F=\frac{1}{2}, m_F=\frac{1}{2}\rangle}{2h^2\Delta_I} \\
&= -\frac{E_2E_1}{2h^2\Delta}\frac{1}{\sqrt{2}}\sum_I \langle F=\frac{3}{2}, m_F=-\frac{1}{2}|\mu_0^1|I\rangle\langle I|\mu_1^1|F=\frac{1}{2}, m_F=\frac{1}{2}\rangle \\
&= -\frac{E_2E_1}{2h^2\Delta}\frac{1}{\sqrt{2}}\left[\langle F=\frac{3}{2}, m_F=-\frac{1}{2}|\mu_0^1|F'=\frac{3}{2}, m_{F'}=-\frac{1}{2}\rangle\right. \\
&\quad\times\langle F'=\frac{3}{2}, m_{F'}=-\frac{1}{2}|\mu_1^1|F=\frac{1}{2}, m_F=\frac{1}{2}\rangle \\
&\quad+\langle F=\frac{3}{2}, m_F=-\frac{1}{2}|\mu_0^1|F'=\frac{1}{2}, m_{F'}=-\frac{1}{2}\rangle \\
&\quad\left.\times\langle F'=\frac{1}{2}, m_{F'}=-\frac{1}{2}|\mu_1^1|F=\frac{1}{2}, m_F=\frac{1}{2}\rangle\right],
\end{aligned}$$

and using the matrix elements in Figure 3.3

$$\begin{aligned}
&= -\frac{\mu_0^2E_2E_1}{2h^2\Delta}\frac{1}{\sqrt{2}}\left[\left(\frac{2}{3\sqrt{15}}\right)\left(\frac{1}{3}\sqrt{\frac{5}{3}}\right)+\left(-\frac{1}{3\sqrt{3}}\right)\left(-\frac{4}{3\sqrt{3}}\right)\right] \\
&= -\frac{\mu_0^2E_2E_1}{2h^2\Delta}\frac{\sqrt{2}}{9}. \qquad (3.13)
\end{aligned}$$

Arbitrary choices for the intensities of the E_2 and E_1 fields affect the Raman transition efficiency because of the light shifts they cause on the levels involved in the transition. As described in Chapter 2, unequal light shifts on the initial and final states will change the resonance frequency of the Raman transition. To maximize the transition efficiency over the entire sample, we want to equalize the light shifts on both the initial and final states. The light shift of a ground state in a multi-level atom is given by modifying (2.14) to account for all the levels coupled to the state:

$$\nu = \sum_i \frac{\Omega_i^2}{4\Delta_i} \tag{3.14}$$

for $|\Delta| \gg \Omega_i$, where i is summed over every excited state coupled to the ground state by the incident light, Ω_i is the Rabi frequency (3.7) for each transition, and Δ_i is the detuning from each excited state.

In the experiment, the detunings with respect to the D_2 resonance are much smaller than the fine structure splitting, 10 GHz for ^{6}Li, so the light shifts due to coupling with the D_1 resonance are negligible. Since the D_2 excited states are degenerate, the light shift of a ^{6}Li ground state due to linearly polarized light can be written as

$$\nu_{lin} = \frac{\Omega_0^2}{6\Delta} \tag{3.15}$$

where Ω_0 is defined in (3.10) and $\Delta = \omega - \omega_{res}$, the detuning of the laser frequency ω from the resonance frequency ω_{res}. Because (3.15) arises from a scalar operator and is independent of m_F as described in Chapter 2, all the hyperfine levels shift uniformly. Also note that from (3.10), ν_{lin} is proportional to the intensity.

The detuning of the Raman beams from the excited state in our experiment is centered at $\Delta = -118\,\mathrm{MHz}$. From Figure 3.5, the two Raman frequencies are $\omega_1 = \omega_0 + 110\,\mathrm{MHz}$ and $\omega_2 = \omega_0 - 118\,\mathrm{MHz}$. If I_1 and I_2 are the intensities of the two Raman beams, then the condition for equal light shifts on $|i\rangle$ and $|f\rangle$ becomes

$$\begin{aligned} \nu_i &= \nu_f \\ \frac{I_1}{-118} + \frac{I_2}{-346} &= \frac{I_1}{110} + \frac{I_2}{-118} \end{aligned} \tag{3.16}$$

where the denominators are determined by the detuning of the fields from the resonance frequency of each transition. Using this expression to solve for the ratio of intensities, we find that

$$\frac{I_2}{I_1} = \frac{173}{55} \approx 3.1 \tag{3.17}$$

will achieve equal light shifts on the $F = 1/2$ and the $F = 3/2$ ground states. The higher frequency Raman field must be less intense than the lower frequency Raman field.

If we set the ratio of intensities according to (3.17) we can rewrite the Raman Rabi frequency we calculated in (3.13) as $\sqrt{2}\beta_0/9$ where, using (3.10) and $\Delta = -118\,\mathrm{MHz}$,

$$\begin{aligned} \beta_0 &= -\frac{\mu_0^2 E_1^2}{2h^2\Delta}\sqrt{\frac{173}{55}} = -\frac{\Omega_0^2}{2\Delta}\sqrt{\frac{173}{55}} \\ &= 5\,(\mathrm{MHz})\ I_1\,[\mathrm{mW/mm^2}]. \end{aligned} \tag{3.18}$$

		$\vert f\rangle$: $F=3/2$			
	m_F	-3/2	-1/2	1/2	3/2
$\vert i\rangle$: $F=1/2$	1/2	—	$\frac{\sqrt{2}}{9}$	$\frac{2\sqrt{2}}{9}$	$\frac{\sqrt{6}}{9}$
	-1/2	$\frac{\sqrt{6}}{9}$	$\frac{2\sqrt{2}}{9}$	$\frac{\sqrt{2}}{9}$	—

Table 3.1: Raman Rabi frequency magnitudes.

Table 3.1 contains the magnitude of the Raman Rabi frequencies for transitions from $|F = 1/2\rangle$ to $|F = 3/2\rangle$ in the ground state of ^{6}Li using perpendicular linearly polarized Raman beams. The magnitudes are given in units of β_0 which can be calculated for different detunings and intensity ratios.

Within the ground state hyperfine structure of ^{6}Li, only Raman transitions where $\Delta m = 0, \pm 1$ are allowed, as explained in Chapter 2. The matrix element for a $\Delta m = \pm 2$ transition would be identically 0 because the multiple paths that the atom can take in the transition destructively interfere. A $\Delta m = \pm 2$ would require a rank-2 operation on the initial state. However, because the initial and final states are within the $J = 1/2$ basis, and vector addition of 1/2 and 2 cannot give 1/2, the $\Delta m = \pm 2$ transition is not allowed. This result is addressed in more detail in Chapter 2.

3.3.6 The Effect of Magnetic Fields on the Raman Transitions

In the absence of a magnetic field, the Raman transitions are degenerate, all occurring at difference frequencies of 228 MHz. In the atom's coordinate system, perpendicular linearly polarized Raman beams can be viewed as $\{\hat{\boldsymbol{x}}, \hat{\boldsymbol{y}}\}$, $\{\hat{\boldsymbol{x}}, \hat{\boldsymbol{z}}\}$, etc. polarized. These are equivalent pictures as long as no magnetic field is present.

The imaging experiment is performed within the MOT's quadrupole magnetic field so the magnitude and direction of the magnetic field vary in space. Although the two Raman beams do not specify a quantization axis, the direction of the magnetic field does, as shown in Figure 3.6. In the lab frame, the Raman beams are $\{\hat{\boldsymbol{x}}, \hat{\boldsymbol{y}}\}$ polarized and propagate along the lab $\hat{\boldsymbol{z}}$ axis. In the atom's coordinate system, the $\hat{\boldsymbol{z}}'$ is determined by the local magnetic field direction and the polarizations of the Raman beams are rotated accordingly, as shown in Figure 3.6. Because of the change in quantization axis, the direction of the magnetic field determines which Raman transitions are allowed.

The Zeeman shift of the the initial state $|F = 1/2, m_F\rangle$ and final state $|F = 3/2, m_F\rangle$ energy levels will determine the splitting of the Raman transitions. Each level shifts by

$$\Delta E = g_F m_F \mu_B B, \tag{3.19}$$

where

$$g_F = \frac{F(F+1) - I(I+1) + S(S+1)}{F(F+1)}, \tag{3.20}$$

μ_B is the Bohr magneton, and B is the magnitude of the magnetic field.

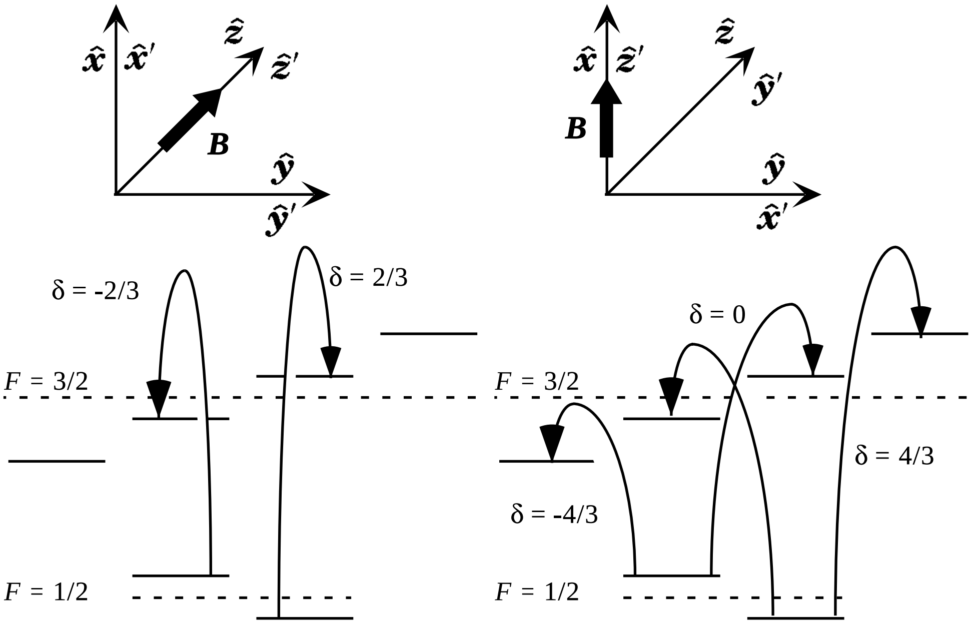

Figure 3.6: ^{6}Li Raman transitions in a magnetic field.

		$\lvert f\rangle$: $F=3/2$			
	m_F	-3/2	-1/2	1/2	3/2
$\lvert i\rangle$: $F=1/2$	1/2	—	0	$\frac{2}{3}$	$\frac{4}{3}$
	-1/2	$-\frac{4}{3}$	$-\frac{2}{3}$	0	—

Table 3.2: Raman resonance frequency shifts in a magnetic field.

The values of the g-factors are $g_{3/2} = 2/3$ and $g_{1/2} = -2/3$. If m_1 is the $\hat{z}'$-component of the angular momentum for the initial state and m_2 is the $\hat{z}'$-component for the final state, the frequency shift of the Raman transition due to the presence of the magnetic field is

$$\delta^B_{m2,m1} = \frac{2}{3}\frac{\mu_B B}{h}(m_2 + m_1) \tag{3.21}$$

$$m_2 = \{-3/2, -1/2, 1/2, 3/2\} \qquad m_1 = \{-1/2, 1/2\}. \tag{3.22}$$

This creates six separate transitions. However, because there are two degenerate transitions where $\delta = 0$, there are only five separate resonances. Table 3.2 shows the frequency shift for each transition in units of $\mu_B B/h = 1.4\,B\,[\mathrm{G}]\,(\mathrm{MHz})$.

Chapter 4

Cooling and Trapping Apparatus

In order to trap lithium atoms, a significant amount of apparatus was built. An atomic beam system, ultra-high vacuum system, Zeeman slower [2, 3], and magneto-optic trap (MOT) [4, 9] were built to create a sample of cold trapped atoms. This chapter describes the separate pieces of the apparatus used to slow and capture the lithium atoms.

As shown in Figure 4.1, an oven at the end of the vacuum system creates an atomic beam. The atoms initially have an average velocity over 1600 m/s. When the atoms enter the Zeeman slower, radiation pressure is used to de-

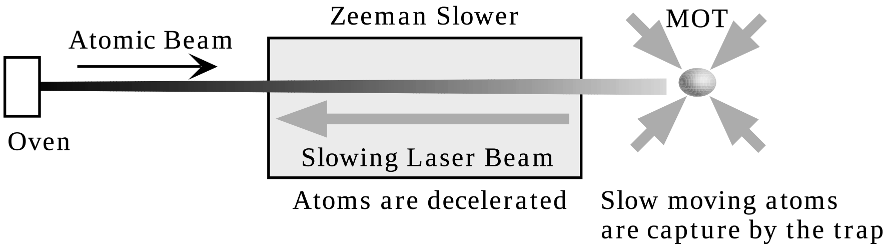

Figure 4.1: A schematic of the apparatus used to cool and trap the atoms.

celerate them. As the atom decelerates, the doppler shift of the slowing laser beam continually changes. In order to keep the atoms in resonance with the slowing beam, their resonance frequency is tuned by the Zeeman shift. The Zeeman slower creates the spatially varying magnetic field and hence, spatially varying atomic resonance frequency, that keeps the atoms in resonance with the slowing beam while they decelerate. Atoms which are initially travelling over 1100 m/s are decelerated to velocities around 40 m/s. Once the atoms leave the slower, additional laser beams and magnets are used to confine the atoms in a MOT. In the trap, the average velocity is reduced to approximately 1 m/s corresponding to a temperature of 350 μK.

The first sections of this chapter discuss the most fundamental parts of the trapping system—the atomic beam, vacuum system, and laser sources. Then, the atom's deceleration in the Zeeman slower is explained. The last section describes the MOT. In Chapter 5, I show how all of the apparatus is used in the imaging experiment.

4.1 The Oven

First, I will explain how the beam of ^{6}Li atoms is created. The beam originates in the oven at one end of the vacuum system. The oven melts the lithium, which is solid at room temperature, to create a significant vapor pressure. The vapor exits the oven through a long collimating nozzle and enters the multi-coil Zeeman slower.

To create the lithium vapor, the lithium was heated above it's melting point of 179 °C. Above this temperature, the vapor pressure, P, of liquid lithium is given by [64]

$$\log_{10} P\,[\text{torr}] = 10.3454 - \frac{8345.57}{T} - 8.84\times10^{-5}T - 0.68106\log_{10} T \quad (4.1)$$

where T is the temperature in degrees Kelvin. During most of the data acquisition, the temperature of the oven was approximately 400 °C causing a vapor pressure of

$$P = 9.2\times10^{-5}\,\text{torr}. \quad (4.2)$$

Using the ideal gas law, the number density of the atoms in the vapor is

$$n = \frac{P}{k_B T} = 9.66\times10^{18}\frac{P[torr]}{T[K]}\,\text{atoms/cc} \quad (4.3)$$

where k_B is Boltzmann's constant. At $T = 400\,^\circ\text{C}$, this evaluates to

$$n_0 = 1.3\times10^{12}\,\text{atoms/cc}. \quad (4.4)$$

As shown in Figure 4.2, the oven consists of a hot reservoir 2.5 in. tall and 3/4 in. in diameter. The 1/32 in. wall thickness 316SS reservoir is sealed at the bottom and welded at the top to a 1.33 in. conflat mini-flange. A 6.25 in. long 1/4 in. od. tube is connected to the reservoir 1.25 in. from the

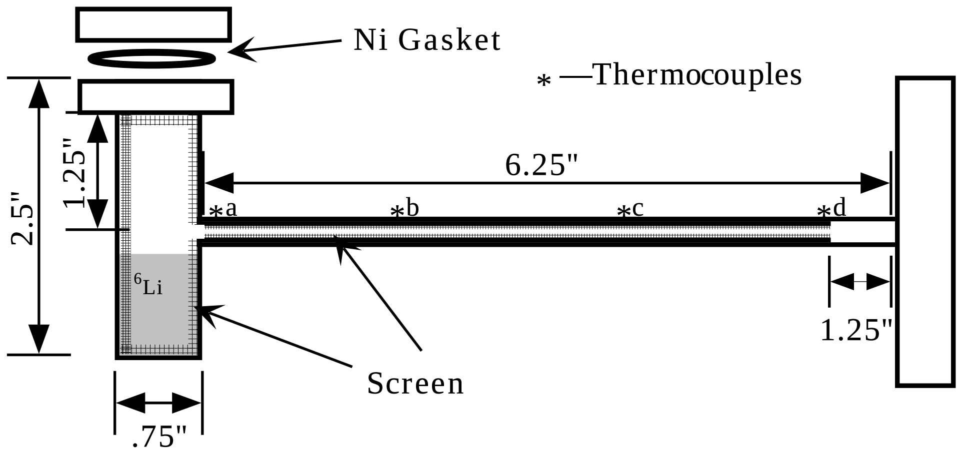

Figure 4.2: The oven.

reservoir top. At the oven end, the nozzle tube has an aperture of 1/8 in. and at the exit end the aperture was drilled out to 3/16 in. The collimation angle provided by the nozzle is $\theta = 0.125/6 = 21$ mr. Thinning of the nozzle wall at the exit end allows a greater temperature gradient near the end of the nozzle, helps prevent clogging from lithium condensation, and reduces the heat flow out of the nozzle.

A nickel gasket is used between the flanges that seal the reservoir. The nickel gasket provides a better seal than copper when the flange is temperature cycled repeatedly. Occasionally, oven temperatures were increased to 500 °C which is above the recommended specifications for the flange, and both copper and silver-coated copper gaskets failed during these runs. In addition, and more importantly, the nickel gasket is less reactive with the lithium vapor in the oven.

The reservoir and nozzle are heated by nichrome wire. The wire is electrically insulated from the stainless steel oven by a thin coating of Omegabond 400 High Temperature Air Set Cement, a thermally conducting cement. On the reservoir, the greatest concentration of wire wrapping occurs between the conflat mini-flange and the nozzle. This should keep the mini-flange relatively free of condensed ^{6}Li which will allow us to refill the oven if necessary. The concentration of wraps on the nozzle is highest at the oven end and gradually reduces toward the output end to produce a temperature gradient along the nozzle. After the wire was wrapped around the oven, additional coats of cement were applied to hold it in place. The oven is enclosed in fire brick to provide insulation from the local air temperature.

The oven was designed to recirculate the lithium that doesn't pass through the collimating nozzle tube [65]. The fine 316SS screen that lined the nozzle and the temperature gradient in the nozzle causes the condensed uncollimated lithium to wick back to the reservoir. However, no attempts have been made to verify if this recirculation is working. Because the vacuum system operates in the 10^{-11} torr range and can take over a week to restart, the recirculating oven design was implemented to maximize the lifetime of our oven.

Ideally the temperatures along the nozzle tube would be the highest at the oven and gradually decrease until the temperature was slightly above the melting point of lithium at the exit. Four thermocouples mounted on the oven and along the nozzle tube, as shown in Figure 4.2, provide temperature measurements during the experiment. Table 4.1 shows typical oven and

Thermocouple	a	b	c	d
Temperature °C	360	405	429	256

Table 4.1: Nozzle temperature gradient.

nozzle temperatures when taking the imaging data.

The winding of the reservoir and oven is somewhat of an art. After the second coat of cement is applied, no further adjustments in the wrapping can be made. The nozzle and the reservoir were wound with separate wires and the current through each heater is controlled separately which does provide some differential control of the temperatures. However, in this particular oven the temperature gradient is not ideal.

The two nichrome heating wires were powered by a Sorensen 40 V-25 A power supply. During warmup, approximately 10 A combined flows through the wires. The current is divided using two high power MOSFETs with gate voltages independently controlled. After the oven is warm, approximately 8 A combined flows through the wires at approximately 20 V.

With a nominal oven temperature around 400 °C, the mean free path of the ^{6}Li atom is much longer than any of the nozzle dimensions. The mean free path, λ_A, can be calculated using [66]

$$\lambda_A = \frac{1}{\sqrt{2}\sigma_k n_0} \tag{4.5}$$

where σ_k is the collisional cross section for lithium and n_0 is given by (4.4). Using $\sigma_k = 7.6\times10^{-16}\,\mathrm{cm}^2$ [66] and (4.4), we get a mean free path of $\lambda_A =$

7.1 m. With the mean free path much longer than the dimensions of the oven and nozzle, the source operates in the effusive limit where collisions with other atoms in the nozzle can be neglected.

An estimate of the oven lifetime may be calculated by considering the flux of atoms leaving the oven reservoir. Since this lifetime estimate neglects any recirculation provided by the nozzle, the actual oven lifetime should be much longer. The flux from the oven reservoir into the nozzle is given by [67]

$$\Phi = \frac{1}{4} n_0 \bar{v} \tag{4.6}$$

where $\bar{v} = \sqrt{8k_B T/(\pi m)} = 1538\,\mathrm{m/s}$ is the average speed of the atoms in the reservoir. The number of atoms leaving the reservoir per second, $\dot{N}$ is given by

$$\dot{N} = \Phi A_s = \frac{n_0 \bar{v} A_s}{4} = 4\times 10^{15}\,\mathrm{atoms/s} \tag{4.7}$$

where $A_s = 8\,\mathrm{mm}^2$ is the area of the oven-nozzle aperture shown in Figure 4.2. After loading the oven, a procedure described in Section 4.2.2, the oven contains 2–3 g of ^{6}Li, so the oven lifetime at 400 °C is on the order of 2 years! Because the running temperature is lower than what was initially planned, the recirculation provided by the nozzle is probably not necessary. However, at 500 °C which was the temperature occasionally used in preliminary experiments, the oven lifetime lowers to just 3 weeks.

4.2 The Vacuum System

Now that I have described the relevant properties of the ^{6}Li atom and how the ^{6}Li beam was created, I will discuss the components of the vacuum system. While this preliminary experiment did not require the ultra-high vacuum (UHV) system that was built, future experiments will require the long trapping times enabled by it.

4.2.1 Vacuum System Components

A schematic of the vacuum system is shown in Figure 4.3. The atoms exit the oven nozzle and enter a 4 in. d. by 12 in. tall cylindrical pumping chamber which has five additional ports. The bottom port connects through a gate valve (A) to a 400 l/s turbopump which roughs out the vacuum system to about 10^{-8} torr. A bellows valve (B) connects the turbopump to a 10.7 cu. ft./min. mechanical pump which maintains the foreline pressure on the turbopump and provides some additional roughing capacity.

A window is attached to the top port which provides a view of the atomic beam fluorescence. The presence or absence of fluorescence allows us to check the laser frequency and operation of the atomic beam. In addition, the window provides a view of the slower beam scatter from the oven nozzle.

There are two side ports on the pumping chamber. One side port is coupled to a UHV nude Bayard-Alpert ionization gauge and a 20 l/s triode ion pump. The other side port was connected to a bakeable stainless steel seal

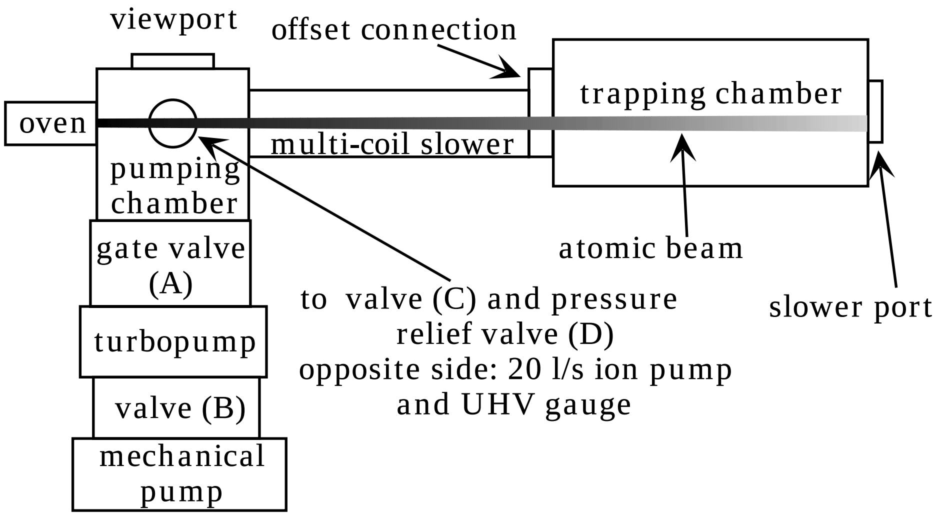

Figure 4.3: Schematic diagram of the vacuum system.

bellows valve (C)[1] followed by a 2 PSI relief pressure valve (D), the opposite end of which was an open connection for raising the vacuum system up to atmospheric pressure.

Opposite the oven was the slower port. While all other flanges in this section of the vacuum system are coupled with regular copper gaskets, the slower port is coupled with a 1/4 in. id. by 6 in. long copper tube mounted within a solid copper gasket. These gaskets are normally sold for pinching off evacuated ion pumps for storage. In the current apparatus, the gasket and tube lower the conductance between the oven and trapping region. This allows the two regions to be differentially pumped as discussed in Section 4.2.2.

---

[1] Usually these valves are used in flowing applications and are marked with an arrow indicating the preferred direction of the flow. The point of the arrow indicates the side of the bellows with the exposed lubricant. For HV and UHV vacuum system applications, only the *other* side of the valve should be exposed to the vacuum to prevent outgasing.

In the vacuum system, the slower is simply a long tube which provides additional restriction for differential pumping. Connecting the slower and the trapping region is a 3/4 in. od. nipple which is offset from center on the trapping side flange by 3/8 in. The offset causes the unslowed portion of the atomic beam to pass under the trap and reduces collisional losses from the trap.

Figure 4.4 shows the trapping region of the experiment. It was designed to accommodate both a large number viewports for optical access as well as the space requirements for the MOT magnets as described in Section 4.5.2. Consequently, in addition to the atomic beam entrance port and a pumping port, the trapping region has 13 viewports. The pumping port leads to a 240 l/s ion pump and another UHV ionization gauge. The anti-reflection coated viewport windows are made of 7056 Glass and mounted within a 2.75 in. flange. Since the windows are used in the UHV region, it is important that they can withstand the thermal stresses involved in a 350 °C bakeout.

The port located at the end of the system provides optical access for the slowing laser beam. Because the atomic beam hits the slowing window, a film of lithium now coats it. To prevent this from occurring in the future, that window must be continually heated to 200 °C, slightly above lithium's melting point.

During assembly, we wore latex gloves to minimize the contamination of skin oils in the system. Most of the vacuum system parts were cleaned at the manufacturer. Any parts that were machined in house were cleaned and

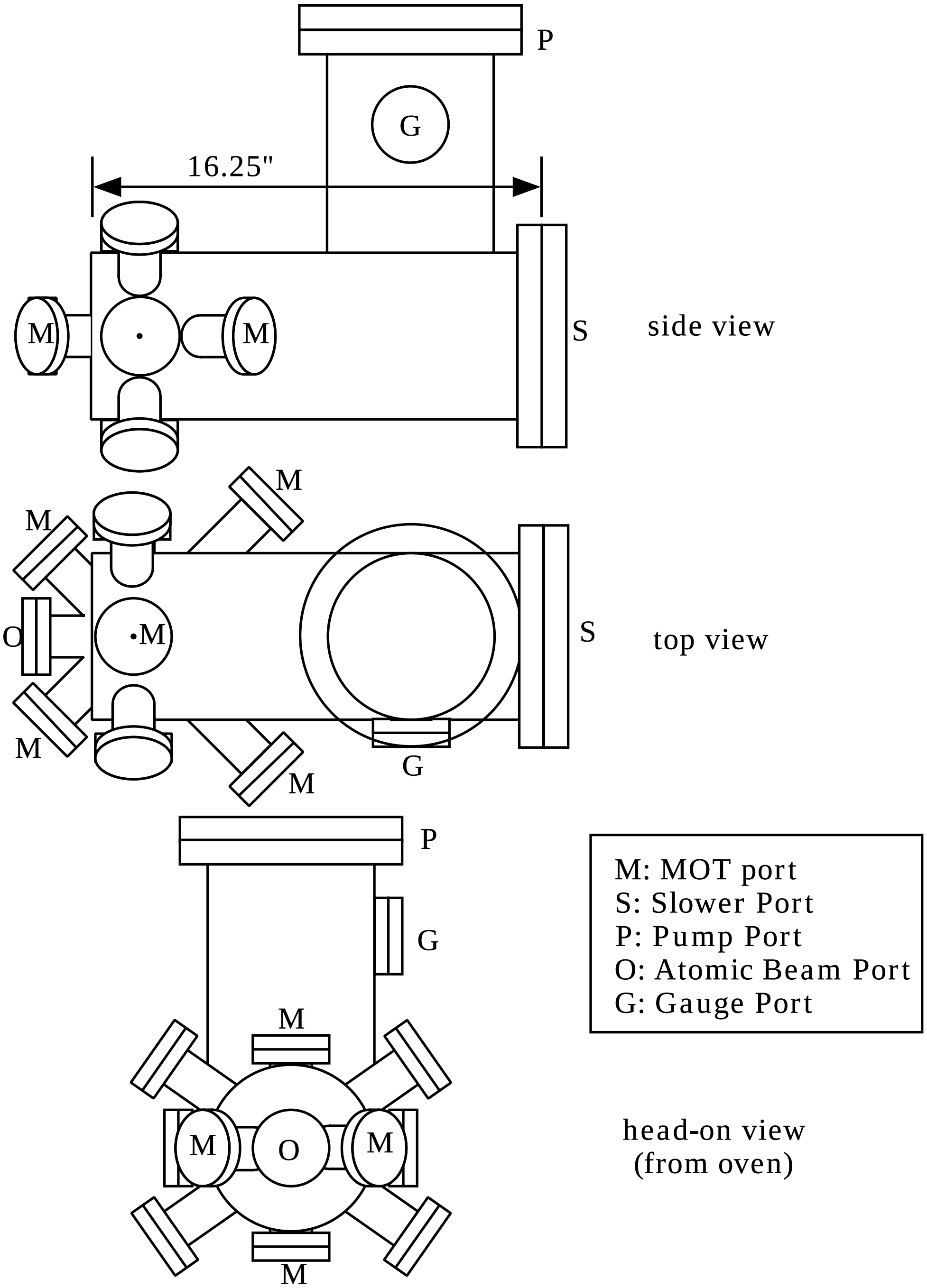

Figure 4.4: The trapping region.

welded at the Duke University Free Electron Laser Laboratory. When parts must be cleaned in the lab, an ultrasonic cleaner is used with the following series of solvents:

1. Alconox and distilled water
2. distilled water
3. acetone (two times)
4. methanol (two times).

All flanges and gaskets are cleaned with acetone and methanol (in that order) prior to assembly.

Silver plated bolts and flange nuts made the assembly much easier. Silver plated bolts do not grab the flanges or the threads in the nut, and are consequently much easier to tighten. Although anti-seize lubricant may be used for the same purpose, it is a potential contaminant to the vacuum system and doesn't work nearly as well. Flange nuts contain a built in lock-washer and do not need to be held by an additional wrench while tightening.

4.2.2 Vacuum System Procedures

Once the vacuum system was assembled, procedures were developed for using it. In this section, I will describe how the system is operated on a daily basis as well as the startup and shutdown procedures.

Daily Operation

When the system is under vacuum, but the experiment is *not* running, the turbopump is kept off. When on, the turbopump whines unpleasantly like a jet engine. With a cold oven, the ion pumps maintain the pressure near 6×10^{-10} torr in the oven region and 6×10^{-11} torr in the trapping region. Valve C is kept closed, keeping the system under vacuum.

Valves (A) and (B) must also be closed with the turbopump off to prevent the foreline pressure around 1 mtorr inside the turbopump from reaching the rest of the system. The mechanical pump is also turned off, and must be disconnected from valve (B) and let up to atmosphere to prevent oil from siphoning toward the turbopump.

At least four hours before running the experiment, the mechanical and turbopumps are restarted. First, the mechanical pump is reattached to valve (B). Then, both pumps are started simultaneously. After about a 30 s warmup period but before the turbopump has reached it's maximum speed, valve (B) is opened. Since valve (A) is still closed, it only takes a few hours for the turbopump to reach its minimum pressure of 5×10^{-9} torr.

About an hour before the experiment begins, the oven is warmed up. The pressure in the pumping chamber gradually rises as the oven heats. When the pressure reaches 10^{-8} torr, gate valve (A) is slowly opened. Once the gate valve is open, the pressure in the pumping region drops to 5×10^{-9} torr, the minimum pressure of the turbopump. Gradually, as the oven continues to warm, the pressure rises to 10^{-8} torr again, where it remains during the experiment. At this point, the temperature in the oven will have reached the steady state values shown in Table 4.1. Due to differential pumping [68], the pressure in the trapping region remains two orders of magnitude lower at 10^{-10} torr.

When the experiment is concluded and the oven is shut off, the pressure in the pumping chamber rapidly drops to the minimum pressure of the turbopump and the gate valve (A) is closed. If the experiment is to be run the next day, the turbopump is left running. If not, valve (B) is closed, the turbo and mechanical pumps are turned off, and the mechanical pump is disconnected from valve (B).

Startup Procedures and Bakeout

In this section, I will describe how the vacuum system is turned on from atmospheric pressure, how ovens are loaded, and the procedures used to bake out the system. Once running, the vacuum system rarely must be restarted from atmospheric pressure.

Turning on the vacuum system requires valve (C) to be closed and valves (A) and (B) open. First, the mechanical pump is started, followed immediately afterward by the turbopump. Once the turbopump has reached its maximum speed, after about 3 min., the pressure in the system is below 1 mtorr and the ion pumps can be started. However, the ion pumps become quickly saturated when turned on this way, and loose half of their pumping speed [69]. A bakeout, discussed below, will restore the ion pumps to their full pumping capacity. After about one hour of operation, the pressure in the vacuum system drops to 10^{-6} torr.

To prepare the lithium for loading, it is cut into into pieces small enough to fit through the aperture at the top of the oven. Lithium is very malleable, but is easily cut by a sharp wire snipper. Once cut, it is dipped in petroleum ether to remove the oils used in storing it. While preparing the lithium, argon gas is flowed over it to minimize contact with the nitrogen and water in the air which react with it.

The vacuum system must be prepared for loading the oven as well. Argon gas is connected to the open end of valve (D) with valve (C) open, and the top of the oven is removed so that the argon gas exits the vacuum system through the top of the oven. The clean chunks of lithium are quickly dropped into the oven reservoir. The pressure of the argon gas should be fairly low to prevent the light lithium from being blown out of the system. Once the reservoir is full, usually with $1 - 2$ g of ^{6}Li the oven is closed, valve (C) is shut, and the argon is disconnected.

Although the lithium is cleaned with petroleum ether, it still acts like a contaminant in the vacuum system. With fresh (but dirty) lithium in the system, the vacuum system must be baked out.

First, the turbopump and mechanical pump are started as described earlier. The ion pumps remain off, initially. The pumping chamber, trapping chamber, and all stainless steel vacuum tubes are heated to 250 °C[2] and the

---

[2] In the initial bakeouts, the metal components in the vacuum system were heated to

gate valve and ion pumps to 150 °C. The multi-coil slower, described in Section 4.4, is heated to 100 °C by running 8 amps through each of the coils without any water or air cooling.

When the entire system is hot, the temperature of the oven is slowly increased. Initially, the oven outgasses considerably. The pressure in the oven region is monitored and kept near 10^{-5} torr while gradually increasing the oven temperature. After a few hours, the pressure begins to fall and the oven temperature reaches it's normal operating temperature (Table 4.1). At this point the oven is turned up to 550 °C a few times for half-hour periods over the course of $4 - 5$ hours.

Once the oven is clean, the oven is turned down to 200 °C and the ion pumps are turned on. With the pressure in the vacuum system still near 10^{-6} torr, the ion pumps saturate after about 1 h [69] of operation. Since the vacuum system takes longer than an hour to cool, shutting off the bakeout before the pressure drops further will lead to a clean system with saturated ion pumps.

After the bakeout has continued for a few days (depending on the initial state of the system) and the pressure has reached the 10^{-7} torr range in both regions, the ion pump saturation time approaches 24 h. Then, the bakeout can be terminated. During cooling, the ionization gauges must be degassed. By the next day, the pressure in the oven pumping chamber will be near

---

350-375 °C. Even though this is below the specified maximum of 400 °C, the high temperatures caused some copper gaskets to fail. Bakeout temperatures of 250 °C sufficiently clean a system without hydrocarbon contamination [68].

7×10^{-10} torr and 10^{-10} torr in the trapping region.

After subsequent experimental runs, the pressure in the system continues to drop. This is perhaps due to a cleaner oven and due to the gettering properties of lithium which gradually plates the inside of the vacuum system. The best pressures achieved without the oven on are 6×10^{-10} torr in the oven region and 6×10^{-11} torr in the trapping region.

Shutdown Procedure

To prevent contamination of the vacuum system and additional bakeouts, special precautions must be taken when shutting the vacuum system down. First, the oven must be cool and the turbopump must be off and no longer spinning. Then, the ion pumps are shut off. Argon gas is connected to the open end of the 2 PSI relief valve and the pressure adjusted to open the relief valve (which is 2 PSI above the local air pressure). Next, valve (C) is opened and argon gas is allowed to pressurize the system. The pressure valve closes because the vacuum system is swallowing the argon, therefore lowering the pressure in the valve. When the relief valve opens again, the system is pressurized slightly above the room pressure.

Then valve (A) is slowly opened. Once valve (A) is opened, the relief valve closes again. After about 30 s, the relief valve opens again. Once that occurs, valve (B) is slowly opened the system is purged with argon for a few minutes. After purging, valve (B) is closed. Once the relief pressure valve opens for a final time, valve (C) is closed and the argon is disconnected. The vacuum system is left slightly overpressurized to prevent the lithium from contamination.

The relief pressure valve (D) plays a critical role in bringing the system up to atmospheric pressure. It allows one to crudely monitor the pressure in the system and prevents too much overpressurization. While the current valve has a relief pressure of 2 PSI, a lower relief pressure would be adequate and less hazardous to fragile components like the windows.

4.3 The Lasers

Three lasers were used in the experiment. A Coherent Innova Model 310 Argon Ion Laser served as the workhorse of the optical system by pumping a Coherent Model 699-21 Dye Laser. The third laser, only used as on occasional diagnostic, was a PS011-00 CircuLaser Diode from Blue Sky Research. In this section, I briefly describe the operation of these lasers.

The ion laser operates on the visible lines of argon and supplies 6 W of power to the dye laser in light regulation mode. With the aperture of the argon-ion laser set at 8 [70], it provides a good Gaussian TEM_{00} mode for pumping the dye laser. At this power and aperture setting, the ion laser tube voltage and current are usually near 200 V and 45 A. Aside from occasional cleaning, the ion laser does not require much maintenance.

The ion laser beam enters the dye laser and illuminates a thin stream of

Element	Birefringent Filter	Thin Etalon	Thick Etalon
FSR (GHz)	400	225	10

Table 4.2: The free spectral range (FSR) of the tuning elements in the dye laser.

LD688 dye dissolved in 2-phenoxyethanol.[3] So that the laser optics have the appropriate reflectivity at 671 nm, the Coherent DCM dye optics are used in the laser.

A ring cavity built around the dye stream amplifies the fluorescence from the dye. The exact wavelength that is amplified depends on the setting of three elements: a birefringent filter, and thick and thin etalons [71, 72]. Each of the tuning elements creates wavelength depend losses in the cavity. The free spectral range (FSR) of each element is contained in Table 4.2. The modes of the tuning elements, separated by their respective free spectral ranges, are shifted in frequency by using knobs on the laser.

The longitudinal modes of the laser are separated by 150 MHz and are shifted by rotating a thin glass plate etalon mounted inside the cavity. Slight rotation of the plate causes a small changes in the length of the ring cavity which in turn changes the longitudinal mode spacing and location. By adjusting and overlapping the modes of the tuning elements and a longitudinal mode, the desired wavelength may be selected.

The combination of LD688 dye and 2-phenoxyethanol solvent has a number of advantages over the traditional DCM-ethylene glycol combination [73].

---

[3] LD688 is purchased from Exciton, Inc. and 2-phenoxyethanol is purchased from Penta Manufacturing.

Due to the mutagenicity of DCM, LD688 is much safer to use. Secondly, DCM produces only 400 mW of single mode power at 671 nm, the wavelength of the lithium D_2 line. However, the LD688 mixture produces over 700 mW single mode at this wavelength. Also, because ethylene glycol is extremely hygroscopic, the DCM dye will deteriorate after mixing, even when not in use. The lifetime of the LD688 mixture, however, depends mainly the number of hours in operation.

To achieve the maximum output power, 1.17 g of LD688 is mixed into a liter of 2-phenoxyethanol. Because this concentration nearly saturates the dye, ultrasonic mixing for at least eight hours is required to fully dissolve the dye. As with all dyes, the output power drops gradually with usage. The LD688 mixture is replaced after about four weeks of daily operation which corresponds to a final output power of 400 mW.

While there are many advantages to using LD688 over DCM, the use of LD688 does have some disadvantages. Because phenoxyethanol has a lower heat capacity than ethylene glycol, the dye is more prone to overheating where the pump laser is focussed into the dye stream. Consequently, the focus of the pump beam may not be positioned at the dye stream as desired. This causes the dye laser to output an astigmatic beam and makes alignment of the laser much more difficult. The astigmatism of the dye laser beam is corrected using anamorphic prisms located at the output of the laser.

The PS011-00 CircuLaser Diode consisted of a 30 mW SDL-7311-G1 diode with a microlens attached by Blue Sky Research. The microlens improves the output quality of the laser by making the elliptical output of the SDL diode more circular. This laser was used only when checking the operation of the Zeeman slower.

An external diffraction grating which can be rotated by a piezoelectric crystal provides single-mode frequency selection for this laser. The mode separation of the cavity formed by the diffraction grating is 3.8 GHz. To tune the laser to the appropriate wavelength, the angle of the diffraction grating and the temperature of the laser is adjusted. The diode laser operates inside a hermetically sealed, temperature stabilized box. The current [74], temperature [75], and piezo-crystal controllers were based on designs developed by D. Gauthier at Duke University.

4.4 Multi-Coil Zeeman Slower

In Section 3.2, I explain why a lithium MOT loaded from a slowed atomic beam captures more atoms than a vapor cell MOT. Simply put, a vapor cell MOT for lithium does not capture the maximum number of atoms. In this section, the method used to decelerate the atomic beam and the required apparatus are described.

4.4.1 Background

The radiation scattering force is used to decelerate atomic beams. As shown in Figure 4.5, when an atom absorbs a photon from a laser beam, it's momen-

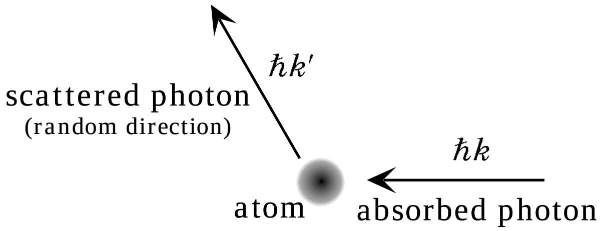

Figure 4.5: Photons absorbed and spontaneously emitted by an atom.

tum changes by $\hbar k$ in the direction of the laser beam. For ^{6}Li, the momentum change corresponds to a 10 cm/s change in the atom's velocity. If the excited atom spontaneously decays it will emit the photon in a random direction. While the momentum changes due to the random emission of photons averages to zero, those due to absorption create a significant force called the scattering force. The magnitude of the scattering force is given $\hbar k\Gamma_{sc}$, where k is the photon wavevector and Γ_{sc} is the rate at which photons are scattered by the atom [76, 77].

Since the slower beam interacts with the closed cooling transition,

$$|F' = 5/2, m_{F'} = 5/2\rangle \leftrightarrow |F = 3/2, m_F = 3/2\rangle,$$

the scattering rate can be easily calculated using the density matrix in the two-level atom approximation. If Γ is the excited state decay rate, the photon scattering rate for a single atom is given by

$$\Gamma_{sc} = \frac{\Gamma}{2}\frac{s}{1+s+4(2\pi\Delta/\Gamma)^2} \tag{4.8}$$

$$\Delta = \Delta_0 = \omega - \omega_0 \tag{4.9}$$

where s is the saturation parameter, ω is the laser frequency, ω_0 is the atomic resonance frequency, and all the frequencies have units of Hz.. The saturation parameter is given by

$$s = 2(2\pi\Omega)^2/\Gamma^2 = I/I_{sat} \tag{4.10}$$

where Ω is the optical Rabi frequency as in (3.7) and (3.9), I is the laser beam intensity given in (3.8), and I_{sat} is the saturation intensity. For the closed cooling transition in ^{6}Li, I_{sat} is

$$I_{sat} = \frac{c\pi h\Gamma}{3\lambda^3} = 2.55\,\mathrm{mW/cm^2} \tag{4.11}$$

where λ is the wavelength of a resonant beam and c is the speed of light.

Thus, the scattering force is

$$F_{sc} = \frac{\hbar k\Gamma}{2}\frac{s}{1+s+4(2\pi\Delta/\Gamma)^2} \tag{4.12}$$

If $I \gg I_{sat}$ then $s \gg 1$ and (4.12) becomes

$$F_{max} = \frac{\hbar k \Gamma}{2}. \tag{4.13}$$

This maximum of the scattering force corresponds to an acceleration a_{max} of $1.83 \times 10^6\,\mathrm{m/s^2}$ for ^{6}Li, or nearly 200,000 times the acceleration due to gravity!

To slow an atomic beam, the laser beam counterpropagates with the atomic beam, thereby opposing the atoms' motion. However, in the atom frame, due to the Doppler shift, the detuning becomes $\Delta = \Delta_0 + v/\lambda$, where v is the velocity of the atom. Consequently, if the atom is resonant with the laser frequency at one velocity, as the atom slows, it will go out of resonance. The change in velocity δv imposed by this resonance limit is given by $\delta v \approx \lambda \Gamma$ and for ^{6}Li is just 25 m/s. In order to continually slow an atomic beam over larger changes in velocity, the Doppler shift must be compensated.

References [27, 77, 78] discuss the methods researchers have developed to compensate for the changing Doppler shift in slowing atomic beams. The two most popular methods are chirping the laser frequency [79, 80] and Zeeman tuning the atomic transition frequency [2]. Chirping the laser frequency to compensate for the changing Doppler shift produces a pulsed source of slow atoms and many atoms miss the slowing cycle. This experiment uses Zeeman compensation which efficiently produces a continuous source of slow atoms.

Incorporating the presence of the magnetic field into the detuning, we get

$$\Delta = \Delta_0 + v/\lambda - \Delta_B. \tag{4.14}$$

In the presence of a magnetic field B, $|F' = 5/2, m_{F'} = 5/2\rangle$ is shifted by $2\mu_B B/h$ and $|F = 3/2, m_F = 3/2\rangle$ by $\mu_B B/h$, where μ_B is the Bohr magneton. Thus,

$$\Delta_B = 2\mu_B B/h - \mu_B B/h = \mu_B B/h \tag{4.15}$$

Since we want to create a magnetic field where the atom is resonant with the laser while it slows down, i.e. $\Delta = 0$, the expression for the magnetic field as a function of position is

$$B(z) = h/\mu_B(\Delta_0 + v(z)/\lambda). \tag{4.16}$$

If constant deceleration is assumed,

$$B(z) = h/\mu_B(\Delta_0 + \frac{1}{\lambda}\sqrt{v_i^2 - 2az}) \tag{4.17}$$

where v_i is the velocity of the atom at $z = 0$ and a is the constant deceleration. For most slowers, $a = \alpha a_{max}$ where $.5 < \alpha < .75$ and a_{max} is the acceleration due to F_{max}, (4.13).

The shape of B is determined by α, Δ_0, the maximum initial velocity one wishes to capture, v_z^{max}, and the desired final velocity, v_f. The initial and final velocity, through simple kinematics, determine the length l of the slower which is given by $l = (v_z^{max\,2} - v_f^2)/2a$.

In some preliminary modeling of trap loading and loss rates using a slowed ^{6}Li beam, for slower lengths under 50 cm, we found that the steady state number of trapped atoms rises sharply [81]. Above 50 cm, the steady state number of trapped atoms remains relatively constant. However, this model assumes that the trapped atoms would be in the path of the atomic beam. Consequently, any *unslowed* atoms in this model contribute to the trap loss rates. The slower was built under this assumption, but in the current setup, however, the MOT forms above the beam to prevent these losses due to unslowed atoms colliding with trapped atoms.

We can determine the trap loading rate R by calculating the flux of atoms slowed to the MOT's capture velocity by the Zeeman slower. As depicted in Figure 4.6, the number of atoms leaving the oven per second with directions given by θ and ϕ and speed v is [67]

$$d\dot{N}_{v,\theta,\phi} = \frac{n_0 A_s}{\pi^{3/2}\alpha^3} v e^{-v^2/\alpha^2} \cos\theta v^2 \sin\theta dv\, d\theta\, d\phi \tag{4.18}$$

where A_s is the oven aperture area, $\alpha = \sqrt{2k_B T/m}$, and n_0 is given by (4.4).

After transforming to cylindrical coordinates to match the symmetry of

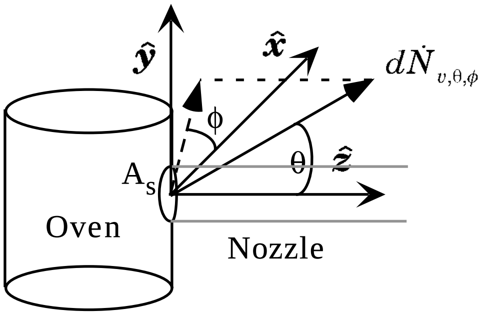

Figure 4.6: The number of atoms leaving the oven with speed v and direction (θ, ϕ).

the beam and integrating over ϕ, we get

$$d\dot{N}_{v_r,v_z} = \frac{2n_0 A_s}{\pi^{1/2}\alpha^3} v_r e^{-v_r^2/\alpha^2} v_z e^{-v_z^2/\alpha^2} dv_r\, dv_z. \tag{4.19}$$

To integrate $d\dot{N}$ we must consider the appropriate limits for v_z and v_r. Since we are calculating the number of atoms slowed per second, the range of v_z is given by $0 < v_z < v_z^{max}$ where v_z^{max} is the maximum velocity slowed. The range of v_r, however, will be the maximum of the trap capture velocity, v_c, and a collimation-limited radial velocity. Since we are calculating a lower bound on the loading rate, we will use the lowest reasonable range for v_r as determined by the collimation limit.

Because the atom's axial velocity v_z decreases as it moves through the slower, the atom does not follow a straight trajectory through the slower. Rather, the trajectory curves increasingly outward during deceleration, as shown in Figure 4.7. To determine the range of v_r for atoms that reach the trapping region we must consider the time of flight of the atoms through

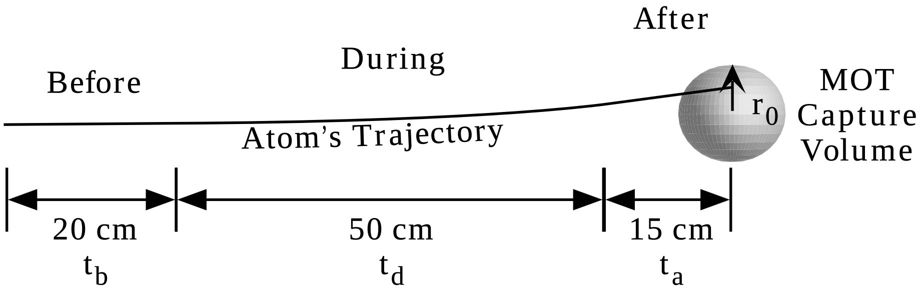

Figure 4.7: An atom's trajectory before, during, and after deceleration in relation to the trapping volume.

the slower. If r_0 is the capture radius of the MOT, the limit on the radial velocity is given by $v_r^{max} = r_0/(t_b + t_d + t_a)$ where t_i are the trajectory times (b)efore, (d)uring, and (a)fter deceleration which depends on v_z. Numerical methods may be used to integrate (4.19) with this limit on v_r [81], but we are calculating only an approximate loading rate here. The longest propagation time gives the lowest v_r^{max}.

As is shown in Section 4.4.7, the slower decelerates atoms from 1100 m/s to 40 m/s. The most significant contribution to the loading rate comes from the higher velocities since the v_z distribution peaks near the average speed of atoms in the reservoir, $\bar{v} = 1538\,\mathrm{m/s}$. The travel time from the oven to the trapping region for an 1100 m/s atom will be dominated by the propagation time t_a after slowing since the atom will have an axial velocity of only 40 m/s during that time. Since the distance between the end of the slower and the trapping volume is approximately 15 cm, the propagation time is approximately 3.75 ms. To be conservative in the estimate of the loading rate, we will double this propagation time. Since r_0 is approximately 1 cm, we will use $v_r^{max} = r_0/7.5\,\mathrm{ms} = 1.3\,\mathrm{m/s}$.

Integrating (4.19) using $v_z^{max} = 1100\,\mathrm{m/s}$ and $v_r^{max} = 1.3\,\mathrm{m/s}$ for the upper limits gives

$$R = \dot{N}(1 - e^{-v_z^{max\,2}/\alpha^2})(1 - e^{-v_r^{max\,2}/\alpha^2}) = 1.7\times 10^9\,\mathrm{atoms/s} \tag{4.20}$$

where $\dot{N}$ is determined in (4.7) at a 400 °C oven temperature.

To determine the steady state number of trapped atoms, N_{ss}, for the slower-loaded trap, we need to estimate the trap loss rate γ (3.4). Lin *et al.* measure a trap loss rate of $0.29\,\mathrm{s}^{-1}$ at a pressure of 3.5×10^{-9} torr [63]. Since γ is approximately proportional to pressure in (3.4) and the pressure in our MOT region is approximately 10^{-10} torr, we expect a $\gamma \approx 8.2\times 10^{-3}\,\mathrm{s}^{-1}$. Thus, for this slower-loaded trap, we get

$$N_{ss} = \frac{R}{\gamma} = 2\times 10^{11}\,\mathrm{atoms} \tag{4.21}$$

in the MOT. This estimate for N_{ss} is much larger than what is possible in standard magneto-optic trap since density-dependent loss mechanisms cause N_{ss} to maximize near 10^8 atoms. However, this estimate does show that our slower-loaded lithium MOT will perform much better than the vapor cell lithium MOT, described in Section 3.2.

4.4.2 Magnet Design

Rather than building a single tapered coil to create the magnetic field in (4.17), the slower was built with ten adjacent equal size coils. The multi-coil slower provides additional flexibility and solves a number of difficult design issues inherent in a single-coil approach.

First, with identical currents in all ten coils and the slower's cooling system off, the slower acts as a bakeout heater for the portion of the vacuum system it encloses. Since a single-coil Zeeman slower with a spatially varying number of wraps has a nonuniform power dissipation, it is not ideal for use as a heater. Another element must be incorporated into the magnet design to facilitate bakeout. In a multi-coil slower, the additional heating element is not necessary.

Winding the coils in the multi-coil Zeeman slower did not require as much precision as winding a single-coil Zeeman slower because the current supplied to each coil can compensate for errors in construction. Although ten constant current power supplies were required, once the supply was designed, it was easily replicated using circuit board etching technology.

Since the multi-coil slower can create the Doppler compensating magnetic field at an arbitrary Δ_0, no external magnetic offset coils are needed for final velocity selection. In addition, the final slowed velocity can be adjusted by tweaking the final coil in the slowing process.

The ten-coil slower was modelled before it was built to make sure it could generate the desired magnetic field (4.17) using power supplies already

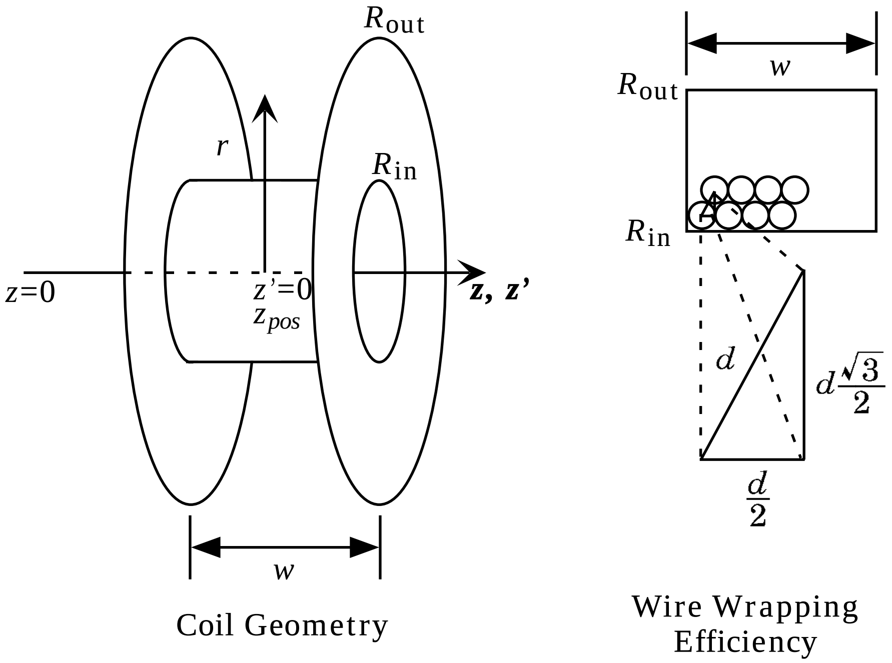

Coil Geometry

Wire Wrapping Efficiency

Figure 4.8: Coil geometry and wire wrapping efficiency.

available in the lab. As can be seen in Figure 4.8, the current density, J, for a spool of wire is given by

$$J = \frac{I}{d^2}\left(\frac{2}{\sqrt{3}}\right)^{\alpha} \tag{4.22}$$

where I is the current in the coil, d is the diameter of the wire, and α is the efficiency of the winding. An α of 1 corresponds to the most efficient winding for round wire. Despite good intentions, most coils end up with an empirically determined $\alpha \approx -1$, indicating inefficient winding.

The magnetic field $B(z)$ along the axis of the coil is given by

$$B(z) = \int_{R_{in}}^{R_{out}} dr \int_{-w/2}^{w/2} dz' \, \frac{J\mu_0}{2} \frac{r^2}{\left[(z-(z_{pos}+z'))^2+r^2\right]^{3/2}}. \tag{4.23}$$

Here, $R_{in(out)}$ is the inner (outer) radius of the coil, w is the width of the coil, μ_0 is the permeability of free space, and z_{pos} is the position of the coil center along the axis as shown in Figure 4.8. Performing this integral gives

$$\begin{aligned} B(z) = \frac{J\mu_0}{4} \Bigg\{ & a(z) \ln \left[\frac{2R_{in} + \sqrt{a(z)^2 + 4R_{in}^2}}{2R_{out} + \sqrt{a(z)^2 + 4R_{out}^2}} \right] \\ & + b(z) \ln \left[\frac{2R_{out} + \sqrt{b(z)^2 + 4R_{out}^2}}{2R_{in} + \sqrt{b(z)^2 + 4R_{in}^2}} \right] \Bigg\} \end{aligned} \tag{4.24a}$$

$$a(z) = 2z_{pos} - 2z - w \tag{4.24b}$$

$$b(z) = 2z_{pos} - 2z + w \tag{4.24c}$$

To determine the voltage required to drive the coil at the desired current, the resistance of the coil must be calculated. Using the formula for a finite arithmetic series [82], for $d \ll R_{in}, R_{out}$ the length, l, of wire used in the coil is

$$l = \frac{\pi w}{d^2} \left(\frac{2}{\sqrt{3}} \right)^{\alpha} (R_{out} - R_{in})(R_{out} + R_{in}). \tag{4.25}$$

The resistance of the coil is then given by $4\rho(T)l/\pi d'^2$ where d' is the actual diameter of the metal wire inside the insulation, and $\rho(T)$ is the temperature dependent resistivity. For copper [83], $\rho(T) = \rho_0(1 + \kappa(T - 20\,^{\circ}\mathrm{C}))$ with

$\rho_0 = 1.7\times10^{-8}\,\mathrm{Ohm}\cdot\mathrm{m}$ and $\kappa = 3.9\times10^{-3}\,/\,^\circ\mathrm{C}$. If a particular coil will carry a significant amount of current, it's temperature may rise 100 °C above room temperature, changing it's resistance by more than 30%. By varying the wire gauge and coil geometry, a set of coils was found with reasonable voltage and current requirements.

The magnet wire used in the slower coils is 12 AWG round copper heavy coated Armored Poly-Thermaleze from Phelps Dodge, rated to 200 °C. Each coil had approximately 390 winds, with an inner diameter of approximately 1.69 in., an outer diameter of approximately 5 in., and a width of 1.94 in.

Figure 4.9 shows a side view and cross sectional view of our multi-coil Zeeman slower. Because it was unclear how difficult the UHV would be to attain, the vacuum flanges were mounted to the vacuum tube before the rest of the coil was assembled. Consequently, the copper sheath and copper fins were assembled in halves before they were mounted to the vacuum tubing. Since the cleaning procedures for UHV are not that difficult, it would have been easier to assemble the sheath and fins in one piece, simply slide the assembly over the vacuum tube, and then weld the flanges.

The vacuum system tubing is 1.5 in. od. and is mounted to 2.75 in. flanges. The 1/16 in. thick copper cooling fins are soft-soldered to the 3/32 in. thick copper sheath in order to provide cooling to the inner windings of the coils. Each cooling fin was cooled on both sides by water flowing through 1/4 in. od. copper tubing, also attached by soft-solder. The copper assembly was temporarily attached to the vacuum system using hose clamps until the coils

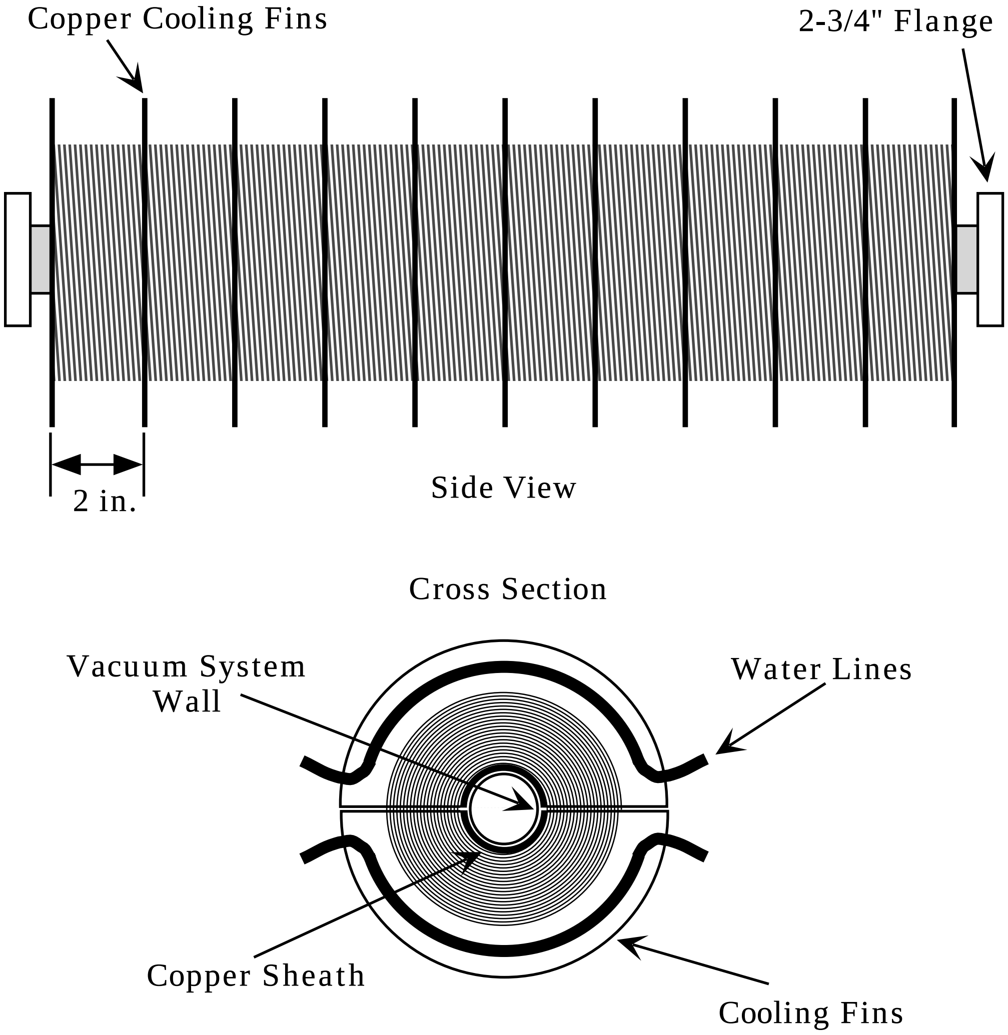

Figure 4.9: The multi-coil Zeeman slower.

were wound, permanently holding it in place. Additional cooling is provided by three fans mounted above the slower coils.

The temperature is limited to 100 °C when baking out the slower because soft-solder was used to join the copper pieces. Silver-solder which can withstand much higher temperatures would have been a better choice for bonding the copper. Then, the bakeout temperature would be limited to 200 °C due to the magnet wire.

The power for the coils was generated by four Sorenson 5 V-100 A supplies, and one Sorenson 10 V-120 A supply. The power from supplies was divided among the coils using ten identical adjustable current supplies of our own design.

4.4.3 Slower Current Supplies

The schematic for one of the slower current supplies is shown in Figure 4.10 and the circuit board mask for the supply is shown in Figure 4.11. A -10 V reference voltage is divided by a front panel potentiometer and sent to a summing amplifier which sums an optional front panel BNC voltage. The total voltage is reduced by a factor of 25 and sent to an op-amp which maintains an equal voltage, V_m, across a high-power $.02\,\Omega$ resistor. Changes in the current in the coil apply negative feedback to the op-amp which counteracts those changes. V_m is calibrated by an on-board potentiometer to measure the current through the coil and sent to a central board for display.

The setting of a rotary switch connected to the central board determines

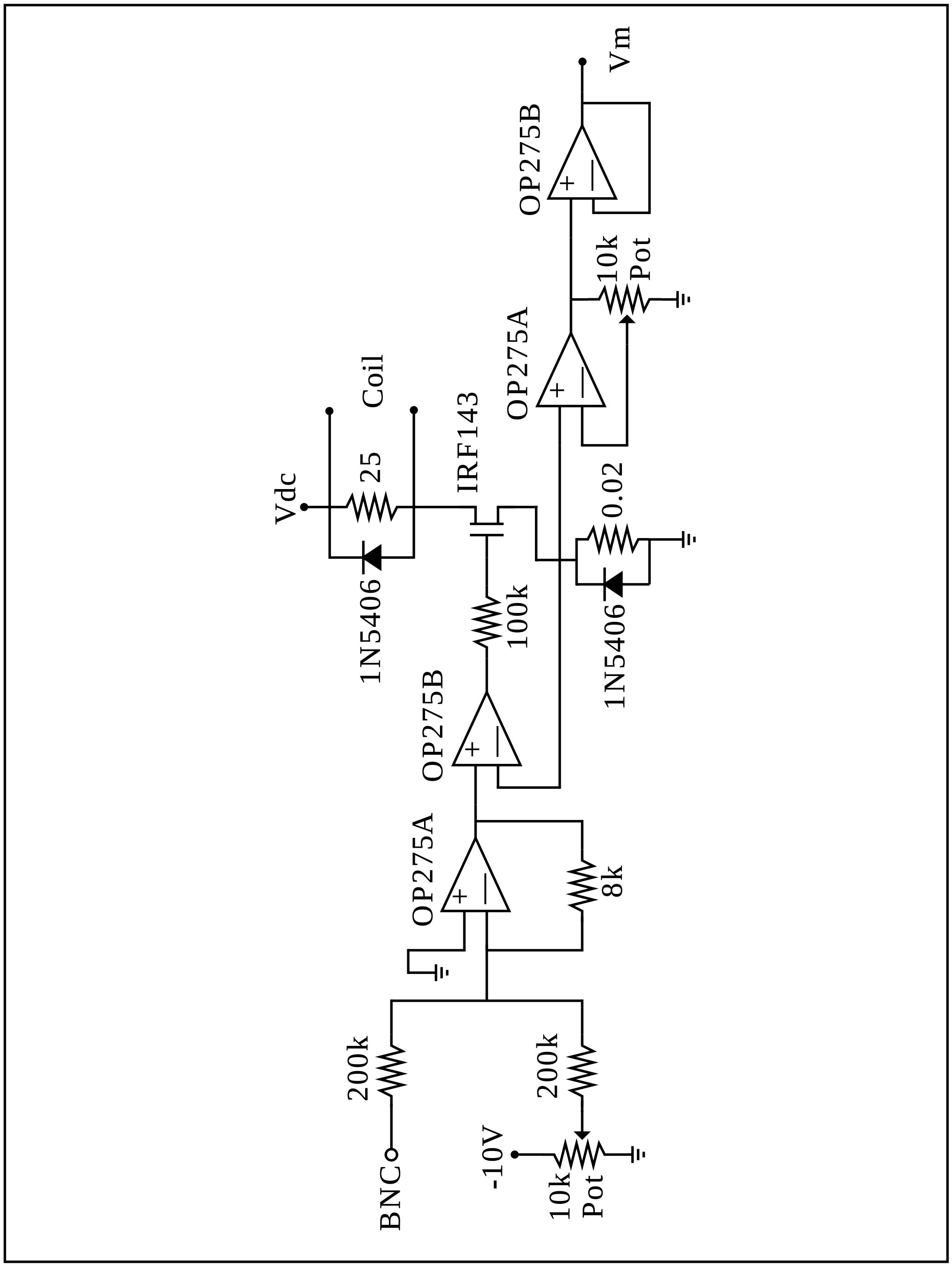

Figure 4.10: A diagram of the slower current supply.

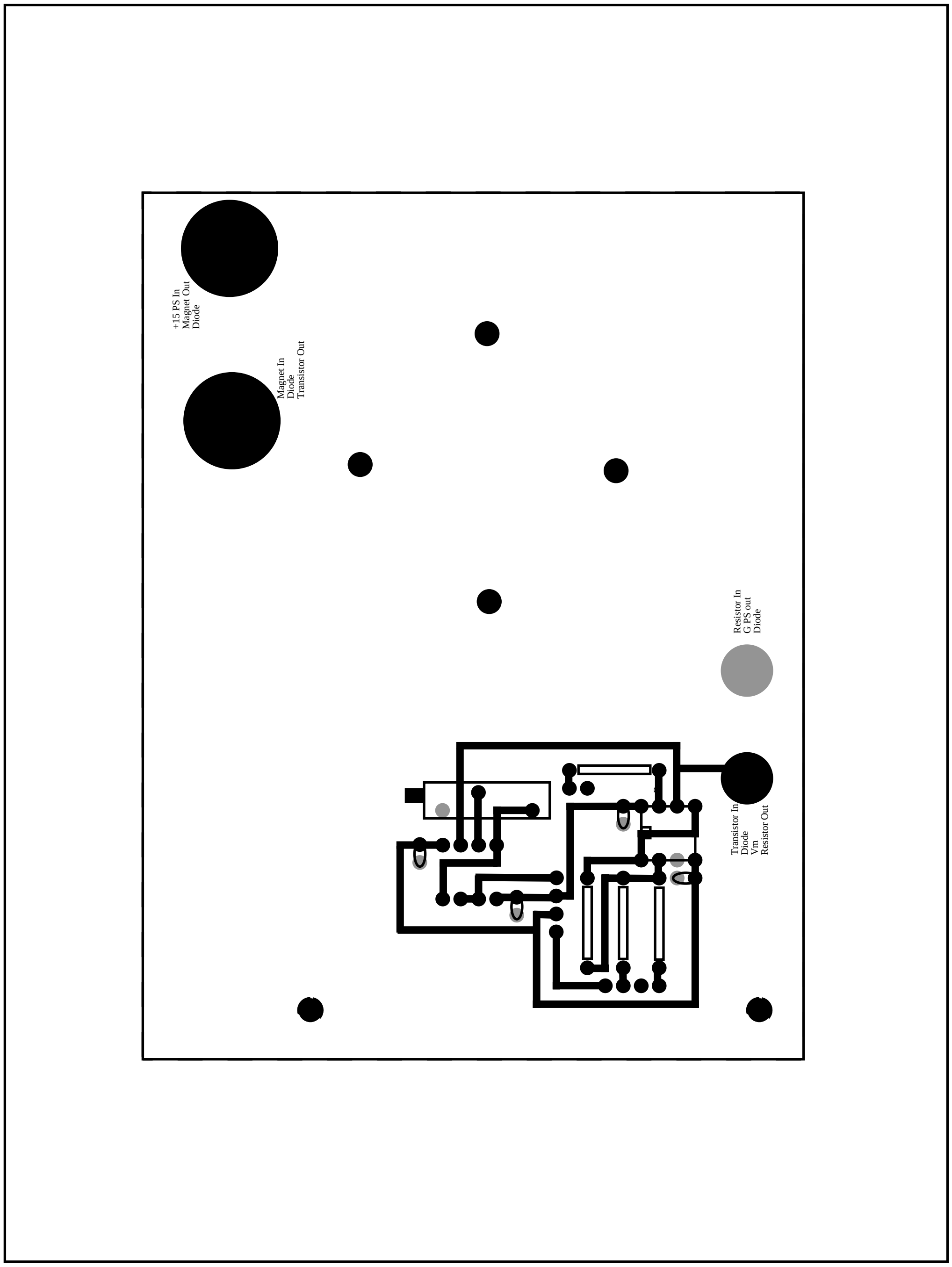

Figure 4.11: The circuit mask for the slower current supply.

which current is displayed on a panel-mounted backlit LCD. In addition to running the display, the central board provides the $-10\,\mathrm{V}$ reference to each supply along with power for the integrated circuits on each board. The circuit board mask for the main board is shown in Figure 4.12. The transistors were mounted on separate water cooled copper plates.

The $25\,\Omega$ resistor in parallel with the coil was added to provide stability to the circuit since the inductive load presented by the coil tended to cause oscillations in the circuit. Even though we compensate for the parallel resistor in our current measurement by adjusting the on-board potentiometer, temperature dependencies of the coil and resistor may cause the current in the coil to drift. To minimize this effect, we calibrated the coil current near the operating current and after the electronics had warmed up.

The grounds between the ten supply boards differ due to the high current flowing through the coils. As originally built, the displayed value of the current changed by $< .05\,\mathrm{A}$ depending on the settings of the other coils. To fix this, a probe was added to the display that references each coil current measurement to the appropriate current supply ground.

Although there are a few minor problems with this circuit design, overall, the current supplies perform quite well. Improvements to the circuits that eliminate the problems described above are reported in Section 4.5.2.

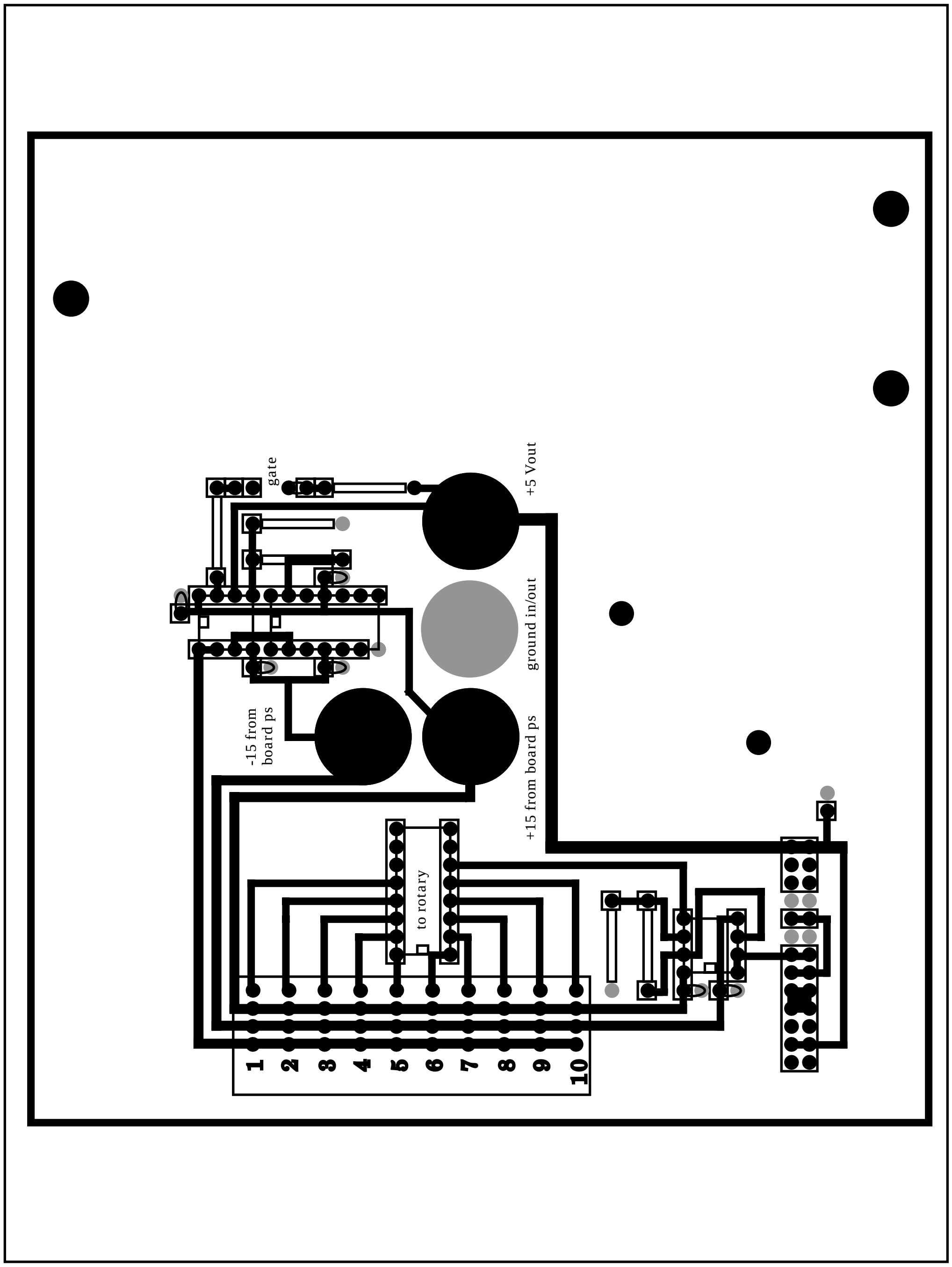

Figure 4.12: The circuit mask for the slower main board.

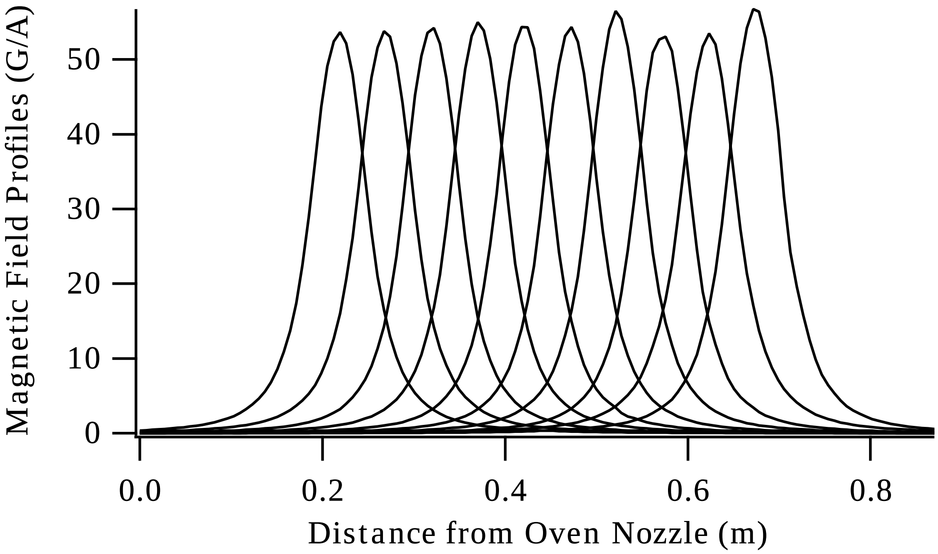

Figure 4.13: Magnetic field profiles of the slower coils.

4.4.4 Coil Configuration

After winding the coils and completing the current supplies, the magnetic field produced by each coil was measured using a Bell Model 620 Gaussmeter. Figure 4.13 shows the magnetic field per amp for each of the coils. The data taken by characterizing each of the ten coils is used in an eleven-parameter function that is fit to the desired magnetic field. Ten of the parameters returned by the fitting program determine the coil currents. The eleventh parameter describes a simple shift in position axis. Because the $z = 0$ point in (4.17) occurs when slowing begins, and $z = 0$ in the coil functions is at the nozzle output, this offset is necessary. Figure 4.14 shows the results of fitting the coil currents to acheive a particular field. The desired magnetic field was calculated using (4.17) with $\Delta = -1400\,\mathrm{MHz}$, $a = .5a_{max}$, and $v_i = 900\,\mathrm{m/s}$.

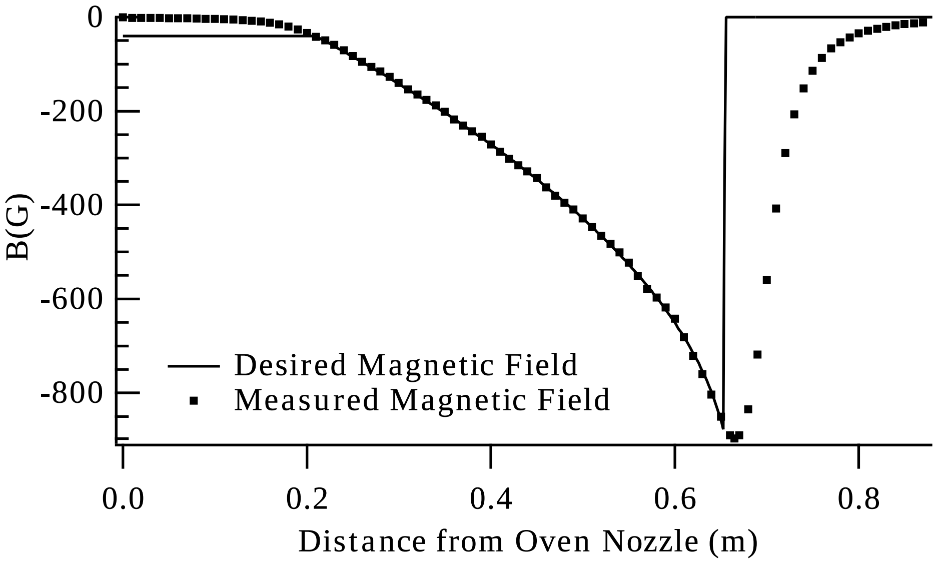

Figure 4.14: Desired and measured magnetic field profiles.

Coil	0	1	2	3	4
Current (A)	-0.39	-1.08	-1.69	-2.36	-3.04
Coil	5	6	7	8	9
Current (A)	-4.00	-4.62	-5.91	-7.57	-12.8

Table 4.3: Slower coil currents used in verifying the fitting procedure. Coil 0 is the closest to the oven nozzle.

A final velocity is chosen which determines when the desired magnetic field abruptly goes to zero, quickly taking the atom out of resonance with the slowing beam. The final velocity in this example is 100 m/s. After fitting to the desired magnetic field, the coil currents were set to those returned by the fit (see Table 4.3) and then the magnetic field in the slower was measured. Figure 4.14 shows that the slower creates a field in excellent agreement with the desired magnetic field.

The magnetic field could be verified in this case because the vacuum system had not yet been pumped down. When the vacuum system is closed, preventing access with the gaussmeter, only the coil field data and the coil currents are used to determine the slower's magnetic field.

In the example above, the slower is set to slow the atoms to 100 m/s. While this final velocity is considerably slower that the average velocity of the atoms, it is not slow enough to effectively load the MOT which has a capture velocity near 40 m/s. Slowing the atoms to such low velocities is significantly more difficult. Because the acceleration of the atoms is near $2 \times 10^6\,\mathrm{m/s^2}$, atoms will reverse direction if slowed over an excess distance of $340\,\mu$m, and they will be pushed back into the slower.

4.4.5 The atom's trajectory

To more accurately predict the final velocity of the atom, a computer program, `vtrack`, was written to model the atom's axial trajectory as it travels through the slower. `Vtrack` uses the standard Runge-Kutta and adaptive stepsize methods found in Ref. [84] to integrate the atom's equations of motion. The atom's acceleration is calculated using (4.12) where the detuning (4.14) is dependent on the atom's velocity and it's position in the magnetic field of the slower.

In the imaging experiment, $\Delta_0 = -200\,\mathrm{MHz}$ in the slower beam. With $a = .75a_{max}$, and a final velocity of 40 m/s, the maximum velocity that can be slowed is near 1075 m/s. The desired and projected magnetic fields in the

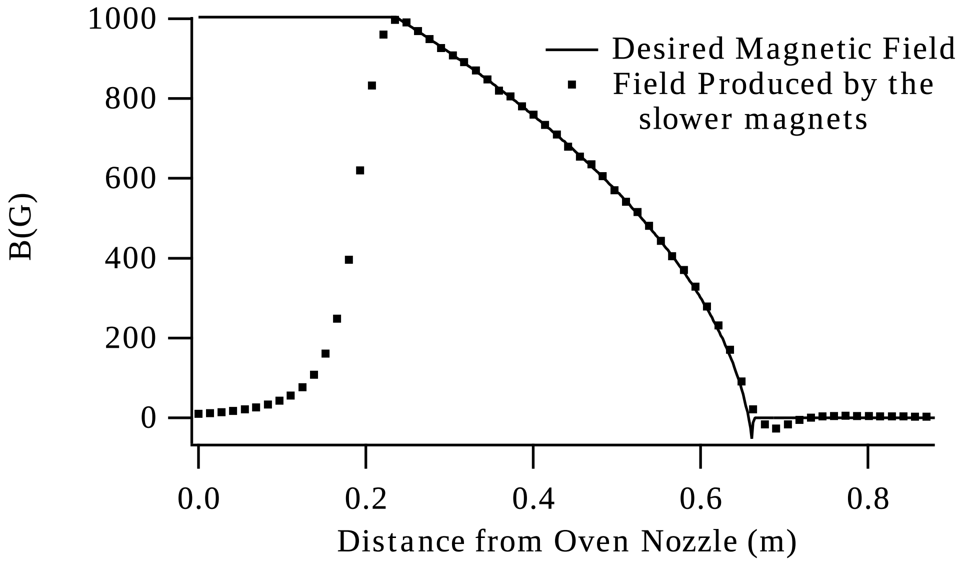

Figure 4.15: Slower field used in imaging experiment.

Coil	0	1	2	3	4
Current (A)	13.73	10.48	9.51	8.49	7.53
Coil	5	6	7	8	9
Current (A)	6.79	5.33	4.12	2.90	-1.70 to -1.95

Table 4.4: Slower coil currents used in the imaging experiment.

slower are shown in Figure 4.15 and Table 4.4 shows the current in each coil. In Figure 4.15 the the current in Coil 9 was set to 1.5 A, although in actual runs, the current in Coil 9 was peaked daily to maximize the MOT loading rate.

In Figure 4.16 the velocity that causes the atomic transition to resonate with the slowing beam is plotted as a function of the atom's position in slower's magnetic field. In addition to the resonant velocity, several computed trajectories are shown for different saturation parameters (4.10). The atom's

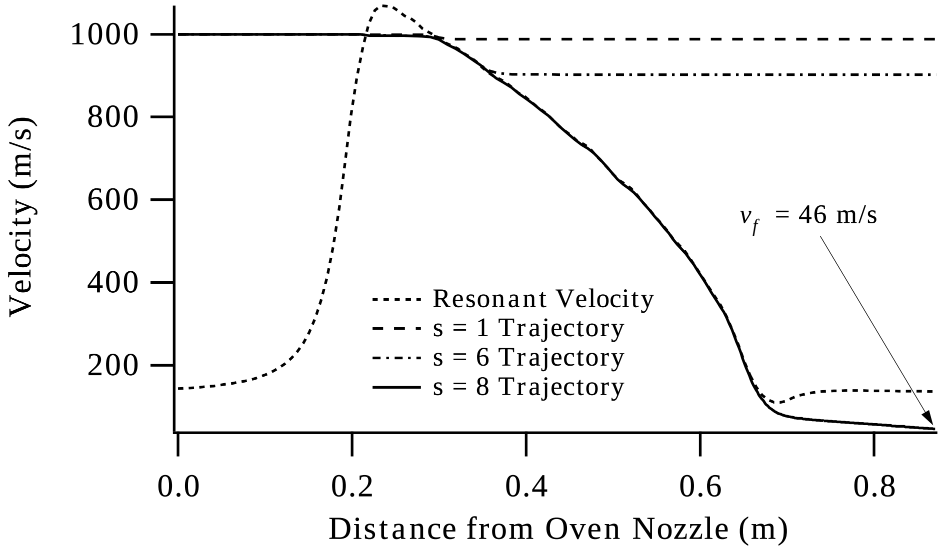

Figure 4.16: Atomic trajectories in the slower.

initial velocity is 1000 m/s. As soon as the atom becomes resonant with the slowing beam, it begins to slow. If the intensity of the slowing beam is too low, small errors in the magnetic field allow the atom to *escape* the slowing trajectory. Once the intensity of the slowing beam is large enough, the errors in the magnetic field become negligible due to power broadening of the atom's slowing transition. In this case, for $s > 6.5$ the atom will continue slowing to the desired final velocity

A slower works by bunching the velocities between the maximum slowed velocity and the final velocity. If the slower beam intensity is high enough, all atoms with initial velocities v_z such that $41 < v_z < 1075$ m/s will be bunched into the final velocity, 41 m/s. Another program, `vprofile`, essentially runs `vtrack` on a sequence of velocities. Combining the output of `vprofile` with

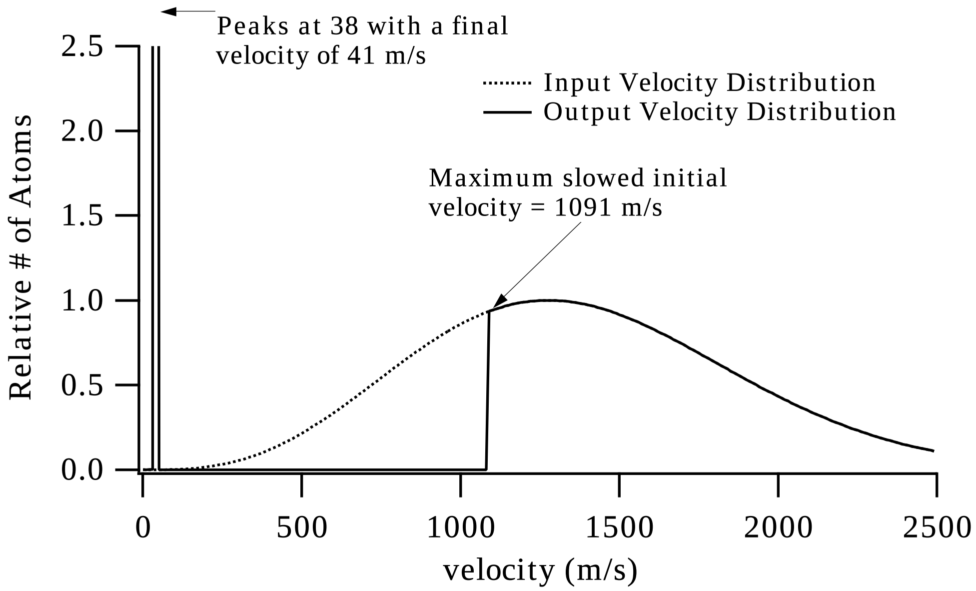

Figure 4.17: Rate of atoms entering and leaving the slower as a function of velocity.

the initial thermal velocity distribution, the bunching effect of the slower is easily seen.

Figure 4.17 shows the computed rate of atoms entering and leaving the slower as a function of velocity. The input rate is calculated from (4.20) assuming an atomic beam from a 400 °C oven, collimated to 20 mr, and normalized to peak at 1. The output rate shows that atoms with initial velocities between 1091 m/s and the final velocity, 41 m/s, all exit the slower at the final velocity.

Figure 4.18 shows the resulting rate of atoms leaving the slower as a function of velocity with a saturation parameter $s = 2$. If the slower beam is too weak, the atoms are bunched over a number of smaller velocity ranges

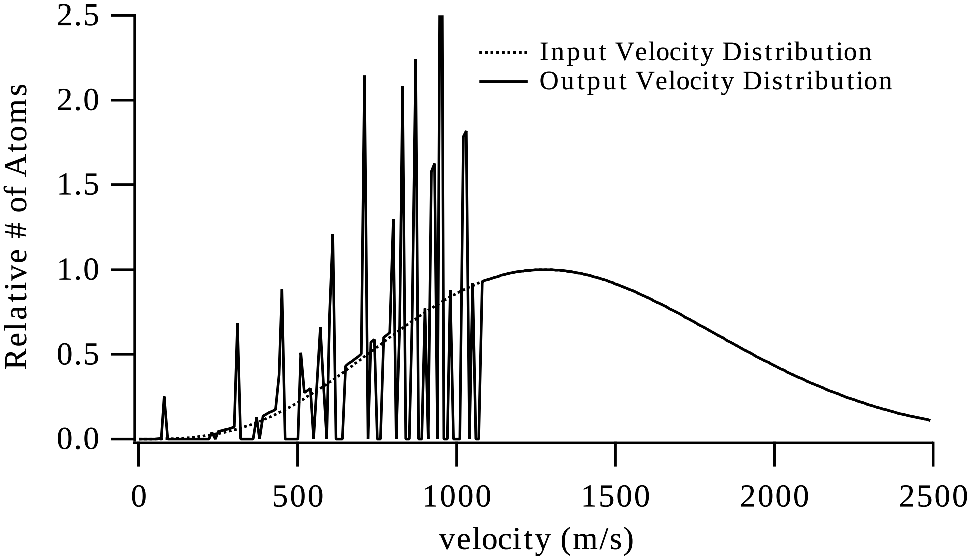

Figure 4.18: Velocity distributions with a weak slowing beam.

because errors in the magnetic field generated by the slower allow the atoms to escape from the slowing trajectory. The number of atoms with an exit velocity of the desired final velocity, 41 m/s, is significantly reduced.

In this section I have explained the methods and tools we use to determine the slower coil currents and test their adequacy. The results indicate that an intense slowing beam can be used to overcome errors in the slower's magnetic field profile. In the next section, I will discuss additional properties of the slowing beam.

4.4.6 Required Optical Fields

While the desire for an intense slowing beam arises out of the wish to compensate for possible magnetic field errors, most of the other properties of the slowing beam are chosen due to the multi-level nature of ^{6}Li. In addition to making the slowing beam intense, it is σ^+ circularly polarized, focused gradually toward the oven nozzle, and detuned 200 MHz to the red of the cooling transition, $|F = 3/2, m_F = 3/2\rangle \leftrightarrow |F' = 5/2, m_{F'} = 5/2\rangle$.

Atoms slowing from 1000 m/s must do so using nearly 10,000 photons. If the atom absorbs a photon of the wrong polarization, it may spontaneously decay to a non-resonant ground state, terminating the deceleration process. The presence of a strong magnetic field during most of the slowing process along with a σ^+ polarization slowing beam keeps the majority of the atoms cycling in the closed cooling transition. The magnetic field causes the excited state energy levels to split, detuning the transitions that are coupled by the photons with errant polarization.

As the atoms exit the oven, all the ground states of the atom are equally populated. Since the magnetic field is small at the output of the oven, the slowing beam is detuned from resonance with $|F = 3/2\rangle$ atoms by 200 MHz and with $|F = 1/2\rangle$ atoms by 428 MHz. To encourage all of the atoms to begin cycling in the cooling transition, the slowing laser beam is focused from approximately 1 cm diameter at the input of the vacuum system to a width of the nozzle diameter at the oven nozzle. Because the intensity in the slowing beam becomes so large at the focus, the $F = 1/2$ atoms absorb a few photons from the non-resonant σ^+ slowing beam. After a few cycles of absorption and spontaneous emission, the majority of the atoms end up in the $|F = 3/2, m_F = 3/2\rangle$ ground state of the cooling transition.

The power in the slower beam depended mainly on the age of the dye in the dye laser and ranged from $35 - 60\,\mathrm{mW}$. Dipole forces, which arise from the lightshift (2.14), necessitate using red-detuned light for the slowing beam. Red-detuned light creates a dipole force which draws the atom into the slower beam whereas blue-detuned light repels the atom from the beam. The amount of red detuning, 200 MHz, was chosen based on the available acousto-optic modulators in the lab. The optical layout of the slower beam and it's use in the imaging experiment are detailed in Chapter 5.

4.4.7 Observation of Slow Atoms

After the slower was installed and operational, only a few weeks were spent trying to characterize it's behavior. This section contains the data showing that the slower indeed produces slow atoms. In order to obtain this data, the oven had to run at nearly 500 °C. To maintain the life of the oven, the process of characterizing the slower was discontinued once slow atoms were produced.

A schematic for measuring the rate of atoms entering the trapping region of the MOT with a particular velocity v is shown in Figure 4.19. If the probe has a frequency ω and the atomic resonance frequency is ω_0, due to the doppler shift, only atoms with velocity $v = \lambda(\omega_0 - \omega)/\cos\theta)$ will be resonant with the probe.

In ^{6}Li there are two resonance frequencies separated by 228 MHz corresponding to atoms in either the $|F = 3/2\rangle$ or $|F = 1/2\rangle$ ground states.

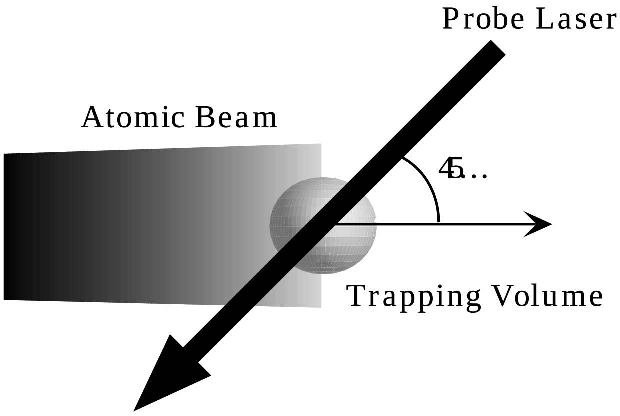

Figure 4.19: Schematic for measuring the rate of atoms entering the trapping region at a specific velocity.

Consequently, the probe will cause fluorescence in two velocity groups. However, the fluorescence from atoms cycling between $|F = 3/2\rangle$ and the excited state is significantly brighter than the other transition's fluorescence. Therefore, only the effects on the fluorescence from the resonant $|F = 3/2\rangle$ velocity group are significant.

Since the probe was linearly polarized, we can assume that the resonant atoms will emit a few photons before decaying to the non-resonant $|F = 1/2\rangle$ state. If we assume that the number of photons emitted is independent of velocity, the fluorescence measures the rate of atoms entering the probe region at the resonant velocity. If the frequency of the probe beam is scanned, the fluorescence recorded as function probe frequency may be used to determine the relative rates of atoms entering the trap at different velocities. This spectrum corresponds exactly with the calculated rates shown in Figures 4.17 and 4.18.

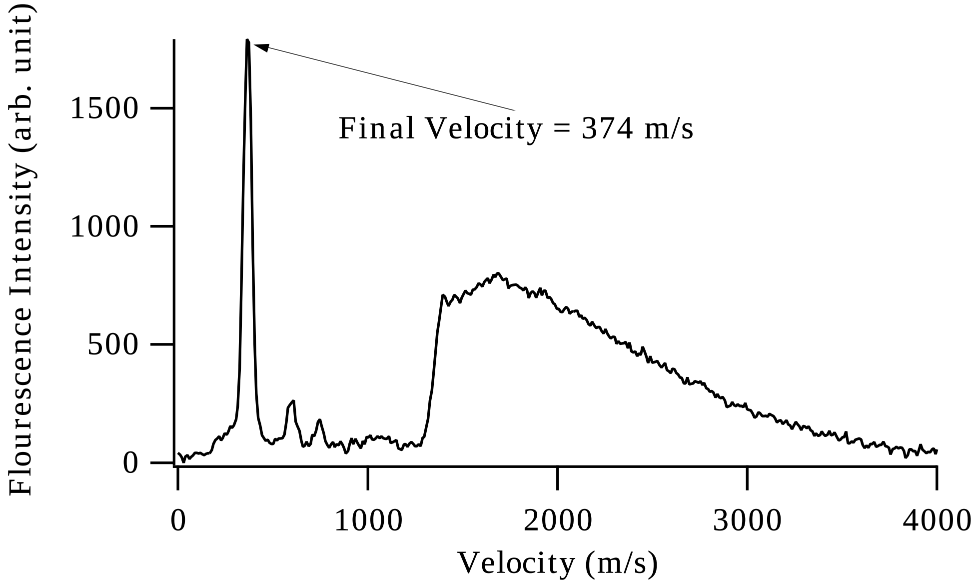

Figure 4.20: Fluorescence signal from a slowed atomic beam.

The fluorescence signal from a slowed atomic beam is shown in Figure 4.20. The probe laser was the diode laser described in Section 4.3 and the fluorescence was measured with a photo-multiplier tube. For this data, the coil currents were set to those in Table 4.3 and the magnetic field profile is shown in Figure 4.14. The velocity bunching effect shown in Figure 4.17 is clearly shown in this data, with a significant fraction of the atoms leaving the slower at 374 m/s.

Figure 4.21 shows atoms decelerated to trapping velocities. This data was taken with a slower beam detuning of $-200\,\mathrm{MHz}$ and with the coils set to the values in Table 4.4 which is how the slower operates during the imaging experiments. The peak located near 0 m/s indicates the presence of trappable atoms.

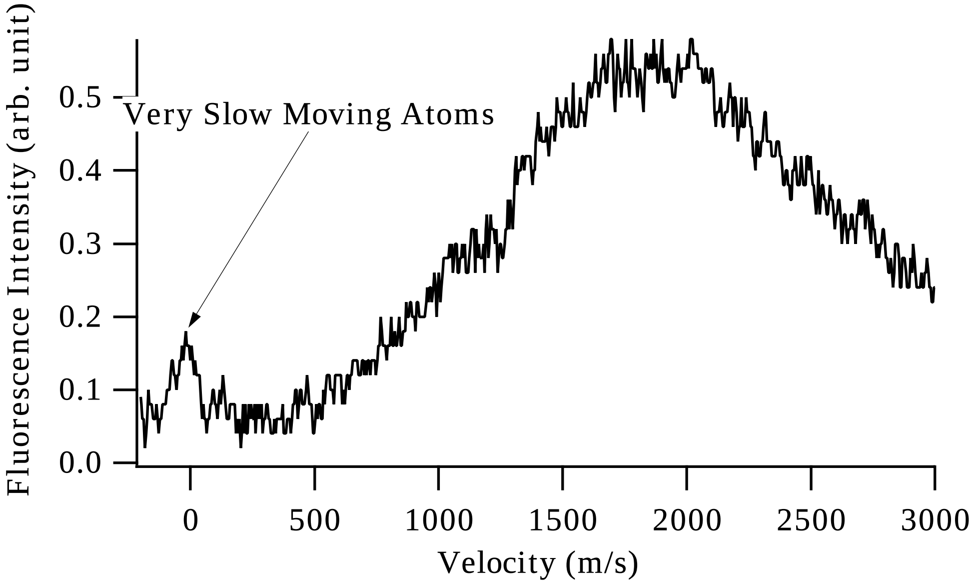

Figure 4.21: Atoms slowed to trapping velocities.

The peak shown is much smaller than that estimated by the `vprofile` in Figure 4.17. The trajectories calculated for Figures 4.17 and 4.18 do not include any dependence on radial velocity so the size of the slowing peaks are exaggerated in those figures. When atoms are slowed to such low velocities, the divergence shown in Figure 4.7 significantly affects the size of the slowed-atom peak. Also, as shown in Figure 4.20, the probe volume was not matched to the trapping volume which amplifies the effect of divergence.

4.5 Magneto-Optic Trap

Once the atoms leave the slower, they are confined by a magneto-optic trap. In this section, I will explain how the MOT operates and describe the appa-

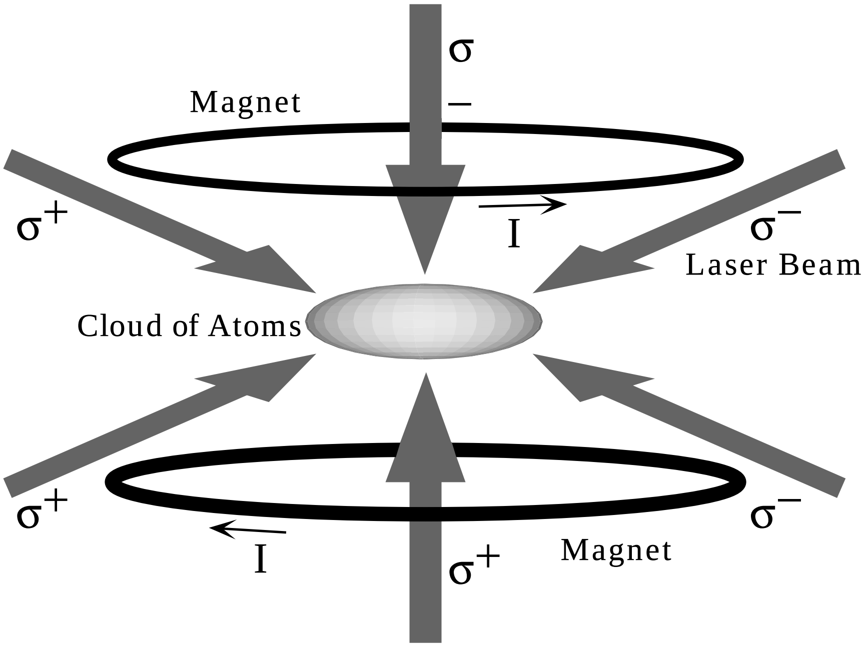

Figure 4.22: The schematic diagram for a magneto-optic trap.

ratus that was built to implement it.

4.5.1 Background and Required Optical Fields

The standard MOT [9] consists of two gradient magnets and three sets of counterpropagating laser beams, as shown in Figure 4.22. Each of the laser beams exerts a scattering force on the atom. The laser beams are detuned below resonance so that atoms moving toward any of the beams are decelerated.

In addition to the damping force, the presence of the magnets creates a spatially dependent force. Because the magnets are operated with opposing currents, they create a quadrupole field. This quadrupole field is zero in the

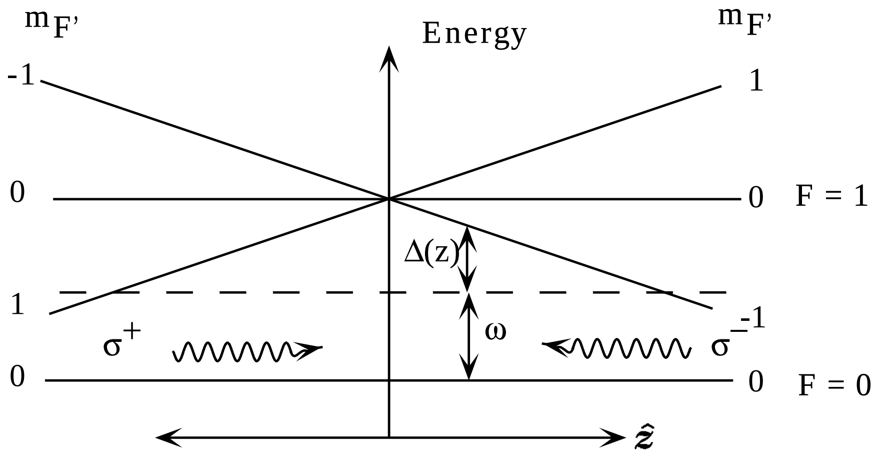

Figure 4.23: A one-dimensional energy diagram for an atom in a MOT.

center between the two magnets and increases approximately linearly in every direction from the center. Due to the $\sigma^{\pm}$ polarizations present in each beam, the Zeeman shifts caused by the magnets provide a spatial dependence to the scattering force. Consequently, the MOT both damps motion and exerts a restoring force on the atoms.

To understand the spatial dependence of the force, consider the one-dimensional energy diagram for an atom in a MOT as shown in Figure 4.23. To simplify the diagram, the energy level structure of the atom has been reduced to an $F = 0$ ground state and an $F = 1$ excited state. If an atom is displaced in the direction of positive $\hat{\boldsymbol{z}}$, the $m_{F'} = 1$ excited state is shifted away from resonance with the laser while the $m_{F'} = -1$ state is shifted closer. Because the σ^+ beam does not couple to the $m_{F'} = -1$ state, the atom preferentially absorbs photons from the σ^- beam. The differential scattering force on the atom caused by the difference in absorption creates a net force restoring the atom to the magnetic field center. A displacement in any direction from the magnetic field center causes a restoring force on the atom.

The energy level structure of lithium only adds a few complications to the workings of the MOT. The $m_{F'} = \pm F'$ states in the example lead to forces and the same holds true for ^{6}Li. As an atom moves away from the center, the differential absorption created by the Zeeman shifts will tend to push the atom into the $|F = 3/2, m_F = \pm 3/2\rangle \leftrightarrow |F' = 5/2, m_{F'} = \pm 5/2\rangle$ cooling transition. Then, lithium behaves much like the atom in the example.

The trapping beam frequency is tuned to the red of the $|F = 3/2, m_F = 3/2\rangle \leftrightarrow |F' = 5/2, m_{F'} = 5/2\rangle$ transition frequency. The linewidth of this transition is 5.9 MHz and the trapping frequency detuned below resonance by 3.5–7.5 linewidths during the course of the experiment. In this slower loaded trap, the most atoms are trapped at detunings of approximately 6.5 linewidths, or approximately -38 MHz.

Due to the presence of the six laser beams in the MOT, the quantization axis is not well defined in the center of the MOT. Consequently, excited atoms may decay to the lower hyperfine level (see Section 3.3). To return these atoms to the trapping cycle, a repumping frequency is added to each of the confining laser beams. The repumping frequency is upshifted by approximately 228 MHz to resonate with the $|F = 1/2\rangle$ atoms. The details of the optical layout are presented in Chapter 5.

Coil Pair	IR (in.)	OR (in.)	W (in.)	D (in.)	WG (AWG)
Gradient	1.5	2.88	1.75	4	12
Null A	13.2	14.68	1	3.5	14
Null B	3	5.6	1	6.5	14

Table 4.5: Physical parameters for the MOT coils. IR = inner radius, OR = outer radius, W = coil width, D = distance from the MOT to the center of the coil, WG = coil wire gauge.

4.5.2 The Magnets

Three pairs of electromagnets are used to adjust the magnetic field in the MOT. Opposite currents flow through one pair, the MOT gradient magnets, as shown in Figure 4.22. The other two pairs typically carry parallel currents and provide a method of moving the magnetic field zero into the center of the intersecting laser beams and nulling background magnetic fields.

The coils were designed using the method described in Section 4.4.2. The inner and outer radii, coil widths, distance from the center of the magnet to the MOT, and wire gauges are shown in Table 4.5 for the pairs of magnets. The gradient and B coils were wound on copper spools like the one shown in Figure 4.8. Copper tubing, 1/4 in. dia., was soldered to these coils so that they could be water cooled. The A coils were wound on a spool made of plexiglass.

Figure 4.24 shows the position of the MOT magnets with respect to the vacuum system. The on-axis magnetic field shapes of all the coils were measured using a Bell Model 620 Gaussmeter. Each gradient coil produces a gradient per amp of $0.67\,\mathrm{G/A\cdot cm}$ axially and $0.35\,\mathrm{G/A\cdot cm}$ radially at the

Coil	G1	G2	A1	A2
Current (A)	25.1	24	0	.67

Table 4.6: The MOT coil currents used during the imaging experiment.

midpoint between the magnets. Coils A1 and A2 each contribute 2.5 G/A to a uniform field along the axis of the slower. The B coils each produce 0.85 G/A. Pair A of the nulling coils allows one to shift the magnetic field center along the slower axis while Pair B allows horizontal adjustments perpendicular to the slower axis. Vertical adjustments of the magnetic field center are provided by using different currents in the gradient magnets.

For the data presented in Chapter 6, the B coils were not used. The settings of the gradient magnets and the Pair A coils are shown in Table 4.6. With the currents for the gradient coils as indicated in the table, they combine to produce a gradient of 33 G/cm axially and 16.5 G/cm radially where the atoms are captured. It is easier to null the stray magnetic fields (a procedure explained in Chapter 5) by using just one of the A coils, probably due to the small residual gradient from the slower. However, because A2 has such a large radius, it produces a negligible gradient when compared with the MOT magnets.

The magnets were controlled with a set of current supply boards similar to those used for controlling the slower magnets. The circuit board layout for the main controller board is shown in Figure 4.27 and the layout for a single current supply is shown in Figure 4.26.

Figure 4.25 contains the schematic diagram for a single current supply

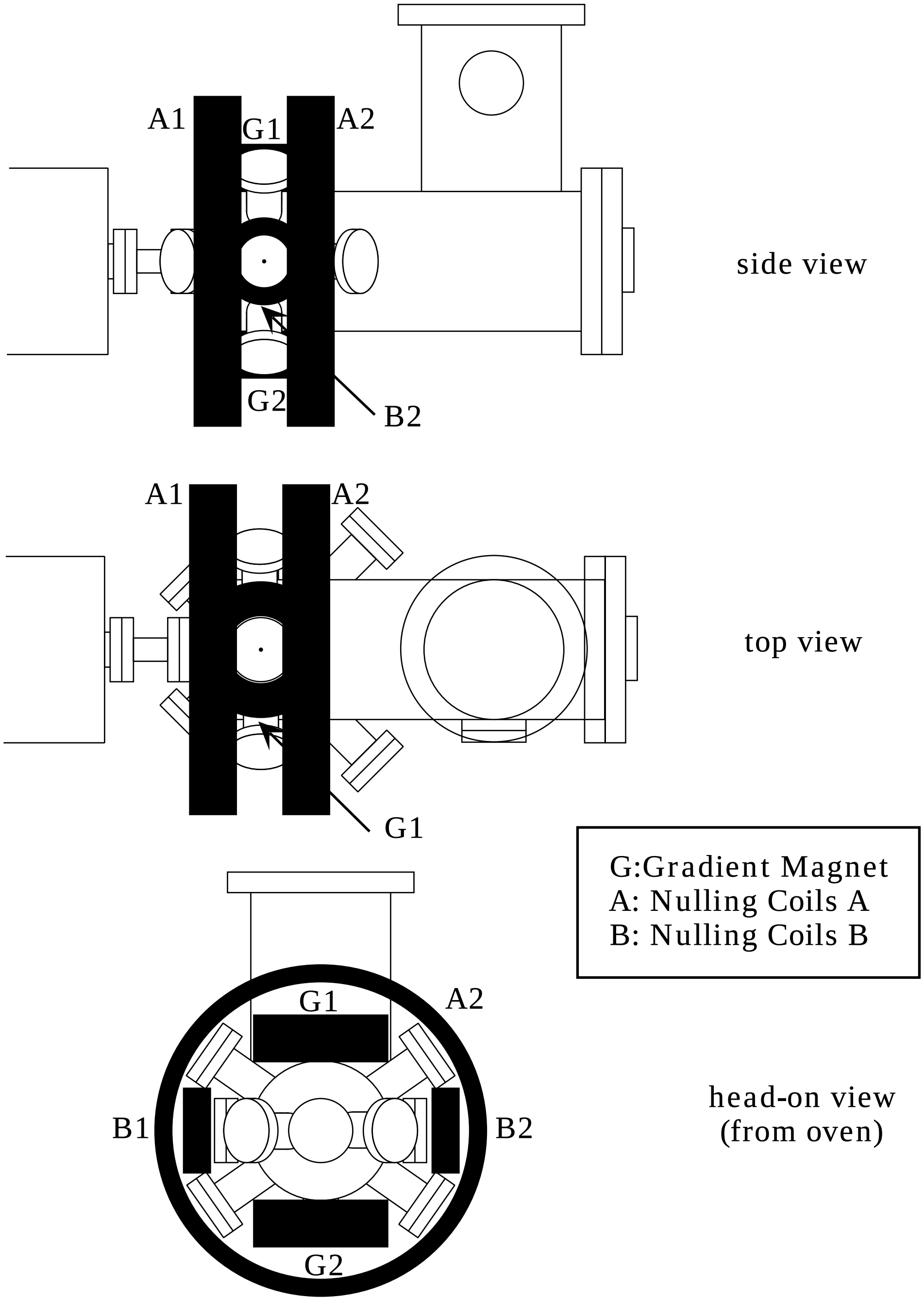

Figure 4.24: The positions of the MOT magnets.

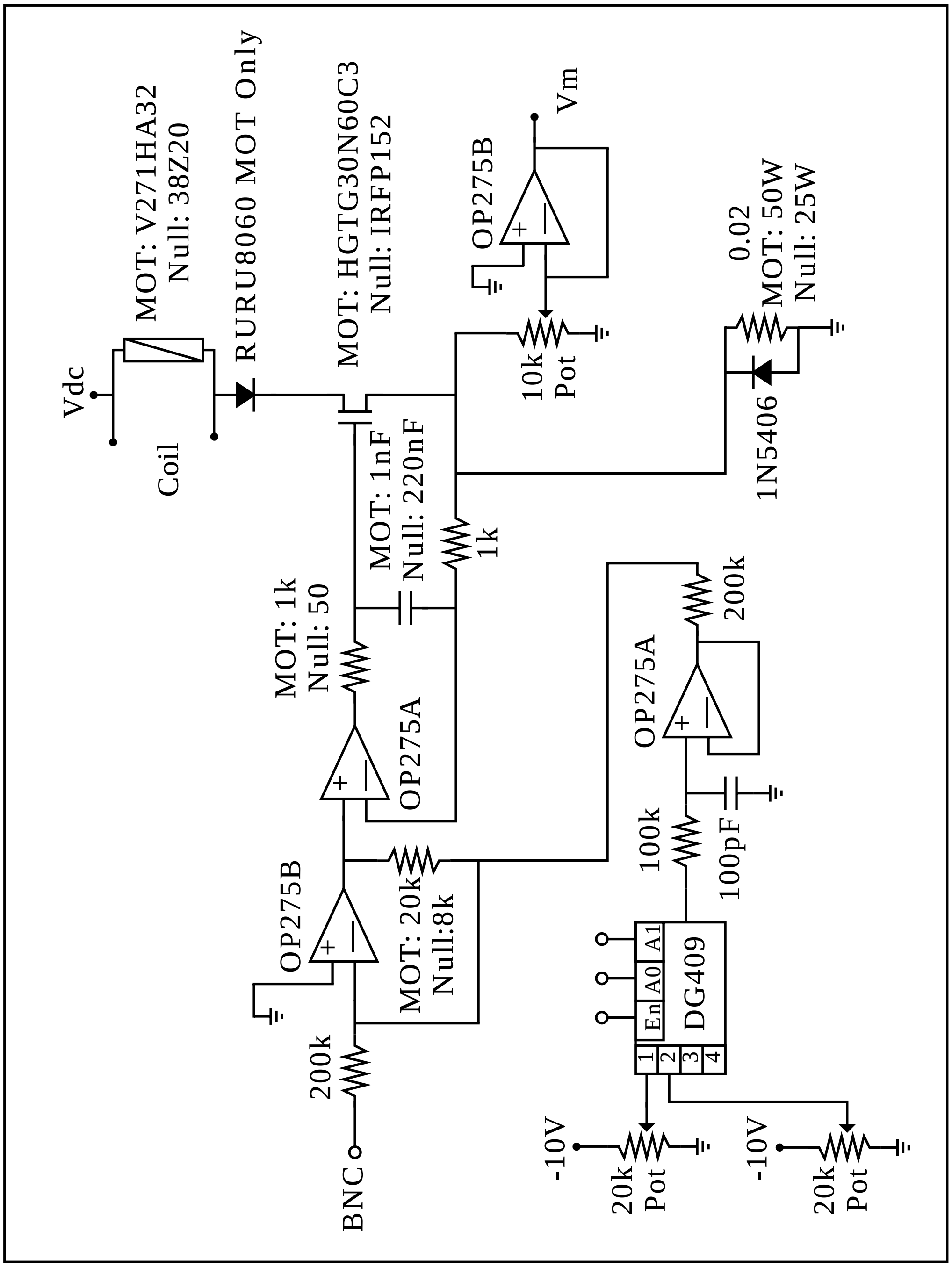

Figure 4.25: The schematic diagram for a MOT magnet current supply.

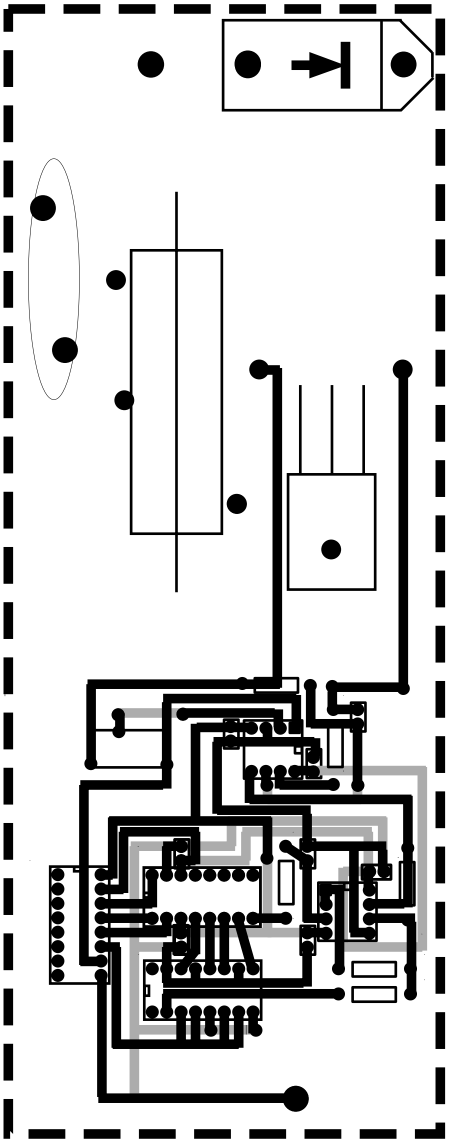

75% Scale

Gray lines indicate top surface traces and jumpers

Figure 4.26: The circuit board layout for the MOT current supply.

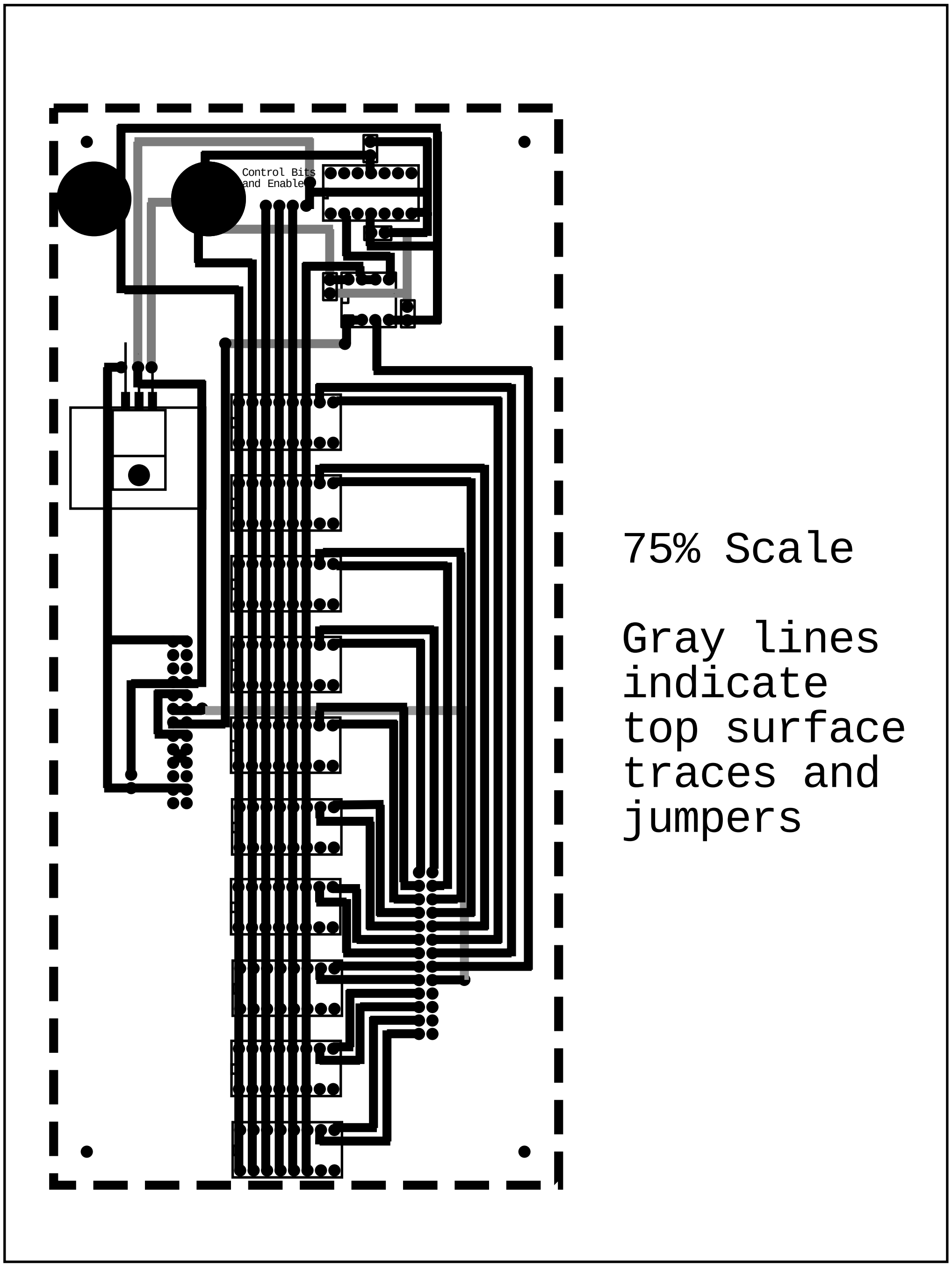

75% Scale

Gray lines
indicate
top surface
traces and
jumpers

Figure 4.27: The circuit board layout for the MOT magnet main controller board.

circuit. Differences between the circuits for the gradient and nulling coils are indicated in Figure 4.25. The digital En, A0, and A1 lines allow us to quickly switch between different current settings for each coil. The 10k potentiometers which set the current settings are located on the front panel of the supply box. The BNC input allows us to uniformly shift all the current settings at once.

A servo loop monitored the voltage across a small $0.02\,\Omega$ resistor. When the current through a coil deviates, the voltage across the resistor changes, and the servo loop responds with negative feedback to a transistor. The voltage V_m is a measure of the current in the coils and sent to another board for display.

This current supply improves upon the slower current supply in two important ways. First, in addition to the sending V_m to the main board for display, each current supply's local ground is also sent to the main board. Since the high current carried by the ground changes the local ground of each supply, only the differential of V_m and the local ground correctly measures the current. Since the slower supplies did not have this capability when built, they had to be modified after assembly to correctly display the current in each coil.

Secondly, on the MOT supplies, there is no resistor in parallel with the coils like on the slower coil supplies. The parallel resistor on the slower coil was necessary to keep the servo loop stable, but may create thermal drifts if the resistor and coil have different temperature coefficients. In the

MOT supplies, the servo loop is stabilized by the capacitor and resistors in the feedback. The capacitor must somehow provide appropriately phased feedback to the loop. It does not seem to be operating by rolling back the gain of the loop at high frequencies since the oscillations occur at much lower frequencies than the RC time constant of the loop.

In the nulling coils, a standard high power MOSFET was used to adjust the current flowing through the coil. For the gradient coils, however, insulated gate bipolar transistors (IGBTs) were used. IGBT's have extremely low resistances when fully on, which was necessary for the high current gradient magnets. Also, IGBT's have large minimum reverse voltage breakdown limits. The 600 V breakdown limit for the IGBT that was used is necessary to rapidly shut off the gradient magnets.

A rapid shut-off for the gradient magnets will be important for future experiments where the MOT's quadrupole field is undesirable. A varistor (V271HA32) in parallel with the coil dissipates the energy when the gradient coils are shut off. A varistor is much like a Zener diode with a large breakdown voltage. Above a certain threshold current, normally in the milliamp range, the voltage across a varistor will be constant. Thus, instead of the coil's current decaying exponentially across a resistive load, the current decays linearly across a varistor. The circuitry for the gradient magnets can completely shut down the gradient coils from 24 A to 0 A in about 250 μs.

While the circuitry can control the current flowing in the gradient wires, eddy currents in the apparatus significantly effect how quickly the magnetic field vanishes. Eddy currents within the copper spool of the gradient coils lasted on the order of 20 ms, almost two orders of magnitude longer than the coil shut-off time. After putting a thin radial slit through the each coil spool, the eddy currents near the coils were significantly reduced as measured by the Bell gaussmeter. However, accurate measurement of the eddy currents is not trivial. Pickup coils which measure the eddy current through mutual inductance also change the dynamics of the eddy currents. Eddy currents within the stainless steel vacuum system may limit the speed at which the magnetic field at the atoms is reduced.

4.5.3 Optical Detection of the MOT

With approximately 10^8 atoms in the MOT, the fluorescence is easily seen by eye. To determine the approximate number of atoms in the MOT, the fluorescence of the MOT is measured with a calibrated photomultiplier tube (PMT). This PMT also measures the fluorescence of the atoms in the final state at each measurement frequency during the imaging experiment. Occasionally, a CCD camera is used to record fluorescence and absorptive images of the MOT.

A Hammamatsu 1894 PMT was optically coupled to the MOT through an optical fiber. The PMT and fiber were calibrated by measuring the power in a laser beam, attenuating the beam with calibrated neutral density filters, shining the beam into the end of the fiber, and measuring the current generated by the attenuated beam. Using this method, we found that the

PMT-fiber combination has a current gain of $\alpha = 69\,\mathrm{A/W}$ at 1000 V bias. At 800 V bias, the gain is $\alpha = 18.7\,\mathrm{A/W}$. The PMT has a maximum safe output current of 30 μA. The load on the PMT is 2 kΩ which gives it a frequency response near 2.5 MHz and a maximum output voltage of 60 mV.

The fluorescence collection optics consist of two 10 cm focal length 3 cm dia. lenses mounted approximately 15 cm from the MOT. The lenses are mounted back to back so that the image distance of the combined lens system was 7.5 cm. With the largest dimension of the MOT approximately 2 mm, the maximum image dimension is 1 mm. The optical fiber with a 6.3 mm aperture was placed at the image distance for the lens pair.

Because of the presence of the repumping light in the MOT beams, the atoms in the MOT were continually photon bursting. The voltage generated by the PMT across the resistive load R per photon bursting atom is given by

$$V_a = P_0 \sigma \alpha R \tag{4.26}$$

where $P_0 = 5.5 \times 10^{-9}\,\mathrm{mW}$ as determined in (3.11) and σ is the solid angle subtended by the detection system. The fluorescence collecting lenses used during the imaging experiment present a solid angle of $\sigma = 2.5 \times 10^{-3}\,\mathrm{str}$ to the MOT. With a bias of 800 V on the PMT, $V_a = 514\,\mathrm{pV}$. The MOT regularly captured 10^8 atoms as determined by this method.

A CCD camera is also used to record two-dimensional fluorescence and

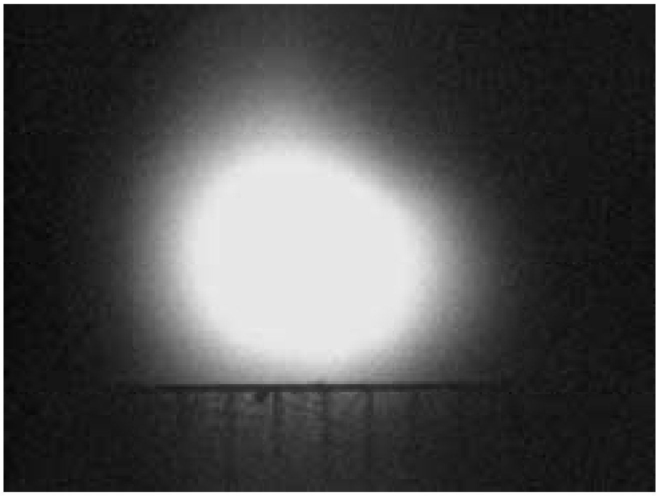

Figure 4.28: The fluorescence of the MOT captured by a CCD camera. Each ruler division corresponds to 1/3 mm.

absorptive pictures of the atoms in the MOT. However, by using these methods of observing the MOT, the entire depth of the MOT is averaged onto a single measurement plane. Figure 4.28 shows one of the fluorescence pictures. The MOT is magnified 3× in this picture. At the bottom of the frame is the shadow of a ruler which was in the image plane of the MOT. Consequently, one division on the ruler corresponds to 1/3 mm. The fluorescence picture shows that the MOT is shaped like an ellipsoid. The MOT is narrower along the dimension that corresponds to the axial magnetic field of the coils. The absorption picture, Figure 4.29, formed by sending a large 5 μW beam through the MOT, shows similar behavior.

The goal of the Raman induced resonance imaging experiment, discussed in the next chapter, is to image the MOT based on the natural symmetry of the trap. Rather than averaging the depth of the atoms onto a plane, the

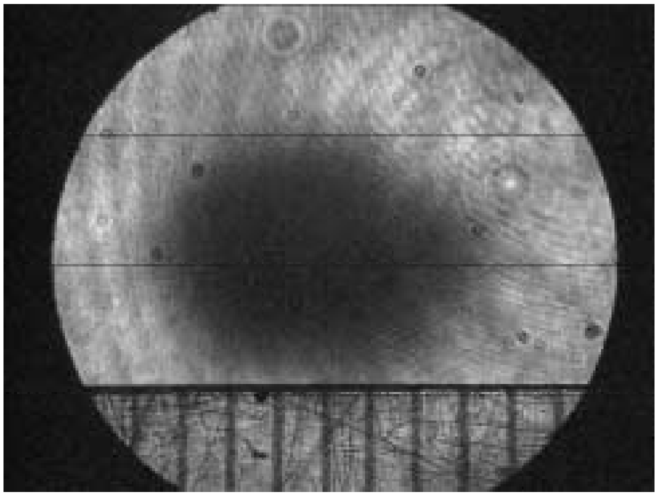

Figure 4.29: The absorption of the MOT captured by a CCD camera. Each ruler division corresponds to 1/3 mm.

magnetic resonance imaging probes the MOT in shells of constant magnetic field strength.

Chapter 5

The Imaging Experiment

In the imaging experiment, a series of pulses are used to measure a Raman spectrum which depends on the spatial distribution of atoms in the MOT. In this chapter, I will describe the method used to measure the spectra. The analysis of the spectra is presented in Chapter 6.

After the MOT has formed and the number of atoms has reached equilibrium, the four operations shown in Figure 5.1 are used to create each point in the spectrum. First, the laser beams that form the MOT are momentarily turned off. At this point, atoms populate both hyperfine levels of the ground state. As explained in Chapter 2 , these states are used as the initial state $|i\rangle$ and final state $|f\rangle$ of the Raman transition. To put all of the atoms into the initial state, an "optical pumping" beam is used. The optical pumping beam, which is resonant with the atoms in the $|F = 3/2\rangle$ state, continues placing those atoms into an excited state until they decay to the nonresonant $|F = 1/2\rangle$ ground state. With all of the atoms in the $|F = 1/2\rangle$ initial state, they are prepared for the Raman pulse.

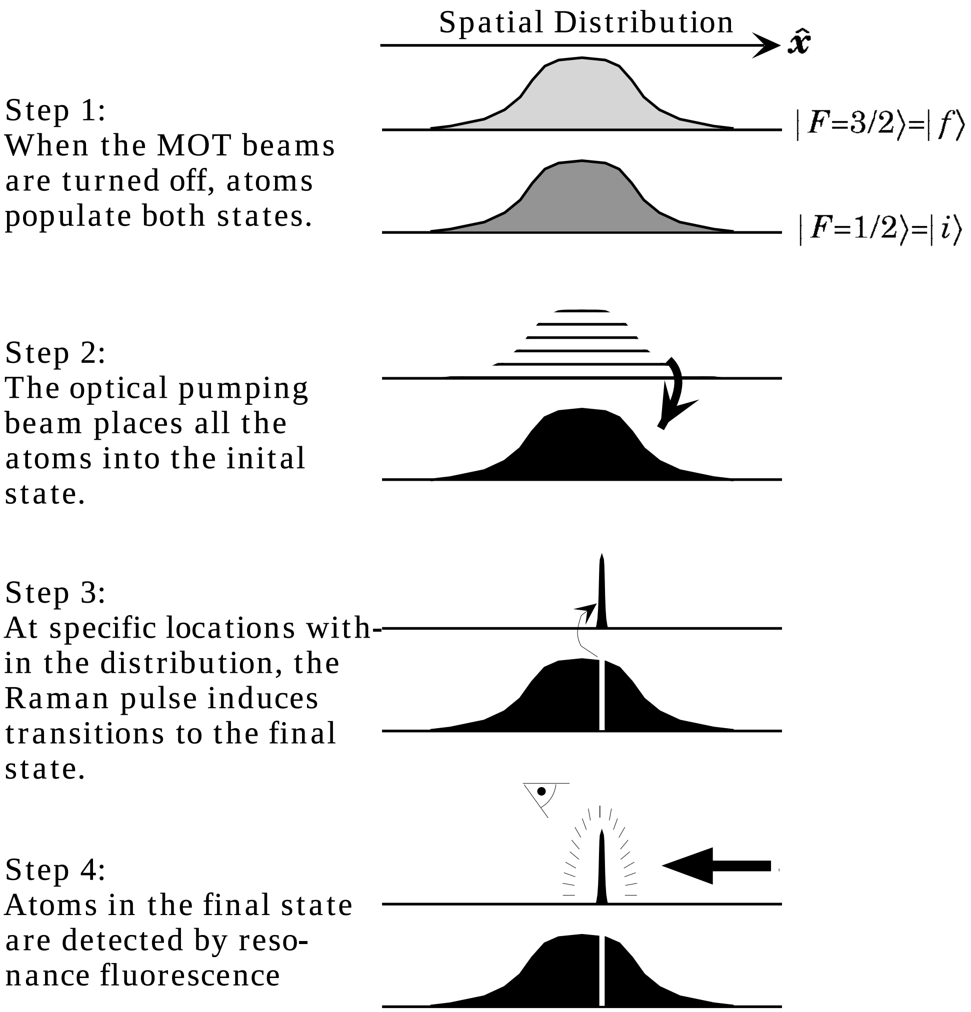

Figure 5.1: A schematic of the four steps used to generate a point in the Raman spectrum.

After the optical pumping beam is turned off, a Raman pulse with a well-defined Raman difference frequency induces transitions from the initial to the final state. Only the atoms located in a particular magnetic field and hence, a particular set of points in space, are coupled to the $|F = 3/2\rangle$ state (see Section 3.3.6).

When the Raman pulse ends, the resonant optical pumping beam is turned on again to probe atoms that made the transition to the final state. The probe beam causes the $|F = 3/2\rangle$ atoms to fluoresce. The magnitude of the fluorescence is proportional to the number of atoms in the final state. Lenses capture this fluorescence and focus it into an optical fiber which leads to a photomultiplier tube (PMT). The voltage generated by the PMT is recorded and the MOT beams are turned back on, reinstating the trapping potential. Additional points in the spectra are determined by taking measurements at a series of Raman difference frequencies.

5.1 Optical Layout

During the experiment, the laser frequency is referenced to the frequency of the $|F = 3/2\rangle$ D_2 resonance in ^{6}Li. Thus, the laser output frequency is at the cooling transition frequency, defined as ω_0 throughout this chapter. To perform this experiment, a number of different laser beams are required—many, but not all of them must be pulsed. The different beams are listed in Table 5.1 along with their frequencies and whether they are continuous (cw)

Beam	Frequency	CW/Pulsed
reference	ω_0	cw
slower	$\omega_0 - 200\,\mathrm{MHz}$	cw
trapping	$\omega_0 - n\gamma$	pulsed
trap repumper	$\omega_0 + 220\,\mathrm{MHz}$	pulsed
optical pump/probe	ω_0	pulsed
Raman	$\omega_0 + 110\,\mathrm{MHz}$, $\omega_0 - 118\,\mathrm{MHz} - \delta$	pulsed

Table 5.1: The laser beams required in the imaging experiment. $n\gamma$ means a few optical transition linewidths, δ is the Raman detuning from the magnetic independent Raman transition resonance frequency.

or pulsed. The beams are created using a combination of beamsplitters and acousto-optic modulators.

The reference beam is used to lock the laser to ω_0, the transition frequency of the $|F = 3/2\rangle$ resonance in the D_2 line. To lock the laser, the reference beam is sent into a separate vacuum system where it interacts with another lithium beam. The oven and vacuum system for this atomic beam are remnants from a previous experiment [59]. The laser is frequency modulated and a locking circuit monitors the derivative of the fluorescence signal of the $|F = 3/2\rangle$ resonance. This fluorescence is measured by an additional photomultiplier tube. A servo loop [57] sends an error voltage to the laser which minimizes the average derivative signal, keeping the laser locked to the the cooling transition.

The cw slower beam, described in Section 4.4.6, is created by shifting the original laser beam frequency by $-200\,\mathrm{MHz}$ with an acousto-optic modulator (AOM). In general, to couple a laser beam into an acousto-optic modulator, a 25 or 30 cm focal length lens focuses the input beam into the acousto-optic crystal. Inside the crystal, the light scatters off of a sound wave created by the rf energy supplied to the crystal by the AOM power supply. The light may scatter into different orders producing more than one output beam. Typically, only the first order beam is used which is either upshifted or downshifted by the rf frequency of the modulator. After the modulator, the light is recollimated using a lens with the same focal length as the input lens. Once the slower laser beam has the correct frequency, it is σ^+ polarized by a Glan-Thompson prism and a Babinet-Soleil compensator.

To create a MOT, three sets of counterpropagating laser beams must be created as discussed in Section 4.5. Each set of beams must be appropriately circularly polarized, as shown in Figure 4.22, and contain both the trapping and repumping frequencies shown in Table 5.1.

The different frequencies are created using acousto-optic modulators as shown in Figure 5.2. A beam from the laser is passed two times through an acousto-optic modulator. This shifts the frequency of the beam 220 MHz to the blue to provide the repumper frequency. Then, a part of this upshifted beam is passed twice through a tunable modulator and shifted down by a few linewidths more than 220 MHz. This provides the tunable trapping frequency in the MOT beams. The frequency of the tunable AOM is adjusted by a voltage supplied to the AOM from a potentiometer that divides the voltage across two 9 V batteries. The repumper and trapping frequencies are combined at the output of the second polarizing beamsplitter. By rotating the half wave plate, different ratios of trapping and repumping power may

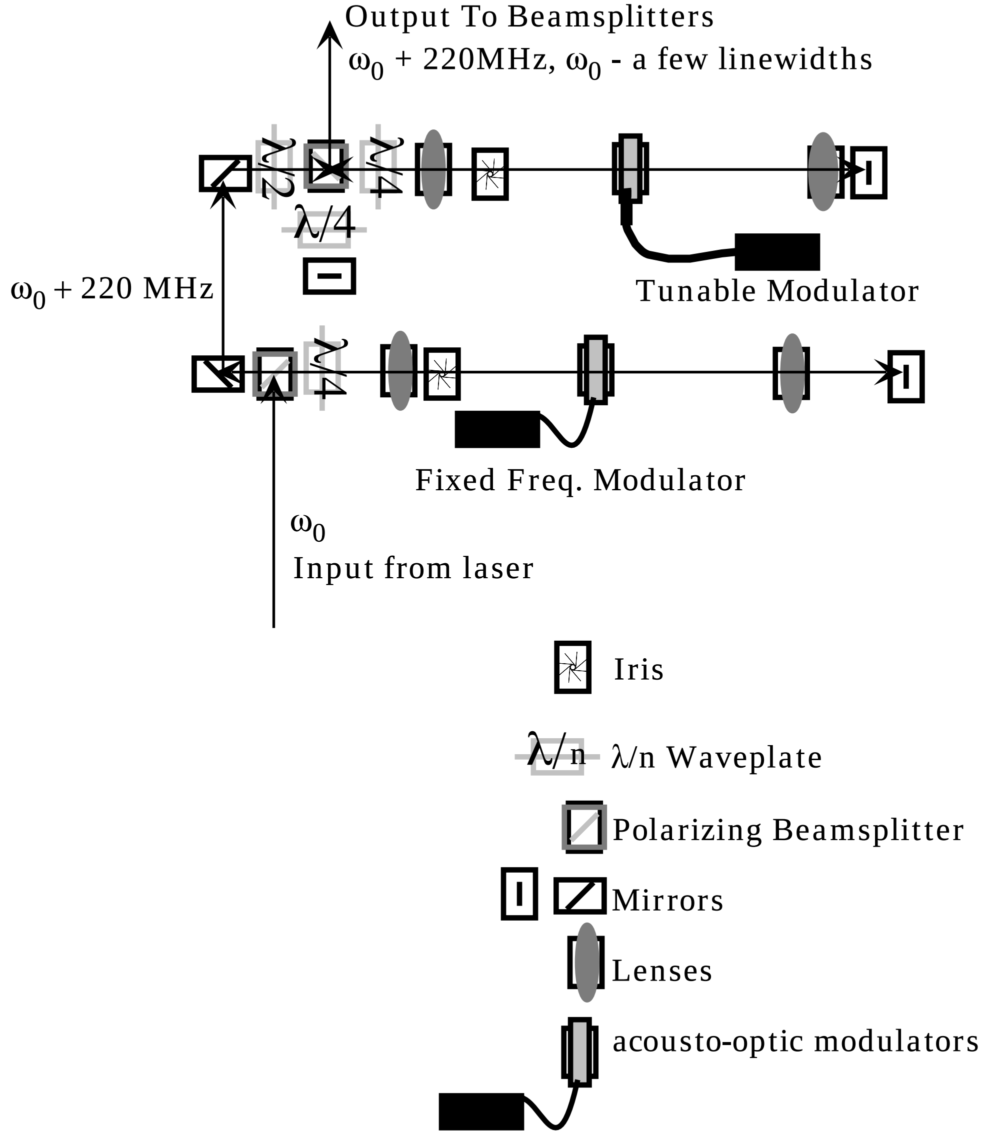

Figure 5.2: The layout of the modulators for creating the MOT beams.

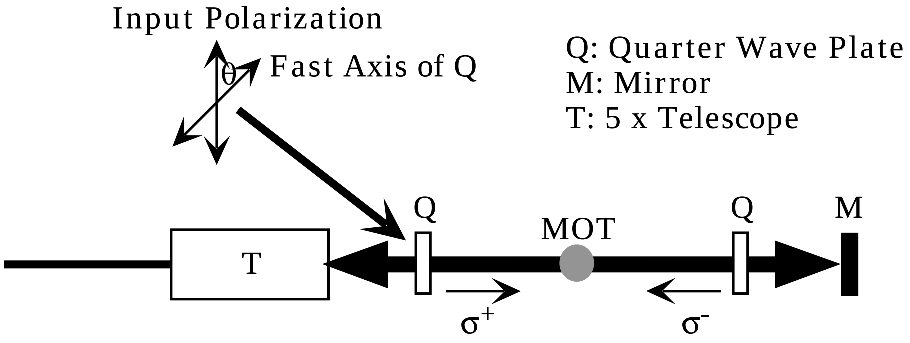

Figure 5.3: Schematic of the MOT beam optical elements.

be selected.

Once the trapping and repumping frequencies are combined into a single laser beam, the beam is sent to a polarizing beamsplitter which splits the beam into two. If the polarization of the beam entering this beamsplitter is rotated using a half-wave plate, the ratio of the power of the two output beams is adjusted. A half-wave plate before the beamsplitter rotates the polarization to create an output power ratio of 1:2. The more powerful beam is split again using a standard beamsplitter. Thus, the three resulting beams have roughly equal power and are used as the MOT beams.

Each of the MOT beams is then treated as shown in Figure 5.3. The $5\times$ telescope expands the input beam to approximately 1 cm in diameter in order to increase the capture volume of the MOT [13]. For a vertical input polarization, to create σ^+ polarization, the fast axis of the first quarter wave plate Q must be oriented at $\theta = 45^\circ$ with respect to the input polarization. An incorrect circular polarization will prevent the MOT from operating. The orientation of the second quarter wave plate is arbitrary since two passes

Beam	Vertical	Horizontal 1	Horizontal 2
Trapping Beam Power (mW)	5.7	6.0	7.0
Repumper Beam Power (mW)	1.6	0.73	0.95

Table 5.2: Typical MOT beam powers.

through it create a half wave of retardation which flips the polarization to σ^-. The mirror M is aligned to retro-reflect the input beam, creating a counter-propagating pair of beams. The combination of the two quarter wave plates creates opposite circular polarizations in the counterpropagating beams, as required. Each of the three input MOT beams is treated similarly. However, since the gradient along the axis of the magnets is opposite in sign to the radial gradient in order so satisfy $\nabla \cdot \boldsymbol{B} = 0$, the orientation of the first quarter wave plate for the beam along the axis of the magnets is rotated 90° with respect to the orientation of the first quarter wave in the beams that are off-axis. An example of typical repumping and trapping beam powers in each of the MOT beams is shown in Table 5.2. The MOT beam diameters were approximately 1 cm.

The Raman resonance imaging experiment requires the Raman beam and the pump/probe beam. These additions with respect to the MOT apparatus are shown in Figure 5.4. The coordinate system for the experiment is also shown in the figure. The $\hat{\boldsymbol{z}}$ axis is defined by the propagation direction of the Raman beams, the $\hat{\boldsymbol{x}}$ axis is the axis of the MOT gradient coils, and the $\hat{\boldsymbol{y}}$ axis is along the atomic beam.

The Raman beam contains an $\hat{\boldsymbol{x}}$ polarized field and a $\hat{\boldsymbol{y}}$ polarized field. To

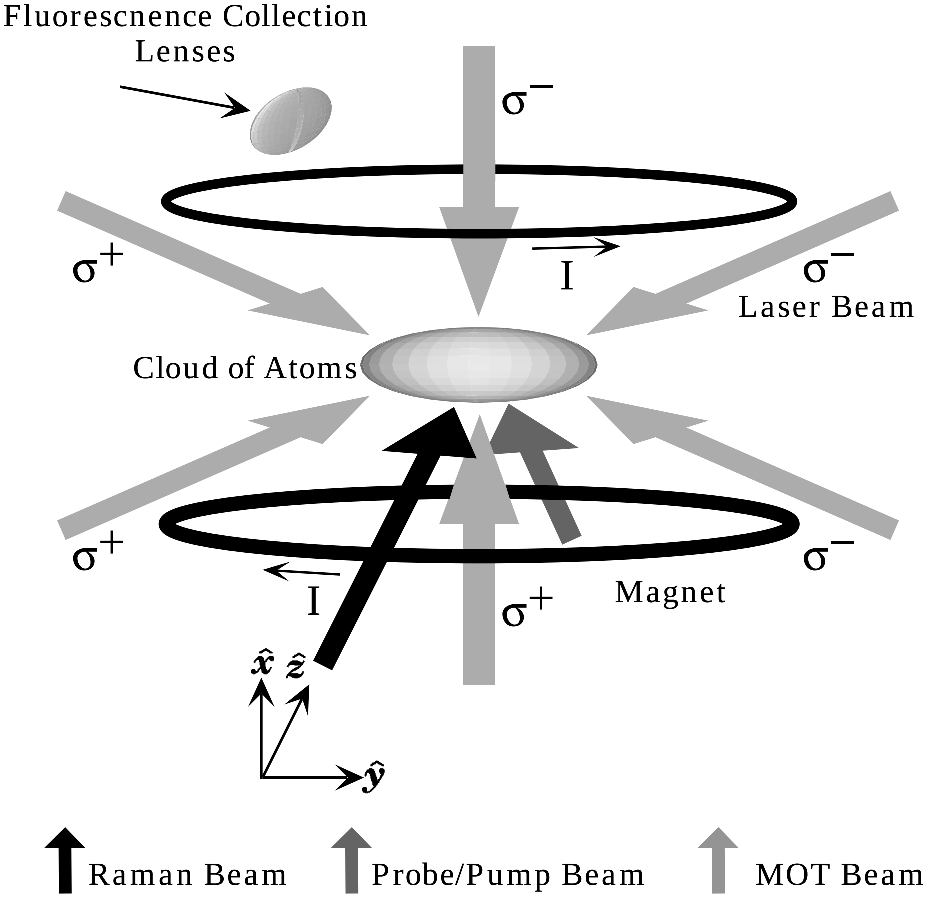

Figure 5.4: The Raman imaging experiment showing MOT beams and the additional Raman and pump/probe beams.

create the different polarizations, a beam from the laser is passed through a half wave plate and polarizing beamsplitter, creating $\hat{\boldsymbol{x}}$ and $\hat{\boldsymbol{y}}$ polarized beams. The half wave plate rotates the polarization of the input beam and allows one to vary the ratio of powers between the $\hat{\boldsymbol{x}}$ and $\hat{\boldsymbol{y}}$ components.

The $\hat{\boldsymbol{y}}$ polarized beam is sent through a fixed 110 MHz acousto-optic modulator and the $\hat{\boldsymbol{x}}$ polarized beam is sent through a tunable modulator. The difference frequency of the two beams is adjustable by changing the output frequency of the tunable modulator. A battery pack and the output from a computer's digital to analog conversion board are added and supplied to the tunable AOM, setting its frequency. The difference frequency of the two beams is given by $228\,\mathrm{MHz} + \delta$ where delta is defined as the Raman detuning from resonance with the magnetic independent transition.

After the frequencies of the beams are shifted, they each go through their own variable density filter so that the power in each beam may be adjusted independently. Then, the beams are recombined by a polarizing beamsplitter and focused into a single-mode polarization preserving optical fiber.

At the output of the fiber, the Raman beams have identical spatial modes and are perfectly overlapped. The spatial matching of both polarizations of the Raman beam maintains a constant intensity ratio in the beam which is necessary for cancelling the light shifts discussed in Section 2.1.2. In order to sample the atoms in the MOT independently of their position within the Raman beam, the diameter of the Raman beams should be much larger than the size of the MOT. To accomplish this, a telescope expands the Raman beam after it emerges from the fiber. The determination of the Raman pulse area is treated in Section 5.3.

The pumper/probe beam is used to place the atoms into the $F = 1/2$ initial state before the measurement and to probe the $F = 3/2$ final state after the measurement. It pumps the atoms into the $F = 1/2$ state by continually driving the $F = 3/2$ atoms into the excited state until the atoms decay into the $F = 1/2$ state. This linearly polarized beam has a frequency of ω_0 so that it is resonant with the $F = 3/2$ state. To create this beam, a fraction of the slower beam, which is at a frequency of $\omega_0 - 200\,\mathrm{MHz}$, is upshifted by 200 MHz bringing it back into resonance. This convoluted method for recreating the frequency of the laser is necessary to make the pump/probe beam pulsable.

The probe beam's intensity was approximately five times the saturation intensity of the transition as defined by (4.11). This ensures that the Zeeman shifts of the probed state are negligible so that *final state* atoms are measured equally wherever they are in the MOT's magnetic field. The power in this beam is approximately 6 mW and has a full-width half-maximum (FWHM) diameter of 7 mm which is much larger than the MOT. By using a large beam, the probe intensity is approximately uniform over the volume of the MOT.

The actual optical layout of the experiment is shown in Figure 5.5. The optics are split over two tables due to the number of AOM's that are required for the experiment. The laser beams and their respective AOM's are

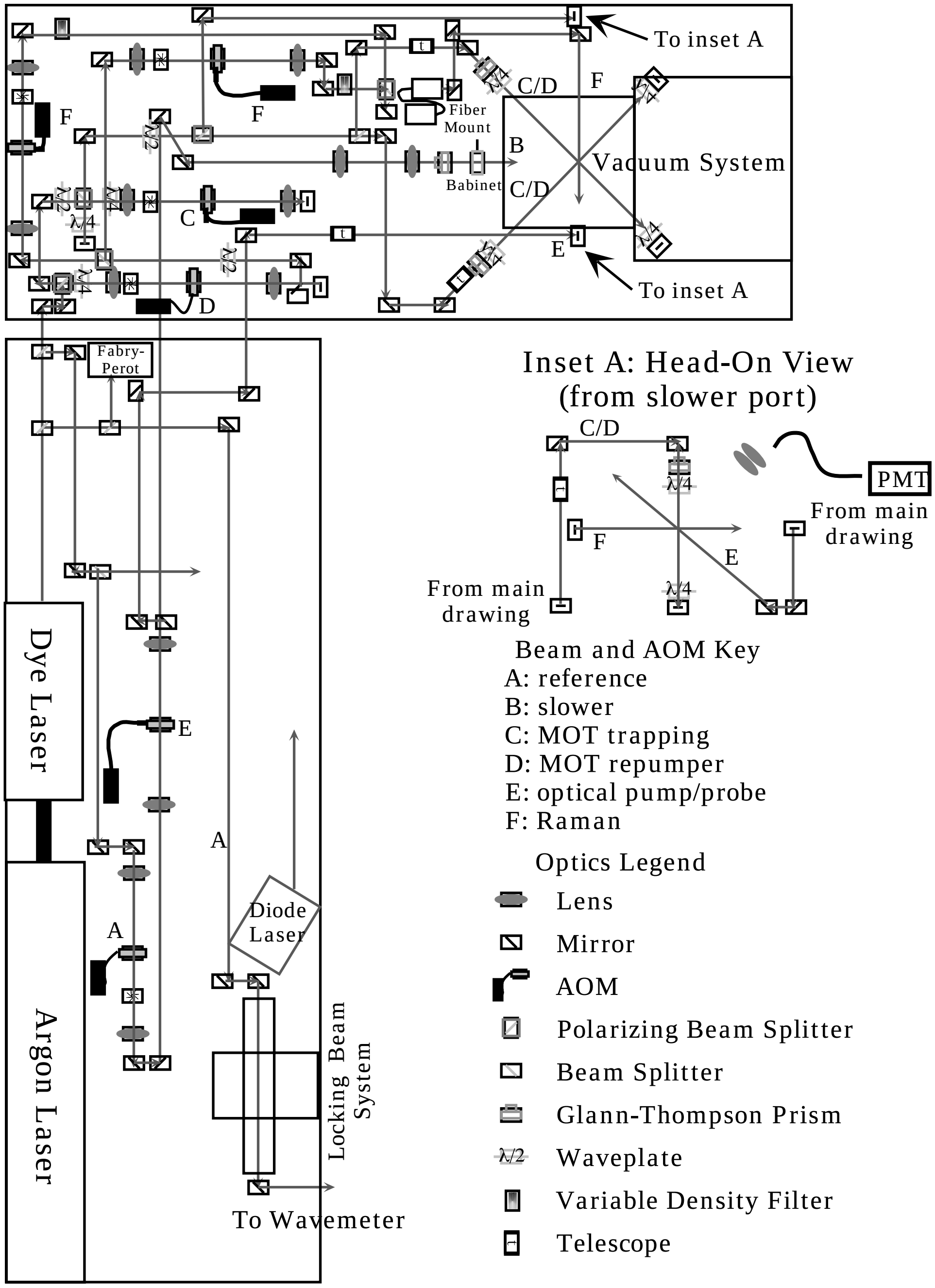

Figure 5.5: The optical layout for the imaging experiment.

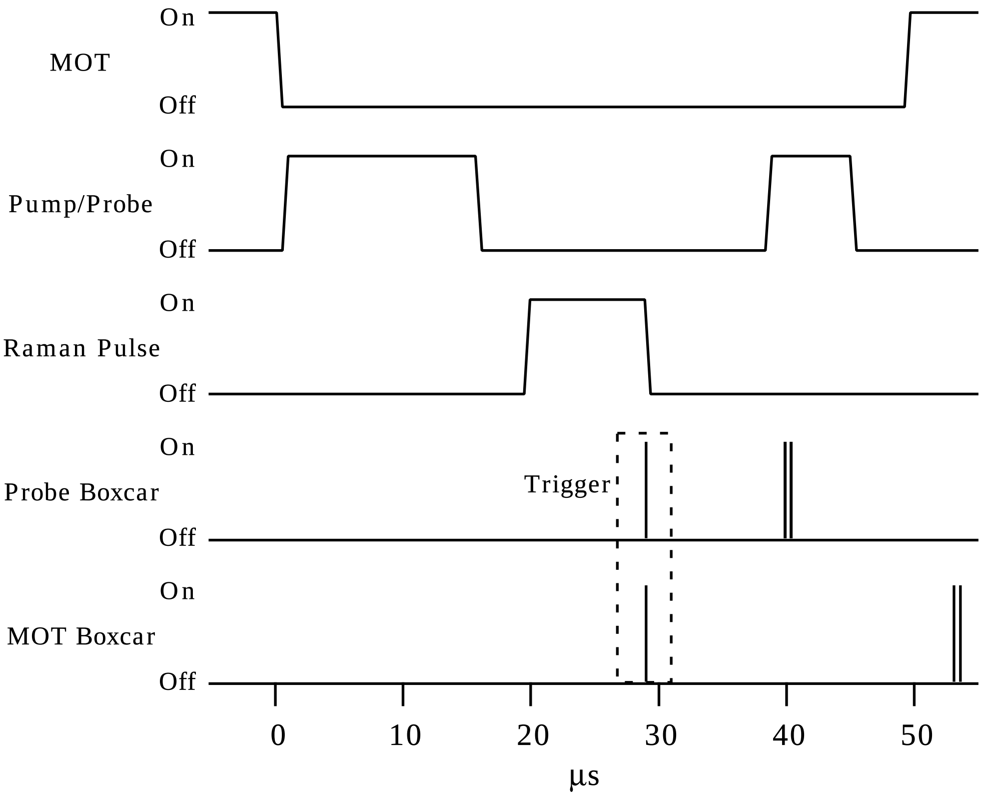

Figure 5.6: The timing of the pulses during the imaging experiment.

referenced by letter, and a legend explains the optical symbols.

5.2 Pulse Timing and Data Acquisition

The pulse timing is handled by two pulse generators from Stanford Research Systems. The clock reference of one of the generators is used to drive the other generator in order to keep them synchronized. The timing of the pulsed laser beams is displayed in Figure 5.6.

At $t = 0$, the MOT beams go off. Then, after a $4\,\mu$s delay, the optical pumping pump/probe beam turns on for approximtely 15 μs. Even though optical pumping should take on the order of a few excited state lifetimes which is 27 ns, longer optical pumping times are required in the MOT. The longer pumping times are due to the high density of atoms. With approximately 10^8 atoms in the MOT, the density approaches 10^{11} atoms/cc. At this density, the MOT significantly attenuates the beam.

To see this, consider that the intensity as a function of depth x into the atoms is approximated by

$$\begin{aligned} I(x) &= I_0 e^{-\alpha x} \qquad (5.1) \\ \alpha &= n\sigma \end{aligned}$$

where α is the absorption coefficient, n is the density of the atoms, σ is the absorption cross section, and I_0 is the input intensity. For atoms, the absorption cross section is a function of intensity (which we assume to be independent of x for the cross section calculation) and is given by the photon scattering rate, Γ_{sc} (4.8), divided by the number of photons entering the medium per unit area, $I_0/(\hbar\omega)$, where ω is the photon frequency. If $I_0 \gg I_{sat}$ where I_{sat} (4.11) is the saturation intensity, the absorption cross section is

$$\sigma = \frac{\Gamma\hbar\omega}{2I_0} \qquad (5.2)$$

where Γ is the excited state decay rate. For lithium, $\Gamma = 37\times10^6\,\mathrm{s}^{-1}$ and

$\omega = 2\pi c/671\,\mathrm{nm}$. For the pumping beam, $I_0 = 12.5\,\mathrm{mW/cm^2}$. Thus, the absorption coefficient for the pumping beam is $\alpha = n\sigma = 44\,\mathrm{cm^{-1}}$. Therefore, even though the MOT is only 1 mm thick, the beam is severely attenuated. Consequently, optical pumping takes significantly longer than a few exited state lifetimes. If the beam is made more intense, off resonant exitation of the $F = 1/2$ state prevents the $F = 3/2$ state from being emptied.

Optical pumping also takes longer due to an effect called radiation trapping. Because the density of atoms is so high, the photons which are emitted by one atom are frequently absorbed by another atom. Whenever a photon is reabsorbed by another atom, the population of the excited state does not decrease. Consequently the excited state decay rate of the *sample's* population is significantly decreased.

The Raman pulse begins $4\,\mu$s after the optical pumping beam is turned off. Since the Raman pulse is composed of two frequencies, two AOMs must be turned on simultaneouly. Even though the two AOMs receive the same electronic pulse, differences in optical alignment vary their actual turn-on times. This occurs because the rf pulse generates a sound wave which must propagate through the AOM crystal in order to turn on a beam. If the input laser beams are located at different distances from their crystal's rf transducer, they will turn on at different times. To synchronize the pulses, one of the Raman AOMs is slid perpendicular to the laser beam while observing the pulses in the Raman beam with an optical diode. By sliding the crystal, the transducer's position relative to the laser beam is varied and the two separate pulses may be sychronized.

After an 8.8 μs Raman pulse, the optical pumping beam is turned back on to probe the final state. The fluoresence from the final state atoms is detected by the fiber and PMT apparatus described in Section 4.5.3. The voltage across the PMT's 2 kΩ load is measured by a Stanford Research Systems boxcar averager. The probe boxcar timing graph in Figure 5.6 refers to this boxcar which is triggered at the end of the Raman pulse. The boxcar's gate delay and width are adjusted to measure only the peak of the final state fluorescence. This fluorescence is assumed to be directly proportional to the number of final state atoms.

Another boxcar is used to measure the MOT fluorescence. The MOT fluorescence is monitored in order to make sure that the number of trapped atoms remains constant during the imaging. This is necessary because occasional bubbles in the dye laser cause sudden frequency jumps of the laser which destroy the MOT.

Figure 5.7 shows the time dependent fluoresence caused by the series of imaging pulses as measured by an oscilloscope in parallel with the boxcar input. Although the fluorescence shown here was measured with different timings than that described by Figure 5.6, it shows the typical behavior. When the MOT beams go off, the fluorescence drops quickly, indicating the fast response of the PMT with the 2 kΩ load.

After the optical pumping beam is turned on, the atoms decay to the $F = 1/2$ state with a time constant of 1.67 μs. As mentioned earlier, this

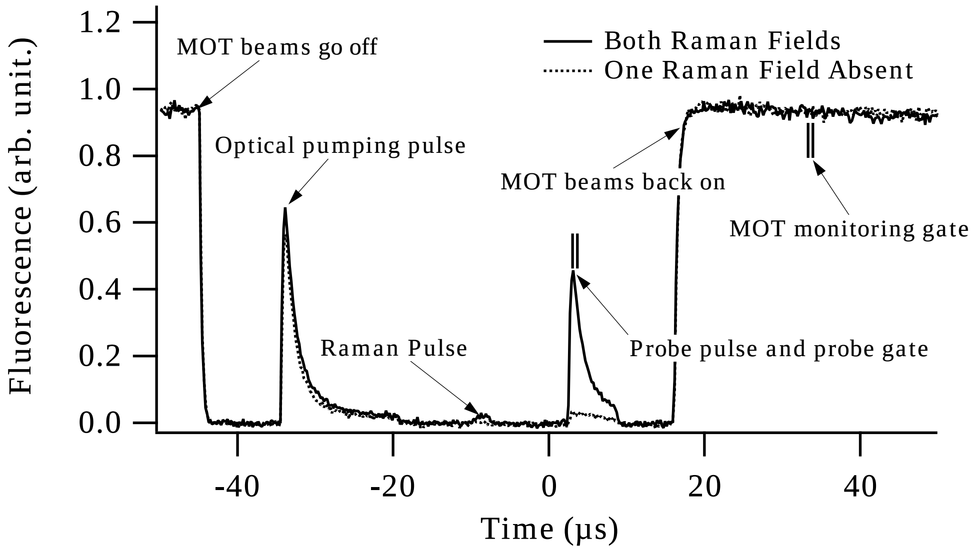

Figure 5.7: The experimentally measured time dependence of the fluorescence caused by a single series of imaging pulses.

is much longer than the typical optical pumping time. During the imaging experiment, even longer optical pumping times were observed.

The Raman pulse causes a small amount of fluorescence as shown in the figure. This fluoresence is due to off-resonant transitions from the initial state to the intermediate states of the Raman transition. Since the intermediate states are excited states, the atoms fluoresce when they decay from these levels. The off-resonant transitions originate from the intermediate state lifetime in (2.11) and will become an important part of the data analysis in Chapter 6.

After the Raman pulse, atoms that are located in the appropriate magnetic field will be in the final state. The next peak in the solid oscilloscope trace is due to the fluorescence from these final state atoms during the probe pulse. The solid curve shows the final state fluorescence when both Raman fields are present in the Raman beam. The dotted curve shows the absence of fluorescence when one of the Raman beams is blocked. In this case, the initial and final states are no longer coupled and none of the atoms make a Raman transition. The position and width of the probe boxcar gate only measures the PMT voltage during the peak of the final state fluorescence.

After the probe pulse, the MOT beams come back on and the MOT fluoresence returns. The approximate timing of the MOT fluorescence boxcar gate is also indicated in Figure 5.7. During the 50 μs duration of the pulse sequence, atoms are not lost from the MOT as indicated by the identical MOT fluorescence levels before and after the single pulse sequence.

These pulse sequences are repeated at a 1 kHz repetition rate. The 50 μs period of the sequence at this repetition rate maintains the duty cycle of the MOT potential at 95%. The final state and MOT fluoresence measurements from the four step imaging sequence are each amplified and averaged over three cycles by the boxcars. After at least three sequences, the same computer that controls the tunable AOM in the Raman beam is used to read and record the averaged output from the boxcars.

I have just described a four step sequence of pulses that is repeated three times at a given Raman difference frequency to generate a single point of the Raman spectrum. To generate a series of points, this process must be done with a series of Raman difference frequencies. Figure 5.8 shows the flowchart for measuring an entire Raman spectrum.

First, the computer is instructed to measure the Raman spectrum. The computer then sets the frequency on the tunable Raman AOM to generate the lowest Raman difference frequency in the spectrum. After waiting for at least three of the pulse sequences, the computer reads the two voltages on the boxcars corresponding to the final state and MOT fluorescence intensities.

After all but the first point in the spectrum, the computer compares the MOT fluorescence with all previous measurements of the MOT fluorescence in the current spectrum. If the MOT fluorescence remains consistent throughout, the computer measures the entire spectrum. If the MOT fluorescence changes significantly due to a bubble in the dye laser, as discussed above, the computer discards the spectrum, waits 30 s to allow the atomic distribution to restore, and then attempts to measure the spectrum again.

5.3 Experimental Procedures

The procedures required to prepare the experiment before the imaging process can begin are described in this section. After the oven and vacuum pumps are turned on as described in Section 4.2.2, the dye laser is locked to the $|F = 3/2\rangle$ resonance of the ^{6}Li D$_2$ line which is diagrammed Figure 3.2. The frequency of the laser is brought to within 30 GHz of the required frequency using a wavemeter [85] which compares a helium neon laser's wavelength to the dye laser's wavelength. The wavemeter displays the ratio r

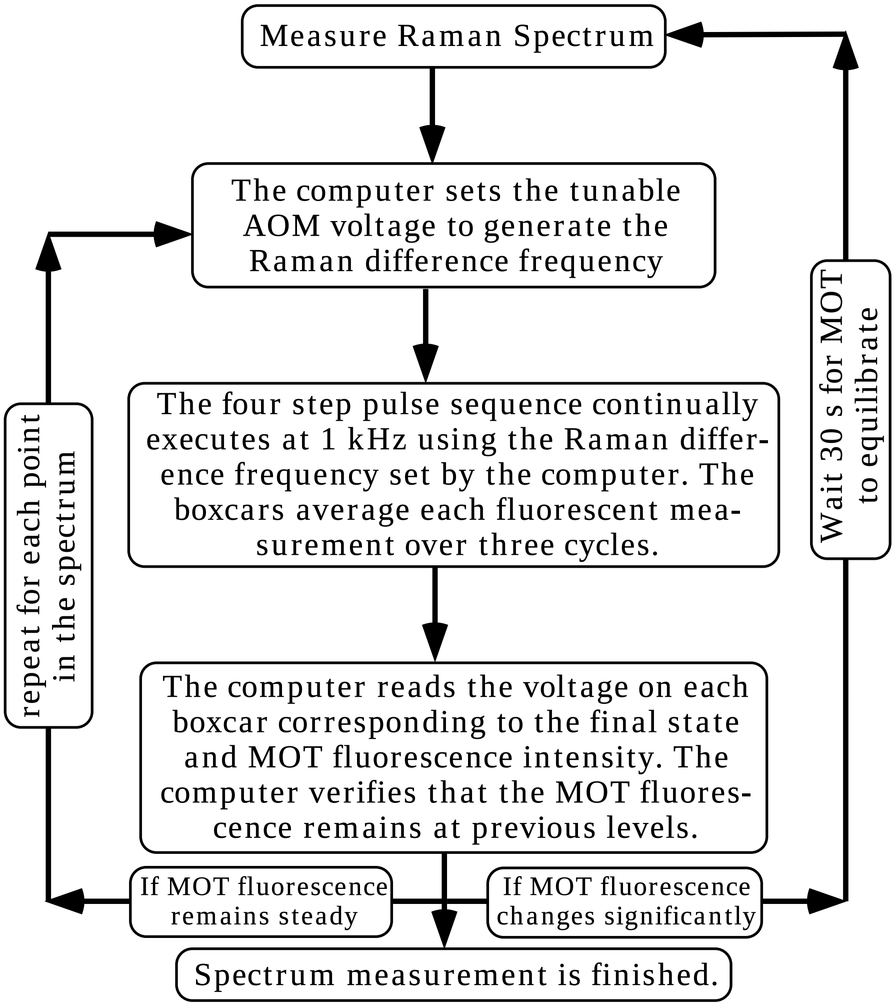

Figure 5.8: The steps followed in measuring a Raman spectrum.

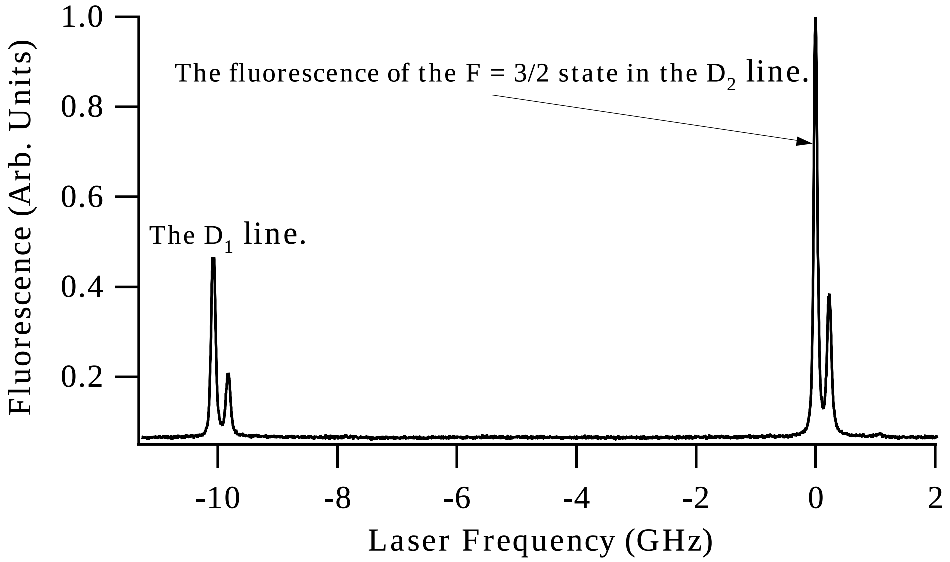

Figure 5.9: The experimentally measured fluorescence spectrum of ^{6}Li.

given by

$$r = \frac{\lambda_{HeNe}}{\lambda_{dye}} \tag{5.3}$$

where λ_{laser} is the wavelength in in air. For the D_2 line, $r = 0.943386$ and for the D_1 line, $r = 0.94336$.

Once the laser is tuned to the D_2 line as measured by the wavemeter, the lithium oven in the locking vacuum system is turned on and warms up quickly. The laser is set up to scan its frequency 30 GHz while the fluorescence of the atoms in the locking atomic beam is measured.

Figure 5.9 shows an example of the fluorescence spectrum of ^{6}Li measured by scanning the laser over approximately 13 GHz. This measurement was intentionally offset from the D_2 line so that both lines could be seen. The two peaks in each line correspond the 228 MHz hyperfine structere splitting of the ground state. The tallest peak in Figure 5.9 corresponds to the $F = 3/2$ resonance in the D_2 line and is the one used to lock the laser.

After the laser is locked to the line, the alignment of the acousto-optic modulators is tweaked. While the AOMs' first order scattered power can be peaked by adjusting the mirrors prior to the AOM, this causes misalignment further down the laser beam's path. Instead, the AOM crystals are slightly rotated until the best power output into the first order scatter is obtained. By only rotating the crystal, gross misalignemt of the output beam is avoided. Because the timing of the individual optical frequencies in the Raman beams depends on the Raman AOMs alignment as mentioned earlier, the synchronization of their timing must be verified after this procedure.

After these preliminary alignment procedures are completed, the MOT and slower magnet supplies are turned on. Usually, a cloud of trapped atoms appears without significant adjustment to any of the laser beams. At this stage of the experiment, the MOT beams are running cw and the other pulsable beams are off. To maximize the number of trapped atoms, the slower laser beam is adjusted first. By looking through the top port of the oven pumping chamber (see Figure 4.3), the scatter from the slower laser beam on the oven nozzle is minimized. This points the slower beam directly into the nozzle. Then, the current in the final coil of the slower magnet is adjusted to select the final slowed velocity that maximizes the steady state number of atoms in the trap, as discussed in Section 4.4.5. The number of trapped atoms is observed by watching the MOT fluorescence measured by the PMT on an oscilloscope.

Once the slower laser beam and final magnet are adjusted, the MOT trapping beams and MOT magnets are optimized. Since the MOT forms under a wide range of conditions, the optimization of the MOT is determined by watching the cloud dissipate when the gradient magnets are switched off. For a detailed description of the MOT magnets, see Section 4.5.2. The MOT performs the best when the atomic cloud dissipates isotropically from the original position of the trapped atoms. If the cloud moves abrubply or if the cloud expands asymmetrically, further alignment is necessary.

Adjustment of the MOT beams and magnets occurs in two alternating steps. First, the "bing" method is used to isolate where the MOT is forming within the cross section of one trapping beam. A card with a small hole is slowly moved across the beam. Another observer looks for the MOT to form and says, "Bing!" with a volume appropriate to the magnitude of the MOT fluorescence as observed by eye. The loudest bing occurs when the aperture in the card is located in the beam where the center of the MOT forms. By noting the position of the aperture within the beam cross section, the beam can be centered on the MOT.

After performing this procedure on one MOT beam, the magnets are switched off and the MOT dissipation is observed. If the MOT seems to abruptly move in one direction, the other MOT magnets are used to move atomic cloud until the atoms expand from their trapped location. This is repeated for each beam in turn until the MOT expands appropriately.

Next, the Raman beam is aligned so that it hits the trapped atoms. This must be done with the MOT and Raman beams pulsing since, as shown in Figure 5.5, the two beams are not designed to operate simultaneously. The Raman beam is derived from the unshifted beam that emerges from the MOT repumping beam AOM. When the MOT repumping AOM is off, all of the power in the input beam passes through unshifted. This beam is then used to generate the Raman beam. Since the MOT beams and the Raman beam are never on simultaneously during the experiment, this provided an excellent method for multiplexing a significant fraction of the laser power into the different beams.

With both beams pulsing, the Raman beam is adjusted until it perturbs the atomic distribution. If no effect is observed by eye, the duty cycle of the beams is adjusted to favor the Raman beam until it exerts a noticeable influence on the trapped atoms.

Once the Raman beam is approximately positioned, the Raman beam is turned on cw, and the power transmission of each frequency component through the fiber is maximized. The maximization is performed with the voltage on the tunable Raman AOM set to 11.75 V, the voltage which corresponds to the magnetic field independent Raman transition frequency and the center of each Raman spectrum.

After the power transmission of each beam is optimized, the power in each beam is adjusted by moving the variable density filters shown in Figure 5.5 using translation stages. The appropriate power in the $\hat{\boldsymbol{y}}$-polarized beam is determined by the desired Raman pulse area, described in Section 2.1.3. For a particular transition, the pulse area is given by

$$\phi_{k,j} = \beta_{k,j}\tau \tag{5.4}$$

where j denotes the m_F of the inital state, k denotes the m_F of the final state, $\beta_{k,j}$ is the Raman Rabi frequency, and τ is the length of the pulse.

Since the expression for the Raman transition probability (2.36) does not correctly describe atoms located in small magnetic fields, as indicated in Chapter 2, the Raman pulse area is set to 2π for those atoms in the experiment. With this pulse area, the atoms that are untreated by the theory never make the transition to the excited state and are not observed in the spectrum. In small magnetic fields, the pulse area is most easily calculated by assuming $\{\hat{\boldsymbol{x}}, \hat{\boldsymbol{y}}\}$ polarizations for the Raman beam which induces only $\Delta m = 0$ transitions. The $\Delta m = \pm 2$ are not allowed because the Raman transition operator is rank one, as discussed in Section 2.2. In Table 3.1, the Raman Rabi frequency for these transitions is given as

$$\beta_{\frac{1}{2},\frac{1}{2}} = \beta_{-\frac{1}{2},-\frac{1}{2}} = \frac{2\sqrt{2}}{9}\beta_0 \tag{5.5}$$

where β_0 is defined in (3.18). Using (5.4) and (5.5), the desired intensity in the $\hat{\boldsymbol{y}}$-polarized beam is

$$I_y\,(\mathrm{mW/mm^2}) = \frac{9}{2\sqrt{2}\,\tau\,(5\,\mathrm{MHz})}. \tag{5.6}$$

With the Raman pulse duration $\tau = 8.8\,\mu\mathrm{s}$, the intensity of the $\hat{\boldsymbol{y}}$- polarized beam is set to $0.072\,\mathrm{mW/mm^2}$. The power corresponding to this intensity is determined by the size of the Raman beam.

The size of the Raman beam is measured by a Hammamatsu linear diode array. Mirrors are placed in the beam so that beam is measured at the same propagation distance as the MOT. The FWHM size of the Raman beam is $h = 4.8\,\mathrm{mm}$ horizontally and $v = 3.6\,\mathrm{mm}$ vertically, making it much larger than the MOT. The $\hat{\boldsymbol{y}}$-polarized power required in the Gaussian Raman beam is given by

$$P_y = \frac{\pi h v I_y}{4\ln 2} = 1.4\,\mathrm{mW}. \tag{5.7}$$

The power in the $\hat{\boldsymbol{x}}$-polarized beam is determined by the ratio expressed in (3.17) so that the light shifts balance in the Raman transition. Thus, $P_x = 3.1P_y = 4.3\,\mathrm{mW}$.

With the powers set appropriately in the Raman beams, the four step pulse sequence described earlier in this chapter is set up to repeat at 1 kHz. While pulsing, the optical pumping beam is aligned by moving it to the position which peaks the fluorescence caused by it as shown in Figure 5.7. Then, with the Raman difference frequency set to induce the magnetic independent transition, the Raman beam is slightly tweaked to maximize the fluorescence caused by the second optical pumping/probe pulse. This guarantees that the optical pumping/probe and Raman beams are centered on the MOT. After this final alignment procedure, the experiment is ready to measure the Raman spectrum and image the atoms.

Chapter 6

Results

In this chapter, the Raman spectra measured using the methods detailed in Chapter 5 are presented and analyzed. Using the expression for the Raman spectrum in Chapter 2 (2.36), which describes the ^{6}Li Raman transitions in an arbitrary magnetic field, a theoretical spectrum for imaging in the specific quadrupole field of the MOT is derived. This theoretical spectrum includes parameters that depend on the position and size of the MOT within the quadrupole field. By fitting the theoretical expression to the actual data, the real size and position of the MOT are determined.

As derived in Chapter 2, the general expression for the spectrum is expressed as

$$P_f^{tot}(\delta) = \int d^3\boldsymbol{r}\, n(\boldsymbol{r}) P_f^{sa}(\boldsymbol{r}, \delta) \tag{6.1}$$

where

$$\begin{aligned} P_f^{sa}(\boldsymbol{r},\delta) &= \sin^2(\frac{\sqrt{2}}{9}\frac{\beta_0\tau}{2}\sin\theta(\boldsymbol{r}))\,\mathrm{sinc}^2(\delta\tau/2) \\ &+ \frac{1}{2}\sin^2(\frac{\sqrt{6}}{9}\frac{\beta_0\tau}{2}\sin\theta(\boldsymbol{r}))\left\{\mathrm{sinc}^2\left[\frac{(\delta-\frac{4\mu_B}{3\hbar}B(\boldsymbol{r}))\tau}{2}\right]\right. \\ &\left.+\ \mathrm{sinc}^2\left[\frac{(\delta+\frac{4\mu_B}{3\hbar}B(\boldsymbol{r}))\tau}{2}\right]\right\} \\ &+ \frac{1}{2}\sin^2(\frac{2\sqrt{2}}{9}\frac{\beta_0\tau}{2}\cos\theta(\boldsymbol{r}))\left\{\mathrm{sinc}^2\left[\frac{(\delta-\frac{2\mu_B}{3\hbar}B(\boldsymbol{r}))\tau}{2}\right]\right. \\ &\left.+\ \mathrm{sinc}^2\left[\frac{(\delta+\frac{2\mu_B}{3\hbar}B(\boldsymbol{r}))\tau}{2}\right]\right\}. \end{aligned} \tag{6.2}$$

Each of the terms in the resolution function (6.2) peaks where the argument of the sinc squared function is zero. Also, note that the resolution function is symmetric about $\delta = 0$. The quantity δ is the Raman detuning from resonance with the magnetic independent transition (Section 3.3.6). With five terms in the resolution function, one would expect five peaks in the Raman spectrum.

The example of a Raman spectrum, shown in Figure 6.1, clearly demonstrates this symmetric five-peak behavior. The horizontal axis of the spectrum is the Raman detuning and the vertical axis is the fluorescence of the final state. The data in this graph is averaged over fifty spectra taken under identical conditions. After averaging, the peak height is normalized to one.

The large narrow peak at $\delta = 0$ is the magnetic field independent transition resonance which is described by the first term in (6.2). Because the

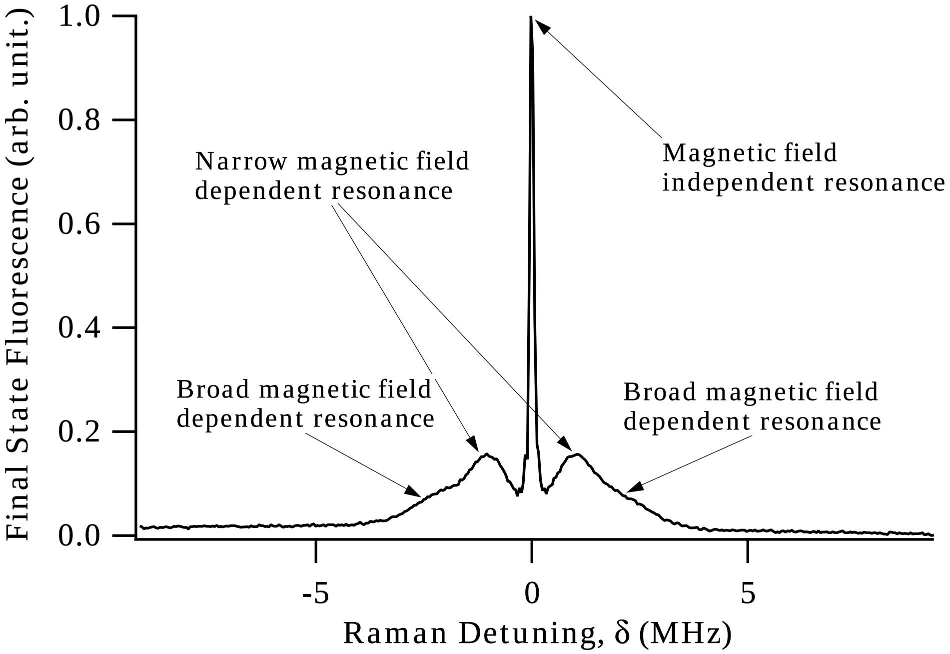

Figure 6.1: A typical Raman spectrum shows five peaks.

resonance is independent of the magnetic field gradient, the frequency width of this peak depends only on the spectral resolution.

On either side of the central peak is the magnetic field dependent structure which is described by the last four terms of (6.2). Within each side structure are two resonances. The resonance that occurs at lower Raman detunings is narrower, and a broader resonance occurs at larger Raman detunings as expected from the form of the resolution function.

6.1 Analysis of the Central Lineshape and the Resolution

In Section 1.2.2, the different resolution limits of Raman induced resonance imaging are defined. An analysis of the central lineshape shows that this imaging experiment is limited by the spectral resolution.

Figure 6.2 shows an expanded view of the central resonance and the fit lineshape function that is used to calculate the theoretical spectra later in this chapter. The lobes on the edge of the lineshape result from the oscillatory decay of the sinc squared function in the first term of (6.2). This sinc squared term is also shown in Figure 6.2 for the pulse duration of $8.8\,\mu$s as used in the experiment.

However, as shown in the figure, the sinc squared function is considerably narrower than the measured lineshape. This is due to a subtle effect caused by off-resonant transitions to the intermediate state of the Raman transition

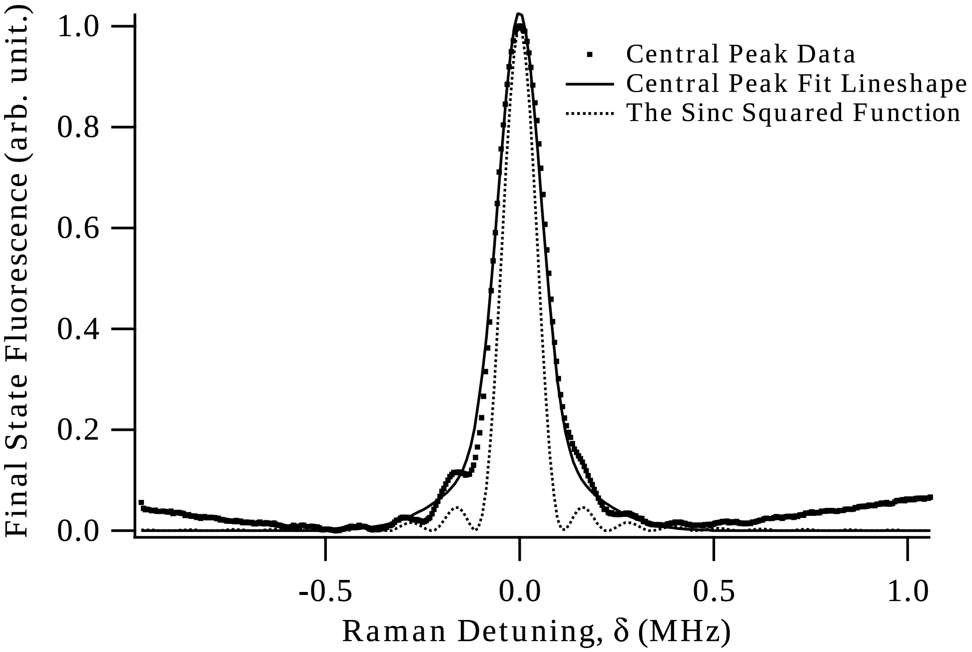

Figure 6.2: The magnetic independent resonance determines the spectral resolution.

during the Raman pulse (see Figures 5.7 and 2.1). The off-resonant transitions from the initial and final states causes the population in those states to decay with a finite lifetime. This lifetime causes radiative broadening of the Raman transition.

The transition rate out of either state can be calculated by keeping the $\Gamma/2$ terms in (2.11). For the Raman pulse used in this experiment as described in Sections 3.3.5 and 5.3, the full width of the radiative linewidth of the Raman transition is approximately 100 kHz. Consequently, the real lineshape in Figure 6.2 corresponds to the convolution of the lorentzian from this radiative broadening with the sinc squared spectral resolution of the square Raman pulse.

Rather than using the convolution for the lineshape in the analysis, a sum of two Gaussians is used to approximate the lineshape which simplifies the numerical analysis. The fit of the lineshape is comprised of a tall narrow gaussian corresponding to the central lobe and a short broad gaussian that approximates the area under the oscillatory decay. The 1/e half width of the narrow gaussian is $\Delta f = 77\,\mathrm{kHz}$. This spectral resolution corresponds to a spatial resolution given by (1.5). Before the spatial resolution can be calculated, the spatial tuning rate, discussed Section 1.2.2, which specifies how quickly the Raman transition tunes in the magnetic field, must be determined.

As mentioned in Section 4.5.2, the MOT gradient magnets produce a gradient of 33 G/cm along the $\hat{\boldsymbol{x}}$ axis of the experiment and a gradient of

16.5 G/cm along the $\hat{\boldsymbol{y}}$ and $\hat{\boldsymbol{z}}$ axes. (The axes are defined in Figure 5.4.) Since the radius of gradient coils is much larger than the size of the atomic spatial distribution, these gradients remain approximately constant over the entire distribution. When the magnetic field points along the $\hat{\boldsymbol{x}}$ axis of the experiment as it tends to do for atoms off-center along the $\hat{\boldsymbol{x}}$ axis, $\sin\theta(\boldsymbol{r}) \approx 1$ and the magnetic field dependent Raman transition that occurs tunes according to $(4/3)(\mu_B/h)B$ (Section 3.3.6) where B is the magnitude of the magnetic field. Therefore, the spatial tuning rate along the $\hat{\boldsymbol{x}}$ axis is given by

$$\frac{F_x}{h} = \frac{4}{3}\frac{\mu_B}{h} 33\,\mathrm{G/cm} = 62\,\mathrm{MHz/cm}. \tag{6.3}$$

With this spatial tuning rate along the $\hat{\boldsymbol{x}}$ axis and the$1/e$ spectral resolution of 77 kHz found by fitting the Gaussians to the lineshape, the half-width spatial resolution Δx along the $\hat{\boldsymbol{x}}$ axis is given by

$$\Delta x = \frac{h\Delta f}{F_x} = 12.4\,\mu\mathrm{m}. \tag{6.4}$$

The resolution along the $\hat{\boldsymbol{y}}$ axis is calculated similarly, but with a reduced gradient. Thus, the resolution along the $\hat{\boldsymbol{y}}$ axis is 25 μm. Along the $\hat{\boldsymbol{z}}$ axis, the resolution is increased to 50 μm because the Raman transition that tends to occur with magnetic fields along the $\hat{\boldsymbol{z}}$ axis tunes only by $(2/3)(\mu_B/h)B$. If the Raman beam is changed so that it propagates along the symmetry axis of the gradient magnets, the resolution would be 25 μm in all three dimensions.

The velocity limited resolution is calculated using (1.6). Since the atoms are moving with a velocity of approximately 1 m/s in the trap, the velocity limited resolution along the $\hat{\boldsymbol{x}}$ axis is 5 μm. By simply increasing the detuning from the intermediate state in the Raman pulse, the narrowness of the Raman linewidth would be limited only by the length of the pulse. Thus, this experiment could easily operate with the better velocity limited resolution. With the Raman beams oriented to produce the symmetric resolution and a larger detuning from the excited intermediate state, the velocity limited resolution is 7 μm in all three dimensions.

If the atoms are cooled before imaging, the velocity limited resolution would decrease until it reached the acceleration limited resolution (1.7). The acceleration limited resolution along the $\hat{\boldsymbol{x}}$ axis is 509 nm. In the symmetric tuning rate configuration, the three dimensional resolution is 641 nm.

6.2 Calculating a Theoretical Spectrum

To evaluate the expression for the resolution function (6.2), the angle of the quantization axes, $\theta(\boldsymbol{r})$ and the magnetic field magnitude, B, must be evaluated for the quadrupole field of the MOT. If we define the zero of the magnetic field to be the origin of the coordinate system, the expressions for $\cos\theta(\boldsymbol{r})$, $\sin\theta(\boldsymbol{r})$, and B are simple to derive.

Near the center of the two coils that create the quadrupole magnetic field of the MOT, the magnetic field is approximated by [86]

$$\boldsymbol{B}(\boldsymbol{r}) = \kappa(2x\hat{\boldsymbol{x}} + y\hat{\boldsymbol{y}} + z\hat{\boldsymbol{z}}) \tag{6.5}$$

where κ is given by the radial gradient of 16.5 G/cm. Therefore, the magnitude of the magnetic field is given by

$$B(\boldsymbol{r}) = |\boldsymbol{B}(\boldsymbol{r})| = \kappa(4x^2 + y^2 + z^2)^{1/2}. \tag{6.6}$$

Since the angle $\theta(\boldsymbol{r})$ is measured with respect to the $\hat{\boldsymbol{z}}$ axis the trigonometric expressions in (6.2) are given by

$$\cos\theta(\boldsymbol{r}) = \frac{B_z}{B} = \frac{z}{(4x^2 + y^2 + z^2)^{1/2}} \tag{6.7a}$$

$$\sin\theta(\boldsymbol{r}) = \frac{\sqrt{B_x^2 + B_y^2}}{B} = \frac{(4x^2 + y^2)^{1/2}}{(4x^2 + y^2 + z^2)^{1/2}}. \tag{6.7b}$$

The expressions (6.6) and (6.7) completely specify the resolution function (6.2) in the quadrupole magnetic field. To calculate a theoretical spectrum (6.1), an expression for $n(\boldsymbol{r})$, the atomic spatial distribution must be hypothesized.

Most generally, the spatial distribution may be written as a Taylor expansion of x, y, and z about $\boldsymbol{r} = 0$. A convenient form for this Taylor expansion is [87]

$$n(\boldsymbol{r}) = \sum_{m=0}^{\infty} \frac{1}{m!} (\boldsymbol{r} \cdot \nabla)^m n(\boldsymbol{0}). \tag{6.8}$$

However, this type of expansion rapidly leads to a large number of unknown coefficients. In fitting a calculated spectrum to the data based on this expansion, it is unlikely that the parameters could be established with much accuracy.

Since this is the first attempt at magnetic resonance imaging in a MOT, we make some reasonable assumptions about the MOT to reduce the number of fitting parameters. First, we make the assumption that the atomic spatial distribution in the MOT is described by a Gaussian of the form

$$n(\boldsymbol{r}) = \frac{1}{\pi^{3/2} u v^2} e^{-[(x-x_0)^2/u^2 + \{(y-y_0)^2 + (z-z_0)^2\}/v^2]} \tag{6.9}$$

where $\boldsymbol{r_0} = \{x_0, y_0, z_0\}$ is the offset of the MOT from the magnetic field zero and $\{u, v\}$ are the 1/e radii of the distribution. The offsets are caused by intensity imbalances between the counterpropagating trapping beams in the MOT. A Gaussian shape of this form is expected if the MOT acts as an ideal gas that is trapped in a harmonic potential with different restoring forces along the minor and major axes of the MOT ellipsoid [41]. Indeed, this ellipsoidal shape is seen in the laboratory (see Figures 4.28 and 4.29).

For large numbers of atoms, numerical studies and experiments have shown that the MOT is comprised of a dense central core with a diffuse outer region [41]. This behavior typically occurs when the detuning of the MOT trapping frequency (Section 4.5.1) is larger than the optical Rabi frequency of atoms in the trap. In this experiment, the detunings of the MOT trapping frequency range from $-20 - 44\,\mathrm{MHz}$ and the optical Rabi frequency in the MOT is estimated at less than $16\,\mathrm{MHz}$. Thus, the atomic spatial distribution in this experiment is assumed to be in this regime.

Although the diffuse outer core may contain a significant number of atoms, the density of atoms in the the outer core is typically at least an order of magnitude lower than that contained in the inner core [41]. Consequently, in this analysis, the contribution to the signal from the outer core is assumed to be negligible.

The presence of the dense inner core in this regime is due to a large restoring force that results from complex interactions among the sublevels of the hyperfine ground states. These interactions are fundamentally related to polarization gradient cooling in optical molasses [14]. As a function of detuning, numerical analysis shows that the dissipative forces in polarization gradient cooling are sharply peaked where the detuning is on the order of the light shift of the ground state [46]. The spatial dependence of the detuning in the MOT due to the quadrupole magnetic field causes the MOT's restoring force to peak where the Zeeman shift is on the order of the light shift of the ground states. The peak of the force defines the size of the minor and major axes of the inner core.

Along the axes, the Zeeman shift is on the order of the ground state light shift $\hbar\nu$ when

$$\mu_B \kappa u \sim \hbar\nu \qquad\qquad \mu_B \frac{\kappa}{2} v \sim \hbar\nu \tag{6.10}$$

$$u \sim \frac{\hbar\nu}{\mu_B \kappa} \qquad\qquad v \sim \frac{2\hbar\nu}{\mu_B \kappa}. \tag{6.11}$$

Consequently, in the regime of large detunings and a large number of atoms, the ratio of $u : v$ is 1:2. Including this result in the expression for $n(\boldsymbol{r})$ gives

$$n(\boldsymbol{r}) = \frac{2}{\pi^{3/2} v^3} e^{-[4(x-x_0)^2+(y-y_0)^2+(z-z_0)^2]/v^2}. \tag{6.12}$$

A comparison of $n(\boldsymbol{r})$ (6.12) and the trigonometric terms (6.7) suggests that the expressions can be simplified by changing to a scaled coordinate system $\{x', y', z'\}$ defined by

$$x' = 2x \qquad y' = y \qquad z' = z \tag{6.13a}$$

$$dx'dy'dz' = 2dxdydz. \tag{6.13b}$$

If we rewrite the density function as $n'(\boldsymbol{r'}) = n(\boldsymbol{r'})/2$, the spectrum in the new primed coordinate system is given by

$$\begin{aligned} P_f^{tot}(\delta) &= 2 \int d^3\boldsymbol{r'}\, n(\boldsymbol{r'}) P_f^{sa}(\boldsymbol{r'}, \delta) \\ &= \int d^3\boldsymbol{r'}\, n'(\boldsymbol{r'}) P_f^{sa}(\boldsymbol{r'}, \delta) \end{aligned} \tag{6.14}$$

where the trigonometric terms in $P_f^{sa}(\boldsymbol{r'}, \delta)$ (6.2) are written as

$$\cos\theta(\boldsymbol{r'}) = \frac{z'}{(x'^{\,2} + y'^{\,2} + z'^{\,2})^{1/2}} = \cos\theta' \tag{6.15a}$$

$$\sin\theta(\boldsymbol{r'}) = \frac{(x'^{\,2} + y'^{\,2})^{1/2}}{(x'^{\,2} + y'^{\,2} + z'^{\,2})^{1/2}} = \sin\theta' \tag{6.15b}$$

and

$$n'(\boldsymbol{r'}) = \frac{1}{\pi^{3/2} v^3} e^{-|\boldsymbol{r'} - \boldsymbol{r'_0}|^2/v^2}. \tag{6.16}$$

Also, the magnitude of the magnetic field (6.6) may written as

$$B(\boldsymbol{r'}) = \kappa|\boldsymbol{r'}| = \kappa r' \tag{6.17}$$

Thus, in the regime where the minor and major axes of the MOT ellipsoid differ by a factor of two, the expression for the spectrum may be easily integrated in spherical coordinates. Unless specifically stated, the coordinate system henceforth is the scaled system and the primes will no longer be explicitly indicated.

Of the three integration variables (r, θ, ϕ) in (6.14), the integral over ϕ is treated first. The only ϕ dependence in the spectrum occurs in $|\boldsymbol{r} - \boldsymbol{r_0}|^2$. The angle ϕ is defined as the angle between the $\hat{\boldsymbol{x}}$ axis and the projection of the magnetic field onto the $\hat{\boldsymbol{x}}$-$\hat{\boldsymbol{y}}$ plane as shown in Figure 2.4. Expanding

$|\boldsymbol{r} - \boldsymbol{r_0}|^2$ gives

$$|\boldsymbol{r} - \boldsymbol{r_0}|^2 = r^2 + r_0^2 - 2rr_0\hat{\boldsymbol{r}} \cdot \hat{\boldsymbol{r_0}} \tag{6.18a}$$

$$\hat{\boldsymbol{r}} \cdot \hat{\boldsymbol{r_0}} = \sin\theta \sin\theta_0 \cos(\phi - \phi_0) + \cos\theta \cos\theta_0 \tag{6.18b}$$

where θ_0 and ϕ_0 denote the direction that the spatial distribution is offset from the zero of the magnetic field. Performing the ϕ integral directly on $n(r, \theta, \phi)$ (6.16) gives

$$n(r, \theta) = \frac{2}{\pi^{1/2} v^3} e^{-r_0^2/v^2} e^{-r^2/v^2} e^{(2rr_0/v^2)\cos\theta\cos\theta_0} I_0[(2rr_0/v^2)\sin\theta\sin\theta_0] \tag{6.19}$$

where I_0 is the zeroth order of the modified Bessel function of the first kind. Note that the ϕ_0 dependence is no longer present in (6.19) due to the spherical symmetry we have assumed.

The r integration of the magnetic field dependent terms in (6.14) may be performed by making a delta function approximation for the lineshape. As mentioned in the discussion of Figure 6.1, the lineshape of the sinc squared function when convoluted with the lorentzian Raman lineshape gives a lineshape that may be approximated by two Gaussians. From fitting to the central peak, the two Gaussians are found to have the form

$$g(\delta) = \alpha_0 e^{-\delta^2/\nu_0^2} + \alpha_1 e^{-\delta^2/\nu_1^2} \tag{6.20}$$

where $\alpha_0 = 0.87$, $\alpha_1 = 0.15$, $\nu_0 = 0.077\,\mathrm{MHz}$, and $\nu_1 = 0.22\,\mathrm{MHz}$. Note that the lineshape at $\delta = 0$ evaluates to ≈ 1 just as the sinc squared function does.

Due to the narrow lineshape, the broad magnetic field dependent contributions are resonant only at particular r as determined by δ. In the scaled coordinate system, each magnetic field dependent term has the form

$$r^2 \sin\theta n(r,\theta) f(\theta) \left(\alpha_0 e^{-(\delta - \frac{\gamma\mu_B\kappa r}{h})^2/\nu_0^2} + \alpha_1 e^{-(\delta - \frac{\gamma\mu_B\kappa r}{h})^2/\nu_1^2}\right) \tag{6.21}$$

where $f(\theta)$ contains the appropriate sine squared term and γ is the $\pm 2/3$ or $\pm 4/3$ tuning rate of the Raman transition. The $r^2 n(r,\theta)$ factor varies much more slowly in r than the sharply peaked lineshape function. Therefore, to approximate the r integral, we will assume that r is a constant equal to $\delta h/(\mu_b\kappa\gamma)$ in the slowly varying factor. The offset due to the Raman detuning δ in the Gaussians of the magnetic field dependent terms allows r to be integrated from $-\infty$ to ∞ for detunings larger than the linewidth which is where these terms contribute as shown in Figure 6.1. Performing the r integral on the magnetic field dependent terms gives

$$\frac{r_p^2(|\delta|)a_0}{\gamma^3} \sin\theta n(r_p/\gamma,\theta) f(\theta) \tag{6.22}$$

$$r_p(|\delta|) = \frac{h|\delta|}{\mu_B\kappa} \qquad a_0 = \frac{h\sqrt{\pi}}{\mu_B\kappa}(\alpha_0\nu_0 + \alpha_1\nu_1). \tag{6.23}$$

Because we have made the delta function approximation in deriving (6.22), only the terms in (6.2) with positive (negative) Raman tuning factors contribute for positive (negative) Raman detunings. Because the magnetic field independent term has no radial dependence in its lineshape, we cannot use the delta function approximation to evaluate that term.

As discussed in Section 5.3, the intensity and timing τ of the Raman pulse is set so that $2\sqrt{2}\beta_0\tau/9 = 2\pi$. Using this as well as (6.19), (6.20), (6.22), and (6.23), the spectrum (6.14) may be written as

$$\begin{aligned} P_f^{tot} = g(\delta) \int_0^\infty dr \int_0^\pi d\theta r^2 \sin\theta\, n(r,\theta) \sin^2(\frac{\pi}{2}\sin\theta) \\ + \frac{1}{2} r_p^2(|\delta|) a_0 \int_0^\pi d\theta \sin\theta \left[\left(\frac{3}{4}\right)^3 n(\frac{3}{4} r_p(|\delta|), \theta) \sin^2(\frac{\sqrt{3}}{2}\pi \sin\theta) \right. \\ \left. + \left(\frac{3}{2}\right)^3 n(\frac{3}{2} r_p(|\delta|), \theta) \sin^2(\pi \sin\theta) \right] \end{aligned} \tag{6.24}$$

In an ideal experiment, this spectrum (6.14) would completely represent the signal.

However, the non-ideal behavior of the tunable Raman acousto-optic modulator (AOM) obliges us to modify (6.24). As this AOM is tuned to select different Raman detunings, δ, the power output of the AOM and the alignment of the AOM's output into the Raman beam optical fiber changes slightly. The resulting power variation causes three effects.

First, because the ratio of the intensities of the two Raman fields is critical to balancing the light shifts of the initial and final states, the power change in one Raman field will unbalance the light shifts. This effectively causes the Raman detuning to be a nonlinear function of the tunable Raman field frequency. However, due to the low intensity Raman fields used in this experiment, this effect creates a nonlinearity of less than 0.1% and will be neglected.

The second effect arises from the calculation of the Raman Rabi frequency. Because the Raman Rabi frequency is proportional to the square root of each Raman field intensity, the Raman Rabi frequency will change slightly as a function of Raman detuning due to the power variation in the tuned beam. To compensate for this, each Raman pulse area in (6.24), which is proportional to the Raman Rabi frequency, is modified according to

$$\phi_{eff} \rightarrow \phi_{eff}\sqrt{1+\epsilon(\delta)} \tag{6.25}$$

where ϕ_{eff} is the effective pulse area and $\epsilon(\delta)$ is the fractional variation in the tunable Raman field power. A graph of $\epsilon(\delta)$ is shown in Figure 6.3.

A third effect occurs due to the off resonant spontaneous transitions to the excited intermediate states of the Raman transition. When the atoms in the excited states decay, some of them decay to the final state. If the power in the Raman beam remained constant as function of Raman detuning, the background signal would remain constant and would be subtracted from the spectrum in the normalization procedure. Because the background signal varies slightly as a function of detuning, a term proportional to $\epsilon(\delta)$ must be added to (6.24).

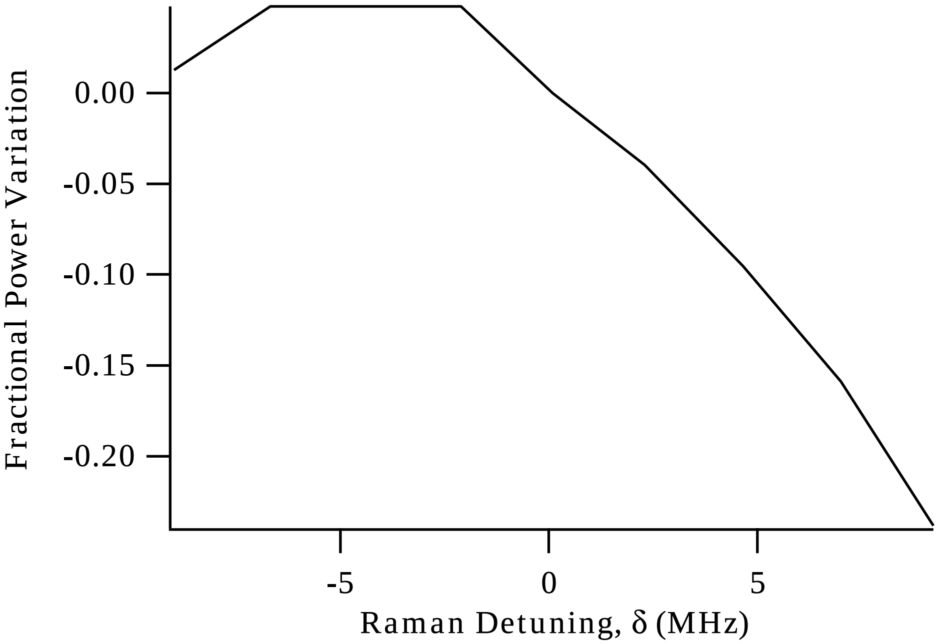

Figure 6.3: The fractional power variation in the tunable Raman field.

Thus, the entire fitting function is given by

$$\begin{aligned}P_f^{tot} &= w_0 + w_1\epsilon(\delta) \\ &\quad + w_2 g(\delta)\int_0^\infty dr \int_0^\pi d\theta r^2 \sin\theta\, n(r,\theta)\sin^2(\frac{\pi}{2}w_3\sqrt{1+\epsilon(\delta)}\sin\theta) \\ &+ \frac{1}{2}r_p^2(|\delta|)a_0\int_0^\pi d\theta\sin\theta\left[\left(\frac{3}{4}\right)^3 n(\frac{3}{4}r_p(|\delta|),\theta)\sin^2(\frac{\sqrt{3}}{2}w_3\sqrt{1+\epsilon(\delta)}\pi\sin\theta)\right. \\ &\qquad \left. + \left(\frac{3}{2}\right)^3 n(\frac{3}{2}r_p(|\delta|),\theta)\sin^2(\pi w_3\sqrt{1+\epsilon(\delta)}\sin\theta)\right] \end{aligned} \tag{6.26a}$$

where

$$n(r,\theta) = \frac{2}{\pi^{1/2}w_4^3}e^{-w_5^2/w_4^2}e^{-r^2/w_4^2}e^{(2rw_5/w_4^2)\cos\theta\cos w_6}I_0[(2rw_5/w_4^2)\sin\theta\sin w_6] \tag{6.26b}$$

$$r_p(|\delta|) = \frac{h|\delta|}{\mu_B\kappa} \qquad a_0 = \frac{h\sqrt{\pi}}{\mu_B\kappa}(\alpha_0\nu_0+\alpha_1\nu_1) \tag{6.26c}$$

and w_i are the fitting parameters. The meaning of each fitting parameter is shown in Table 6.1.

Additional fitting parameters are included in n so that the radial displacement and direction of the atomic distribution with respect to the magnetic field zero and the distribution's size may be determined. To account for possible errors in the measurement of the Raman beam size and power, another parameter, w_3, allows the fitting routine to vary the pulse area.

The theoretical spectra are integrated using Romberg integration [84]. In this method of integration, trapezoidal integration is successively performed

Fitting Parameter	Meaning
w_0	y-axis offset
w_1	variable background scaling
w_2	spectrum scaling
w_3	pulse area adjustment (≈ 1)
w_4	cloud size (v)
w_5	cloud radial offset (r_0)
w_6	cloud offset direction (θ_0)

Table 6.1: The fitting parameters used in the calculated spectra.

with an increasing number of points. The result of each trapezoidal integration is stored as function of the resolution that was used to evaluate the integrand. As more points are used, the resolution becomes smaller, tending toward zero. Romberg integration uses the results of the trapezoidal integration and extrapolates them to an infinitesimal (≈ 0) stepsize.

Figure 6.4 shows how the calculated spectra vary as the physical parameters for the trapped cloud are changed. The reference spectra is calculated for a trapped atom cloud centered on the magnetic field zero with 1/e major axes radii of 0.5 mm. The asymmetries due to the tunable Raman AOM were minimized for these calculated spectra. The heights of the central resonance due to the magnetic field independent transition are normalized to one for each plot.

As the trapped cloud size decreases, in a) of Figure 6.4, the spectral width of the Raman resonance decreases. As the trap becomes smaller, the atoms become concentrated in the low field regions of the quadrupole magnetic field. Consequently, the Raman transition resonance frequencies are spread over a

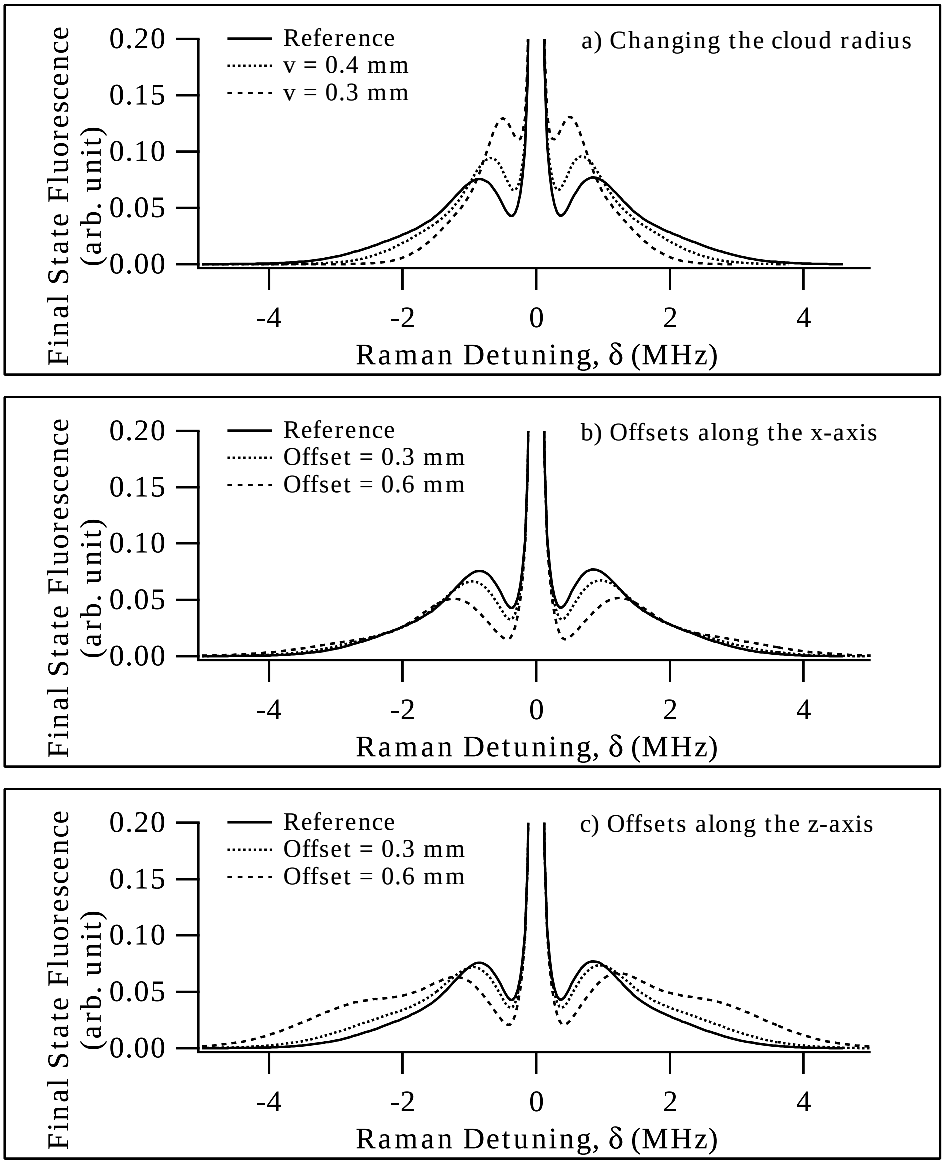

Figure 6.4: Calculated spectra for different spatial distributions: a) the size of the cloud is varied, b) the trap is offset along the x-axis, c) the trap is offset along the z-axis. The Reference plot was calculated for a trapped atom cloud centered on the magnetic field zero with 1/e major axes radii of 0.5 mm. For each plot, the central magnetic field independent transition peak is normalized to one.

smaller frequency range.

When the trap is offset along the x-axis, the $\Delta m = \pm 1$ transitions occur preferentially, as described in Section 2.2. These transitions include the magnetic field independent transitions and those that tune according to $\pm 4\mu_B B/3h$. Consequently, the $\pm 2\mu_B B/3h$ peaks are deemphasized as the trap is displaced along the x-axis in b) of Figure 6.4.

In c) of Figure 6.4, the trap is displaced along the z-axis. These displacements emphasize the $\Delta m = 0$ transitions that tune according to $\pm 2\mu_B B/3h$. As the offset increases, the $\Delta m = 0$ transition peaks become more distinguishable from the other magnetic field dependent transitions. However, the $\Delta m = 0$ transitions do not become significantly taller because the transition is also broadened as the trap is displaced.

6.3 The Measured Raman Spectra

Four different experimentally measured spectra and their fitting functions are shown in Figures 6.5 and 6.6. In the calculated spectra, the pulse area parameter w_3 was held constant at 1 which assumes an accurate measurement of the pulse area. The fits in Figures 6.5 and 6.6 improve significantly, as discussed below, when the pulse area is allowed to vary within the accuracy of the pulse area measurement (see Figures 6.8 and 6.9). The spectra in Figures 6.5 and 6.6 were taken at different trap laser beam detunings which affects the size of the trap. As the detuning increases, the MOT becomes larger. In

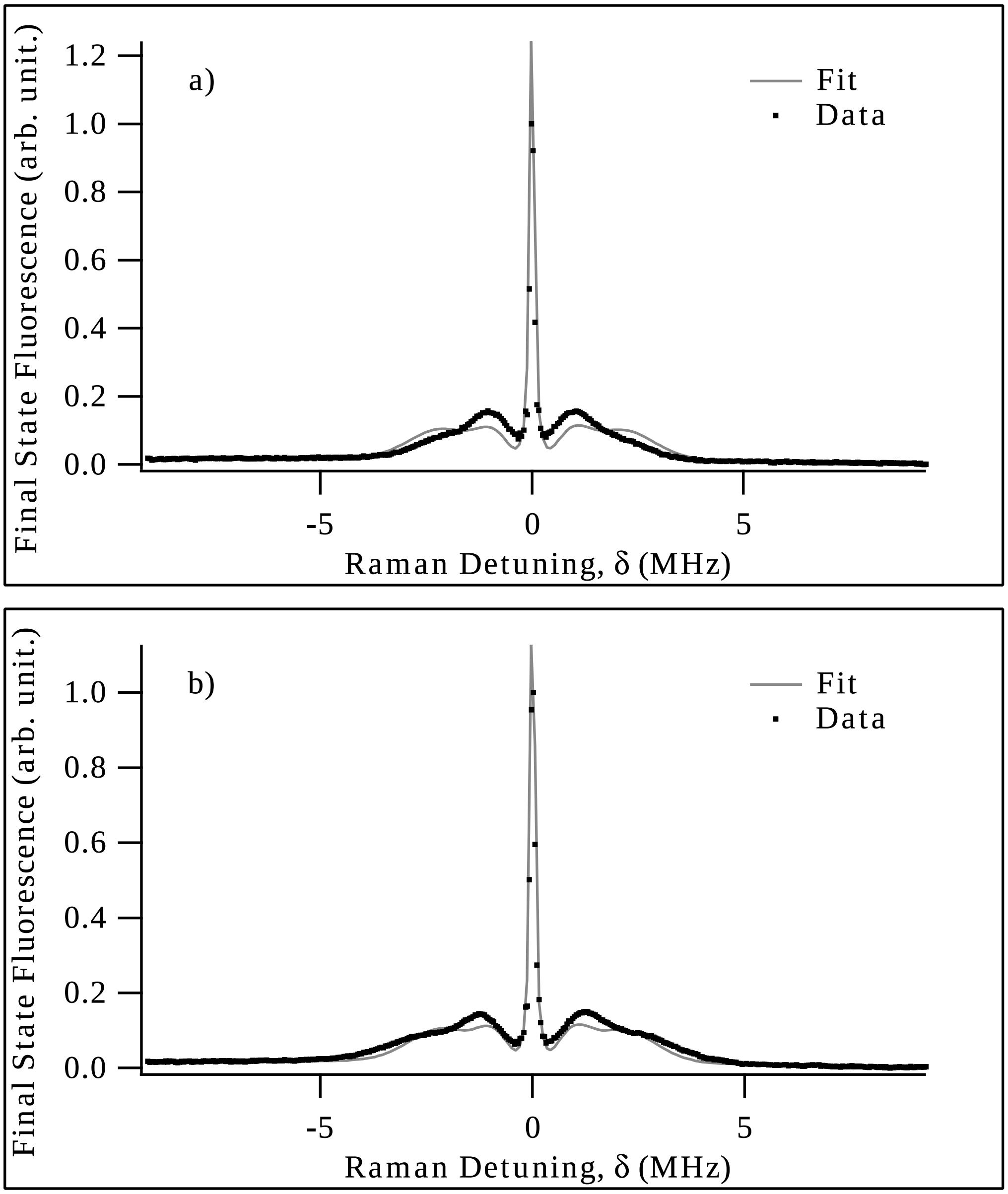

Figure 6.5: Two different Raman spectra taken with different trap laser beam detunings: a) $\Delta = -3.4\gamma$, b) $\Delta = -4.7\gamma$; $\gamma = 5.9\,\text{MHz}$.

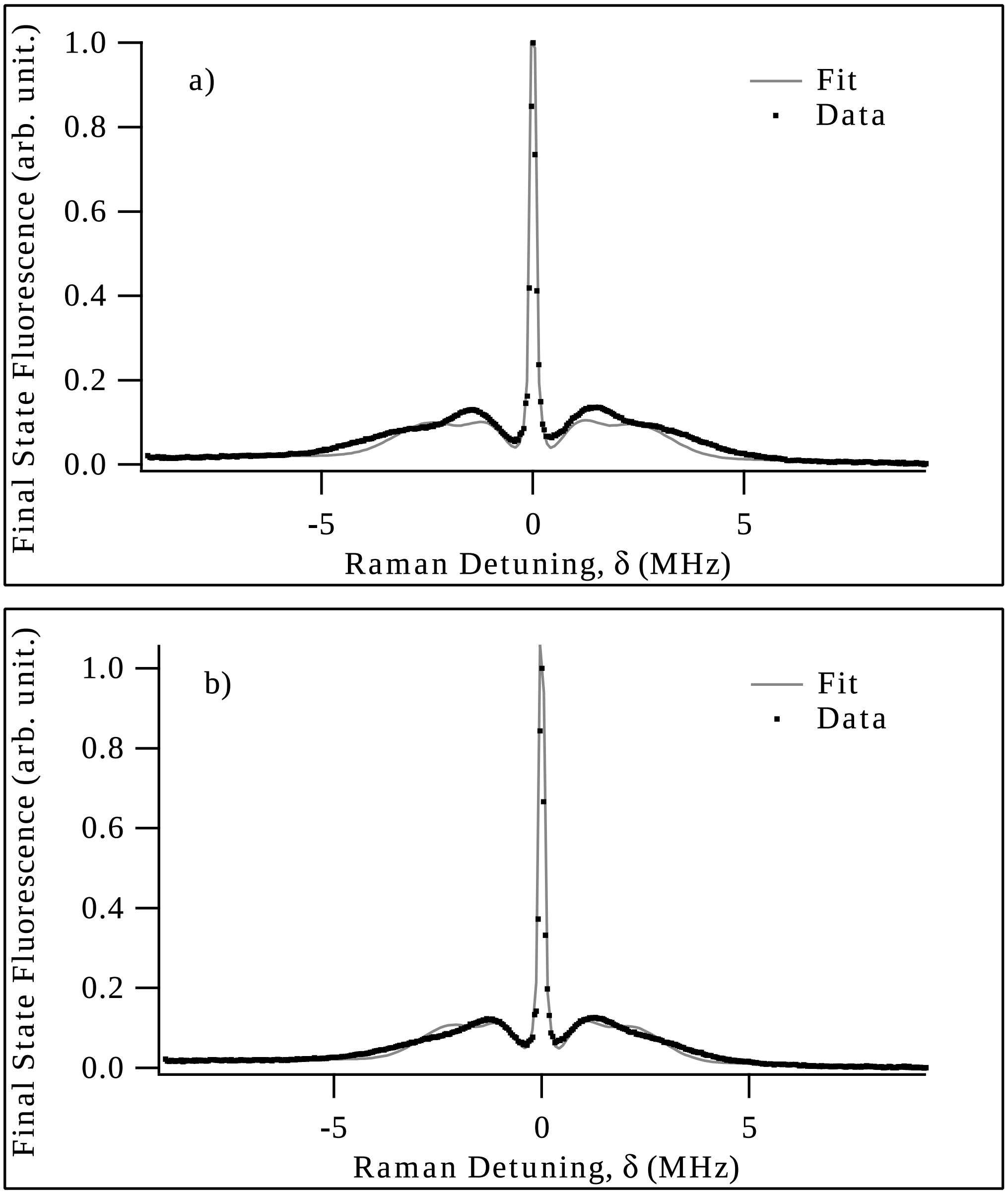

Figure 6.6: Additional Raman spectra taken with different trap laser beam detunings: a) $\Delta = -6.2\gamma$, b) $\Delta = -7.6\gamma$; $\gamma = 5.9\,\mathrm{MHz}$.

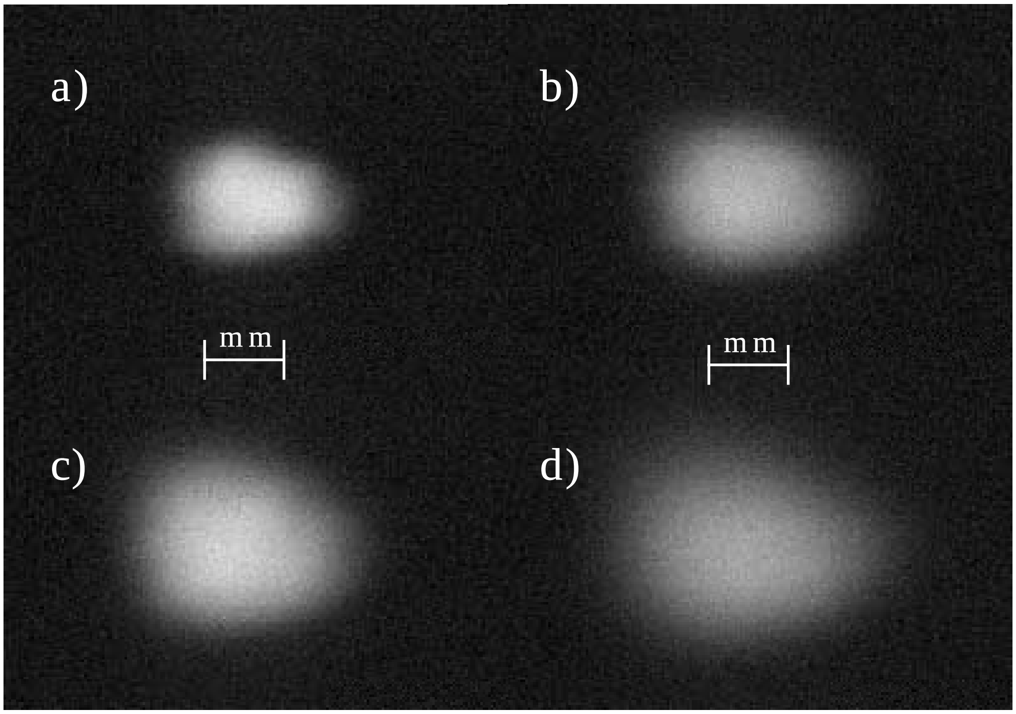

Figure 6.7: Fluorescence images of the trap taken with different trap laser beam detunings: a) $\Delta = -3.4\gamma$, b) $\Delta = -4.7\gamma$, c) $\Delta = -6.2\gamma$, d) $\Delta = -7.6\gamma$; $\gamma = 5.9\,\mathrm{MHz}$.

Figure 6.7, fluorescence pictures of the trap at these different detunings show this general trend, although their two-dimensional view is averaged over the depth of the trap. As one would expect, the spectra in Figures 6.5 and 6.6 get broader for larger MOT sizes because the atoms are spread over a larger and larger range of magnetic field strengths.

The calculated spectra made a better fit to the measured spectra at larger MOT detunings. Since we assumed that the sizes of the minor and major axes of the central feature in the MOT—a feature which is indiscernible in the fluorescence pictures—are related by a ratio of 1:2, the increasingly better fits at larger detunings indicate that the approximation becomes more valid at larger trap laser beam detunings.

When the Raman pulse area parameter w_3 is allowed to vary as a fitting parameter, the fits to the data become noticeably better at the lower trap laser beam detunings, as shown in Figures 6.8 and 6.9. For the spectrum taken with the lowest trap detuning, the fitting routine reduced the calculated Raman pulse area to 85% of its measured value, which was the minimum allowed by the constraints we placed on w_3. For larger trap detunings, the fitting routine returned a Raman pulse area which was 90% of its measured value. An error of up to 15% in an experimentally determined Raman pulse area is reasonable.

The 1/e trap sizes along the major axes are shown in Figure 6.10 for the different trap laser beam detunings. The solid line shows the results when the pulse area is constrained to 1, and the dashed line shows the results when the fitting routine is allowed to vary the pulse area. Both methods for fitting the data indicate the same trends and approximately the same cloud sizes. The error bars denote the square root of the appropriate diagonal matrix element of the covariance matrix determined by the fitting program. The points in the averaged Raman spectra are weighted by the reciprocal of their standard deviations during the fit. These weights are used by the fitting routine to determine the errors in the fit parameters. As such, the errors bars do not indicate the validity of the 1:2 axes size ratio model. However, the error bars, which represent the sensitivity of the chi-squared to variations

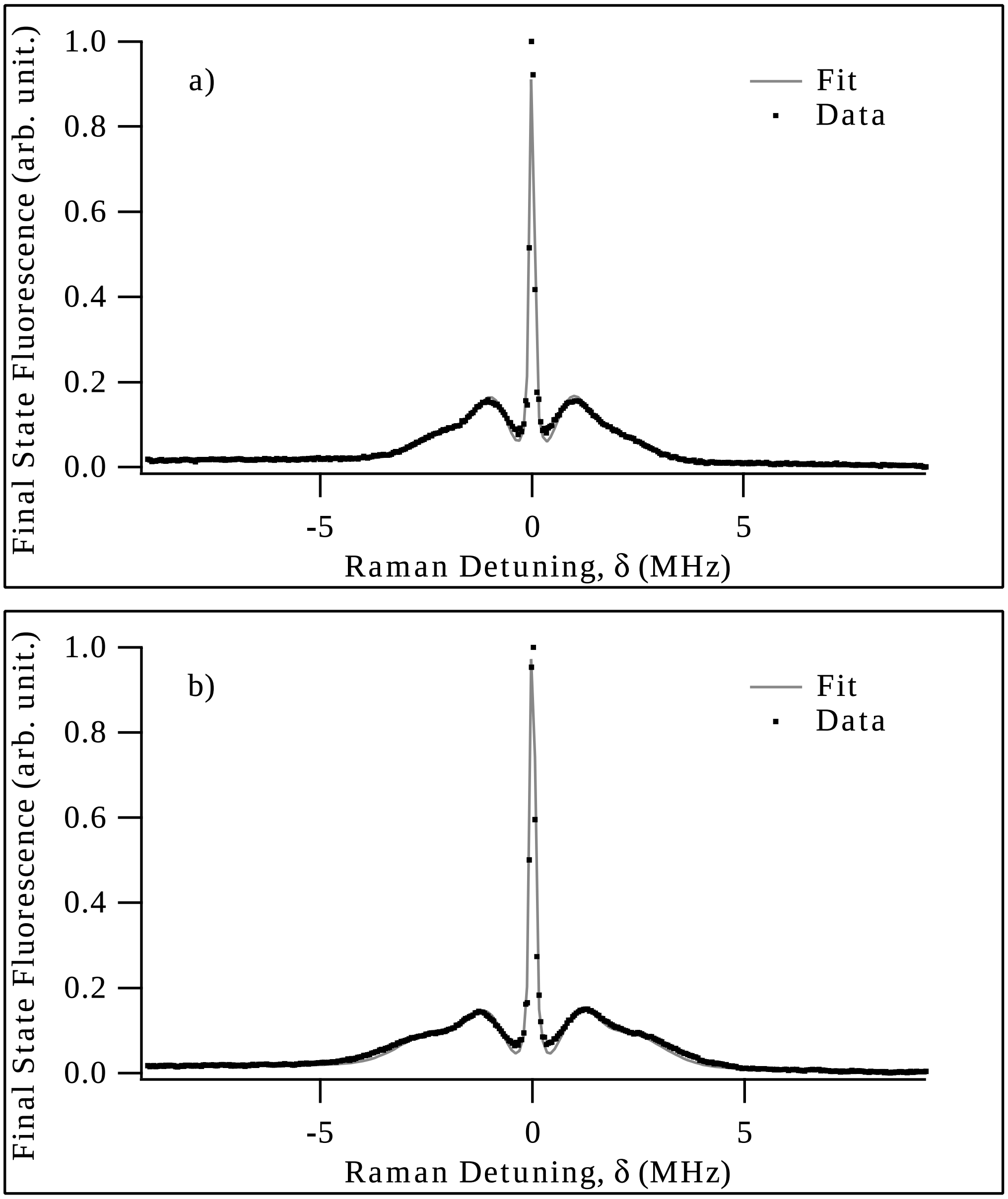

Figure 6.8: Fits of the different Raman spectra when the Raman pulse area is a fitting parameter: a) $\Delta = -3.4\gamma$, b) $\Delta = -4.7\gamma$; $\gamma = 5.9\,\text{MHz}$.

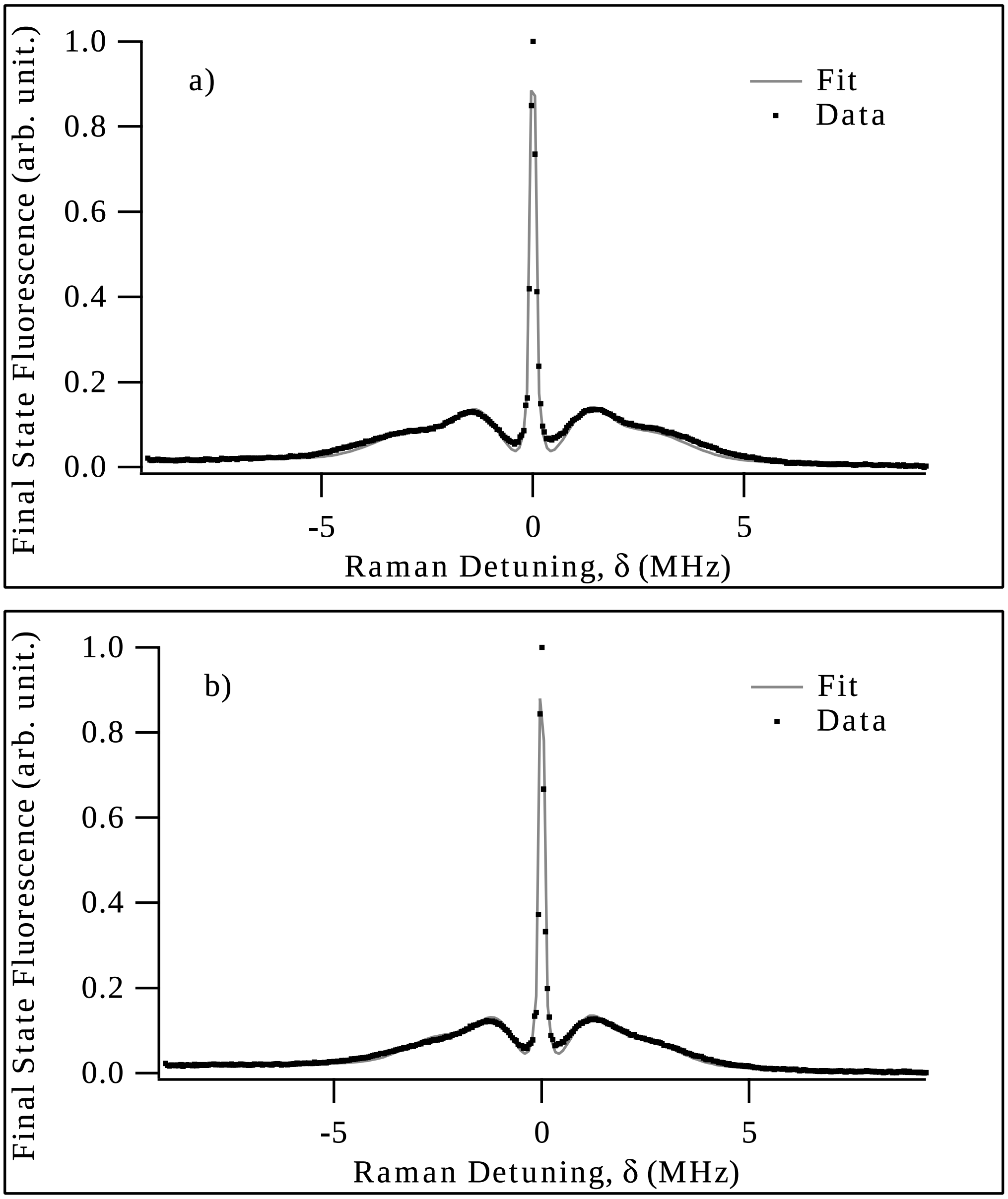

Figure 6.9: Additional fits of Raman spectra when the Raman pulse area is a fitting parameter: a) $\Delta = -6.2\gamma$, b) $\Delta = -7.6\gamma$; $\gamma = 5.9\,\mathrm{MHz}$.

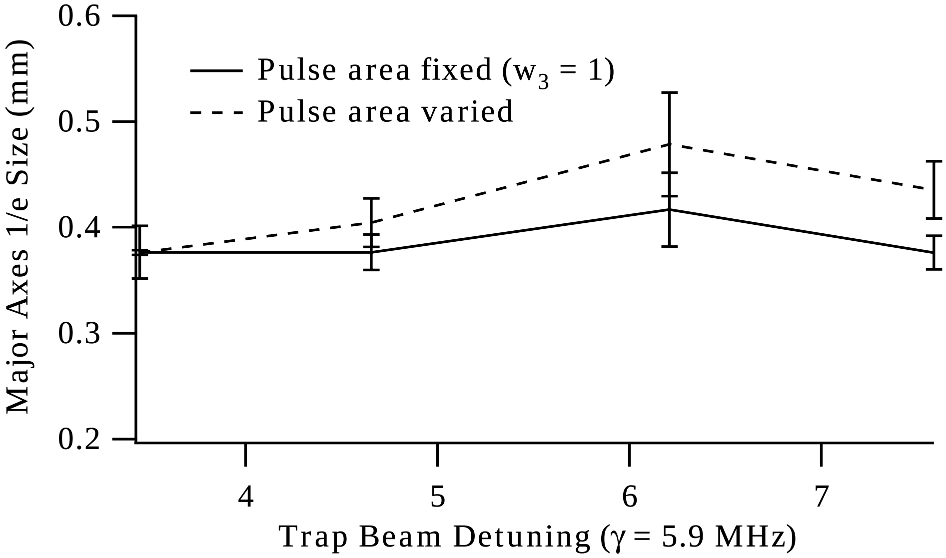

Figure 6.10: The 1/e trap size along the major axes as a function of trap laser beam detuning. The error bars denote the square root of the appropriate diagonal matrix element of the covariance matrix determined by the fitting program.

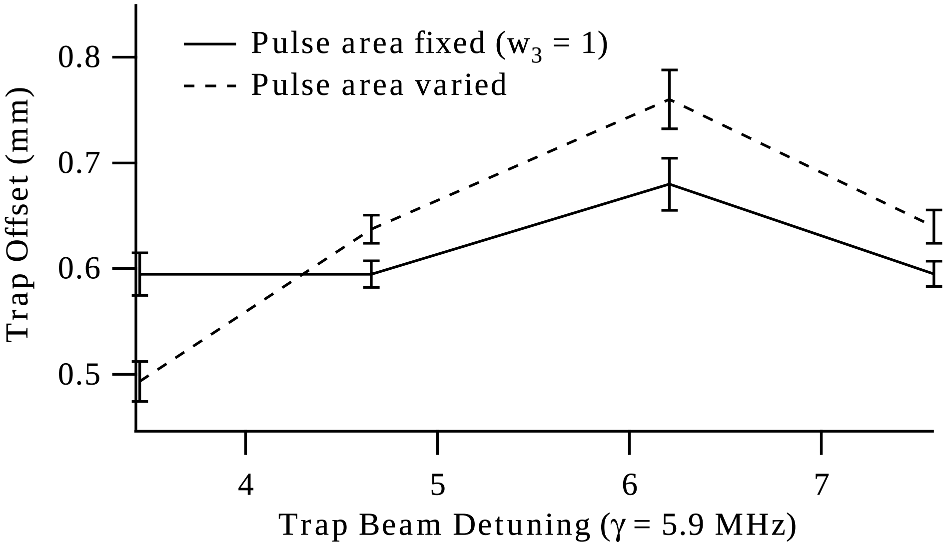

Figure 6.11: The offset of the trap with respect to the magnetic field zero. The error bars denote the square root of the appropriate diagonal matrix element of the covariance matrix determined by the fitting program.

in the parameters, show that resonance imaging can accurately measure the physical parameters of the trapped atom cloud.

As the detuning is increased, the trap increases in size as expected. From the fluorescent spectra shown in Figure 6.7, it appears that the trap continues to increase in size beyond a detuning of 6.5 linewidths. However, the size determined by Raman induced resonance imaging shows that the trap size decreases beyond this detuning. Perhaps this is due to an increasing dominance in the spectra of the small dense central component of the distribution at these detunings.

Figure 6.11 shows the trap offset with respect to the zero of the magnetic field between the MOT gradient coils. The offset is considerable compared to the size of the trap. Both the fixed and adjustable Raman pulse area fits show the same general trends and magnitudes for the trap offsets. The angle of the offset ($\theta_0 = w_6$) was calculated to be ≈ 0 in each fit meaning that the atoms are offset along the axis of the Raman beam. The error bars in these plots were calculated by the fitting routine as described in the previous discussion of Figure 6.10.

These offsets are due to imbalances in the intensity between the counter propagating trapping beams. The intensity imbalance between one of the input and output trapping beams was measured to be 10% with a power meter. Because the center of the distribution will be located where the scattering forces from the forward and backward going MOT beams are equal, the center of the MOT shifts from the magnetic field zero to a nonzero magnetic field region where the forces are balanced. By equating the magnitude of the scattering forces due to each beam, one can show that a ten percent intensity imbalance easily leads to a trap offset on the order of 1 mm.

By using the values for r_0, v, θ_0 returned from fitting the theoretical spectrum to the data, the three dimensional density distribution of the MOT can be visualized. Returning to the unscaled coordinate system in the lab, the density distribution is written as

$$n(x,y,z) = \frac{2}{\pi^{3/2}v^3}e^{-[4(x-x_0)^2+(y-y_0)^2+(z-z_0)^2]/v^2} \tag{6.27a}$$

$$x_0 = \frac{1}{2}r_0 \sin\theta_0 \cos\phi_0 \tag{6.27b}$$

$$y_0 = r_0 \sin\theta_0 \sin\phi_0 \tag{6.27c}$$

$$z_0 = r_0 \cos\theta_0. \tag{6.27d}$$

Because the parameter ϕ_0 cannot be determined by using only one Raman beam, we will assume $\phi = 0$. The 1/e constant density surface is plotted in Figure 6.12 using (6.27) with the parameters $r_0 = 0.6\,\mathrm{mm}$, $v = 0.376\,\mathrm{mm}$, and $\theta_0 = 0$ that were determined for the trap when the detuning is $\Delta = -7.6\gamma$. The origin is the magnetic field zero point centered between the two gradient coils.

The two-dimensional cross sections of the three-dimensional density in Figures 6.13, 6.14 and 6.15 show the offset of the MOT and the scaling of the minor and major axes of the trap. These figures were also calculated with the parameters determined from the spectra in which the trap laser beam detuning was $\Delta = -7.6\gamma$.

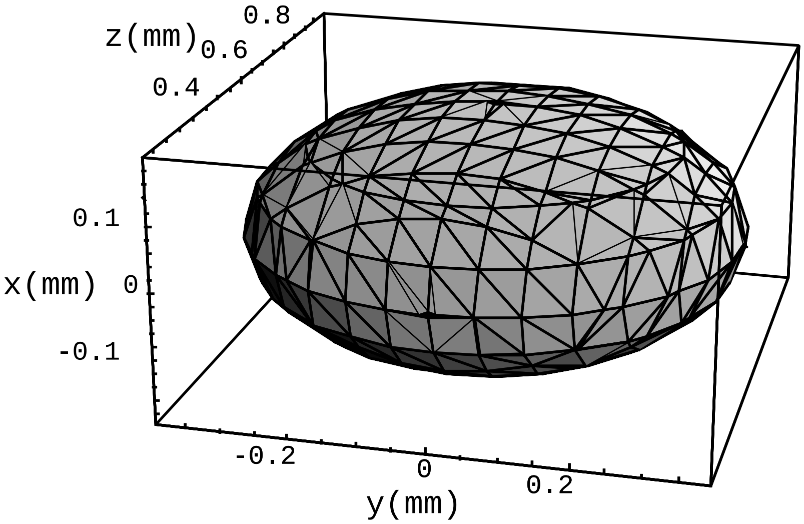

Figure 6.12: The 1/e constant density surface of the MOT with the trap laser detuning set at $\Delta = -7.6\gamma$; $r_0 = 0.6\,\mathrm{mm}$, $v = 0.376\,\mathrm{mm}$, and $\theta_0 = 0$.

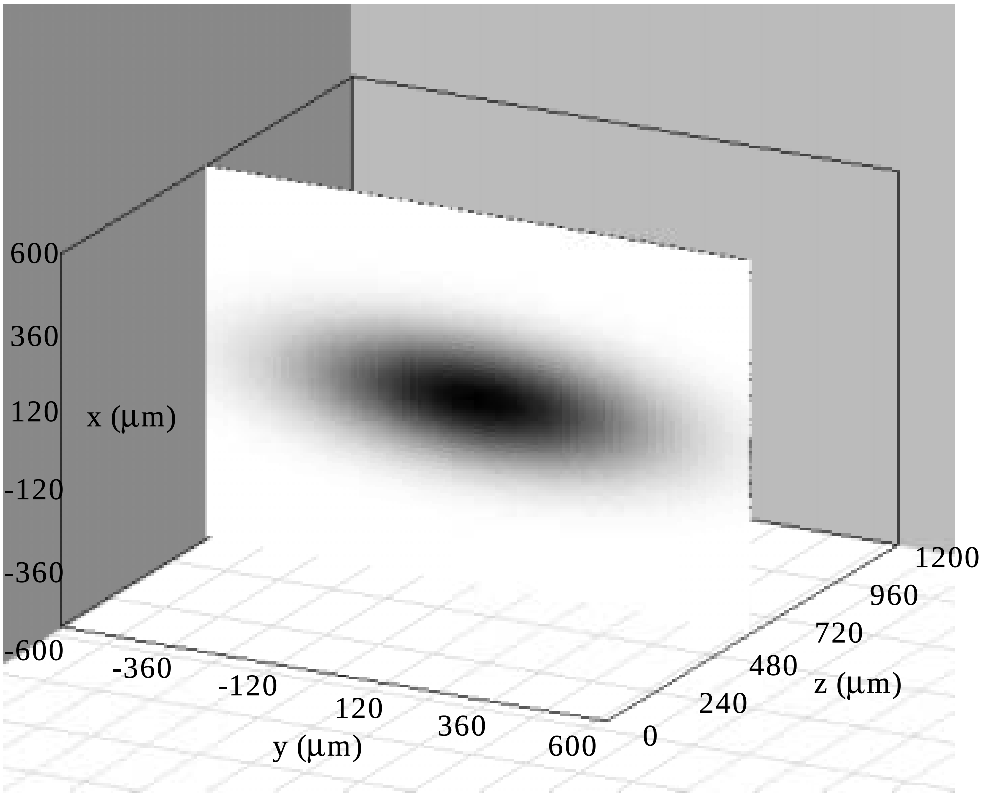

Figure 6.13: The density in the $x - y$ plane at $z = 600\ \mu m$; $r_0 = 600\ \mu m$, $v = 376\ \mu m$, and $\theta_0 = 0$ as determined for the atomic distribution when the trap laser beam was detuned by $\Delta = -7.6\gamma$.

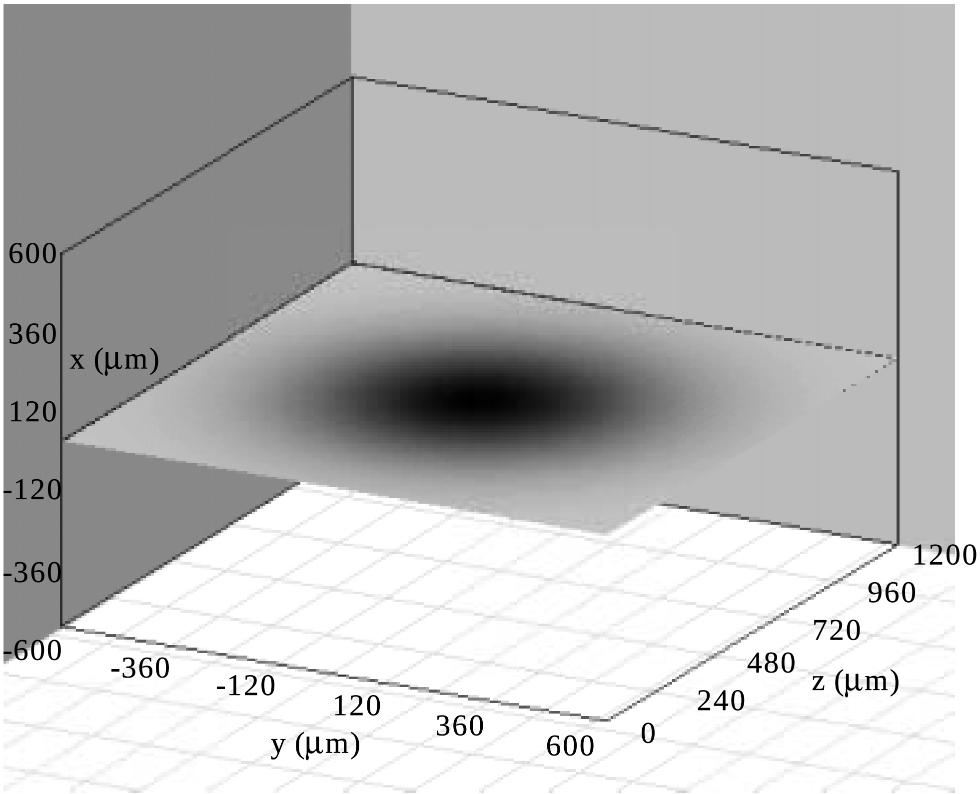

Figure 6.14: The density in the $y - z$ plane at $x = 0$ μm; $r_0 = 600$ μm, $v = 376$ μm, and $\theta_0 = 0$ as determined for the atomic distribution when the trap laser beam was detuned by $\Delta = -7.6\gamma$.

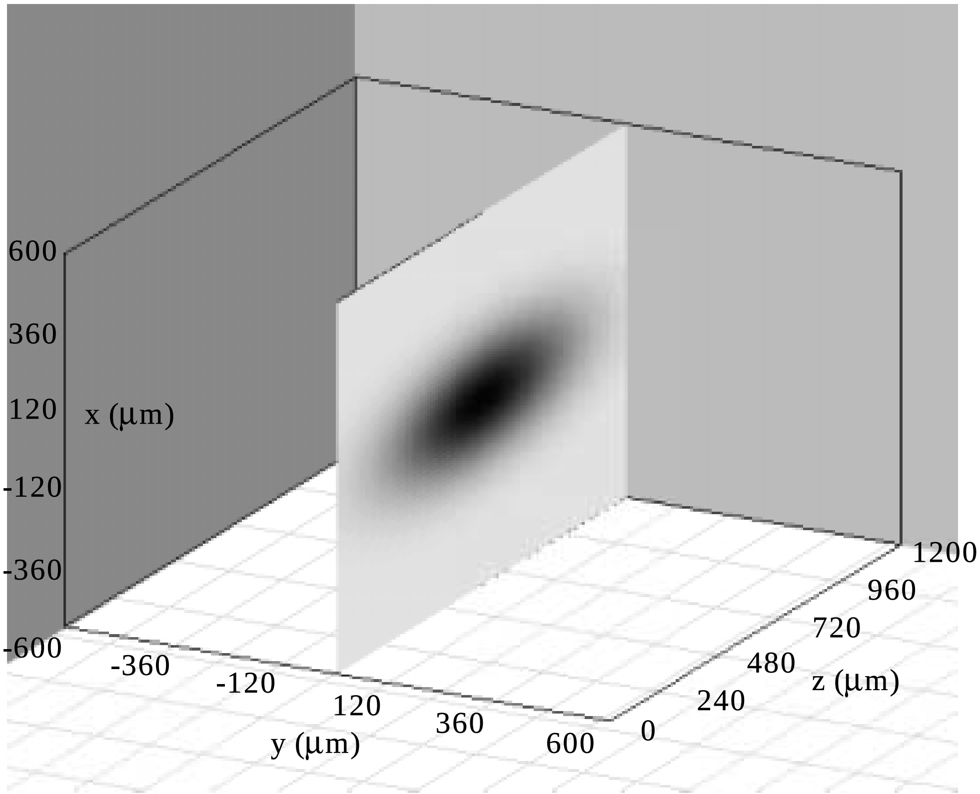

Figure 6.15: The density in the $x - z$ plane at $y = 0$ μm; $r_0 = 600$ μm, $v = 376$ μm, and $\theta_0 = 0$ as determined for the atomic distribution when the trap laser beam was detuned by $\Delta = -7.6\gamma$.

Chapter 7

Conclusion

This dissertation has demonstrated Raman induced resonance imaging of atoms in an optically thick magneto-optic trap. Raman induced resonance imaging is particularly suited to study optically thick atomic distributions with high resolution. Since only a small fraction of the atoms are resonant with a Raman pulse at a particular frequency, the effective optical thickness of the atomic distribution is significantly reduced. Fluorescence imaging, the most common technique currently in use, is unsuitable for optically thick samples because the beams that probe the sample are significantly attenuated within the trap.

Both fluorescent imaging of MOTs and phase contrast imaging of Bose Einstein condensates are two-dimensional techniques. Because the depth of atomic density distributions is averages along the camera's line of sight, small centrally located density variations are not easily detectable with these methods. Alternatively, by tailoring the sampling function of resonance imaging to the symmetry of the distribution of interest, these density variations are more likely to be visible. In this experiment, the quadrupole magnetic field of the MOT was used to create a spatially varying Raman resonance transition strength and frequency. Consequently, the atoms were imaged in thin ellipsoidal shells which matches the symmetry of the MOT.

7.1 Summary

In this first resonance imaging experiment in traps, the resolution was 12 μm which matches the best resolution that has been obtained by two dimensional fluorescence imaging. Simple changes to the experiment will yield 7 μm resolution in three dimensions, rivaling what has been obtained using phase contrast imaging that employed expensive cameras and large diameter optics.

In Chapter 2 of this dissertation, the effect of a non-uniform magnetic field on the ^{6}Li Raman transitions was explored. Using an approach that may be generalized for other alkali atoms, an expression for the ^{6}Li Raman spectrum in a spatially varying magnetic field was derived. Consequently, the theoretical techniques used in this chapter may be used to develop magnetic resonance imaging techniques for other atoms in different magnetic field configurations.

The theoretical results from Chapter 2 were applied to the measured Raman spectra in Chapter 6. In deriving an expression for the Raman spectra expected in this experiment, we made the assumption that the MOT contained a two component atomic density distribution. A small dense core of atoms surrounded by a diffuse outer region is expected when magneto-optic traps are operated with large magnetic field gradients and large trap laser beam detunings like those used in this experiment [41,45,46]. The dense core is predicted to arise from strong polarization gradient forces which only have a significant spatial extent in the large detuning and large magnetic field gradient regime. Because the strong polarization gradient forces are sharply peaked at a particular Zeeman shift of the atom's resonance frequency, the central core is predicted to have a ratio of 1:2 between the sizes of the axes of the ellipsoidal atomic spatial distribution. The diffuse outer region was not expected to contribute significantly to the signal and was neglected. The 1:2 axes size ratio was assumed for the central core and allowed us to make significant simplifications to the calculation.

At the smallest trap laser beam detunings used in the experiment, the results of fitting the theory to the data indicated that the 1:2 size ratio that was assumed for the axes may not be valid. For larger detuning, the theory began to fit the data better. This may indicate that the density of the central core only dominates the signal at the larger detuning or that the two component regime is just beginning to form. Future analysis of the data using different or less rigid forms for the atomic density may yield answers to these questions.

In addition, other regimes of high density MOT operation have shown tendencies to yield non-Gaussian spatial distributions [37,41]. Due to forces that arise from multiple photon scattering events among the trapped atoms, the density of atoms reaches a maximum. Once the maximum density of atoms is reached, adding atoms to the trap only increases its size. As a result, the center of the trap has a uniform density distribution. Using fluorescent imaging, two groups have detected this type of spatial distribution [37, 41] under limited conditions. Because optical thickness limits the ability of the fluorescent techniques to observe the atoms in this regime, the ability of the resonance imaging technique to probe thick samples should be useful in exploring this system.

7.2 Future of Raman Imaging in Traps

While Raman induced resonance imaging is a viable technique for rapidly recyclable traps like the MOT, in many traps, imaging the spatial distribution by scanning the Raman difference frequency would be problematic. Some traps require multiple cooling processes and may require more than a second to recycle. Unfortunately, the recycling would most likely need to occur between each scan point to eliminate perturbations in the spatial distribution that are caused by the measurement process. The low duty cycle of many traps recycling in this manner and the variations of the trap between scan points would create a tedious and ambiguous measurement process.

So instead of using a scanning Raman difference frequency for measurements in traps, we are developing a pulsed method for imaging the entire distribution in a single shot. Perturbations during the measurement process will still disturb the trap significantly and in some cases destroy it, but this single-shot method will image the entire collection of atoms before the perturbations significantly affect the spatial distribution.

As in the resonance imaging method, atoms are prepared in an initial state with a spatially varying Raman transition frequency to a final state. However, when the Raman pulse is applied to the sample, the goal is not to transfer the population from the initial to the final state as in resonance imaging, but to create a superposition, or *coherence*, between those two states. By using a short Raman pulse with enough bandwidth and the appropriate intensity, a coherence can be created over the entire sample, regardless of an atom's particular transition frequency. After the pulse, the Raman coherence of each atom oscillates at it's particular resonance frequency.

In the absence of the potential energy gradient, the transition frequencies would be identical for all the atoms, and the coherence from atom to atom would remain in phase. However, the presence of the potential energy gradient causes the transition frequencies to differ in a spatially dependent manner. Thus, the coherence from atom to atom will dephase after a time corresponding to the bandwidth of the transition frequencies in the sample.

The coherences in the sample may be detected by using a weak probe beam. Consider the energy level diagram in Figure 7.1. The Raman coherence of atoms in the sample oscillates at $\omega_0(x)$. If a weak probe at frequency ω_1 illuminates the sample and excites the $|i\rangle$ to $|I\rangle$ transitions, the atoms

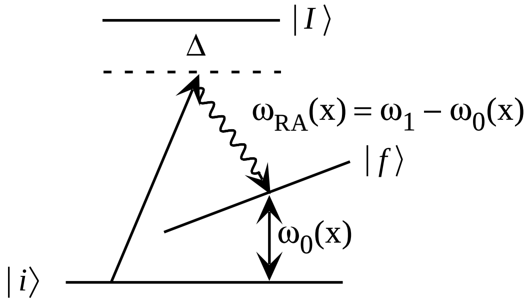

Figure 7.1: The energy level diagram for Raman transient imaging.

radiate at frequencies given by $\omega_{RA}(x) = \omega_1 - \omega_0(x)$.

Because the radiation from the atoms is oscillating at optical frequencies, a technique called heterodyne detection must be used to measure the frequency distribution of the radiation. A schematic of heterodyne detection is shown in Figure 7.2. The radiation from the atoms is mixed with another laser beam called the local oscillator. After mixing, a fraction of the electric field from the atomic radiation and fraction from the local oscillator, E_{LO}, propagate together toward the detector. Since the resonance frequency for the atoms varies in space, the atoms radiate a sum of electric fields with different frequencies. The electric field from the atomic radiation that propagates toward the detector after mixing with the local oscillator is given by $\sum_{RA} E_{RA} \cos \omega_{RA} t$.

At the detector, the intensity I of the sum of both fields goes as

$$I \propto \langle | \sum_{RA} E_{RA} \cos \omega_{RA} t + E_{LO} \cos \omega_{LO} t |^2 \rangle \tag{7.1}$$

where the outer brackets indicate averaging over a few optical periods. Eval-

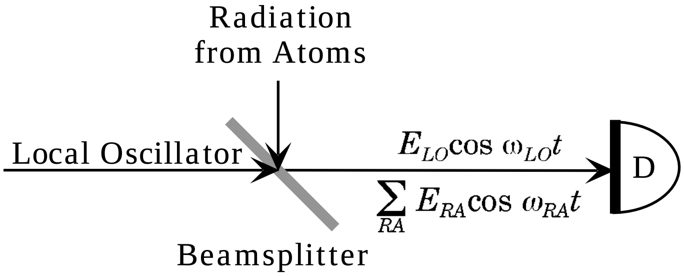

Figure 7.2: A schematic for optical heterodyne detection.

uation of the intensity leads to a term which is proportional to

$$\sum_{RA} E_{RA}E_{LO}\cos(\omega_{RA}-\omega_{LO})t. \tag{7.2}$$

If the frequency of the local oscillator is chosen so that the $(\omega_{RA}-\omega_{LO})$ are within the bandwidth of the detector, these oscillating terms will be detected. Thus, the intensity at the detector will contain frequencies corresponding to the atoms at each location in the distribution. The Fourier transform of the time dependent intensity yields the spatial distribution of the atoms.

If one were to measure the intensity of the atomic radiation without interfering it with the local oscillator, a time dependent intensity would still be obtained and is given by $I \propto \langle|\sum_{RA} E_{RA}\cos\omega_{RA}t|^2\rangle$. This signal is called a free induction decay signal. Figure 7.3 shows the free induction decay signal of atoms loaded into the MOT. Although the atomic spatial distribution cannot be obtained from this signal, its presence indicates that atoms are radiating coherently. This coherent radiation is a necessary requirement for transient imaging with heterodyne detection to be successful. The applica-

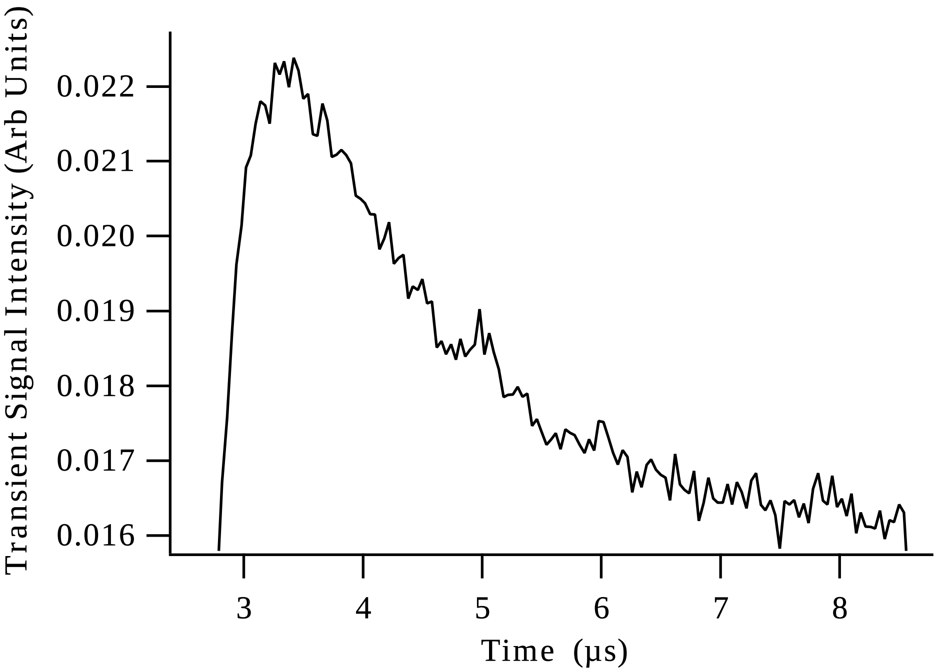

Figure 7.3: The free-induction decay signal from atoms loaded into the MOT.

tion of the heterodyne technique to the coherent radiation detected in the free induction decay signal is currently being developed.

In Raman induced transient imaging, instead of sampling the distribution by scanning the Raman difference frequency, the entire distribution is measured in a single shot. Consequently, developing this technique should prove useful for imaging atoms in traps where there is not a well defined steady state distribution and in traps that cannot be quickly recycled. For example, in addition to the interesting steady state behavior of the MOT at high densities which could be explored by resonance imaging, MOT's occasionally demonstrate intriguing time-dependent behavior. Researchers have intentionally misaligned the MOT trapping beams to create rotating clumps of atoms around a central core [37, 38, 40]. The transient imaging technique which takes a snapshot of the atoms is ideally suited for studying the dynamics of non-stationary spatial distributions.

The high resolution attainable by Raman imaging techniques makes their continued development particularly important. In a resonance imaging experiment performed by our group on an atomic beam, sub-optical resolution of 200 nm was obtained [53]. In some trapping experiments, atomic spatial patterns vary on sub-optical wavelength scales. In optical lattices, for example, where the atoms are confined to the periodic potentials formed by optical [24, 25] and infrared [26] standing waves, the entire distribution of atoms is close to, if not, sub-optical. Consequently, probing the shape of the distribution requires the ultra-high resolution attainable by Raman induced imaging.

The Raman induced resonance imaging technique developed in this dissertation will serve as the foundation for additional resonance experiments as well as the transient techniques under development. Future applications of Raman imaging techniques that we hope to explore include further studies of the magneto-optic trap, imaging of atoms in a one-dimensional optical lattice, the characterization of cold lithium fermions in a CO_2 laser trap, and single shot correlation measurements of quantum degenerate atoms.

Appendix A

The Transition Dipole Moments

Calculating the arbitrary dipole moment

$$\langle (J', I = 1)F', m_{F'}|\mu_q^1|(J = 1/2, I = 1)F, m_F\rangle$$

requires using a combination of the Wigner-Eckart Theorem [61]:

$$\begin{aligned}&\langle n'(J'I)F', m_{F'}|\mu_q^1|n(JI)F, m_F\rangle \\ &\qquad = (-1)^{F'-m_{F'}} \begin{pmatrix} F' & 1 & F \\ -m_{F'} & q & m \end{pmatrix} \langle n'(J'I)F'\|\mu^1\|n(JI)F\rangle \quad \text{(A.1)}\end{aligned}$$

and six-J symbol momentum recoupling relations. The Wigner-Eckart Theorem allows one to calculate dipole moments for different $m_{F'}$, and m_F between a set of fixed J', J, F', and F.

To determine the dipole moments between $F' = 5/2$ and $F = 3/2$ in the D_2 line, we first calculate the reduced matrix element using (3.6) and (A.1).

For now, n', n, and $I = 1$ are omitted for brevity:

$$\begin{aligned}
&\langle (J' = 3/2)F' = 5/2 \| \mu^1 \| (J = 1/2)F = 3/2 \rangle \\
&= (-1)^{\frac{5}{2}-\frac{5}{2}} \frac{\langle (J' = \frac{3}{2})F' = \frac{5}{2}, m_{F'} = \frac{5}{2} | \mu^1_1 | (J = \frac{1}{2})F = \frac{3}{2}, m_F = \frac{3}{2} \rangle}{\begin{pmatrix} \frac{5}{2} & 1 & \frac{3}{2} \\ \frac{-5}{2} & 1 & \frac{3}{2} \end{pmatrix}} \qquad \text{(A.2)} \\
&= \sqrt{6}\, \mu_0.
\end{aligned}$$

Once we have the reduced matrix element, we reapply (A.1) to determine the other matrix elements between $F' = 5/2$ and $F = 3/2$. For example,

$$\begin{aligned}
&\langle (J' = \frac{3}{2})F' = \frac{5}{2}, m_{F'} = -\frac{1}{2} | \mu^1_{-1} | (J = \frac{1}{2})F = \frac{3}{2}, m_F = \frac{1}{2} \rangle \\
&= (-1)^{\frac{5}{2}-\frac{-1}{2}} \begin{pmatrix} \frac{5}{2} & 1 & \frac{3}{2} \\ \frac{1}{2} & -1 & \frac{1}{2} \end{pmatrix} \langle (J' = 3/2)F' = 5/2 \| \mu^1 \| (J = 1/2)F = 3/2 \rangle \\
&= \frac{1}{\sqrt{20}} \sqrt{6}\, \mu_0 = \sqrt{\frac{3}{10}}\, \mu_0
\end{aligned} \qquad \text{(A.3)}$$

Only half of the matrix elements must be calculated since for ^{6}Li and other spin-1/2 particles:

$$\langle F', m_{F'} | \mu^1_q | F, m_F \rangle = r \langle F', -m_{F'} | \mu^1_{-q} | F, -m_F \rangle \qquad \text{(A.4a)}$$

$$r = (-1)^{F'+F}. \qquad \text{(A.4b)}$$

Once calculated, the magnitudes of the matrix elements may be checked using the sum-rule

$$\sum_{m_{F'},m_F} |\langle F', m_{F'}|\mu^1_q|F, m_F\rangle|^2 = \frac{|\langle F'\|\mu^1_q\|F\rangle|^2}{3} \tag{A.5}$$

for each $q = 0, \pm 1$. All of the matrix elements we calculated were tested with this sum rule.

For the other F' and F elements, we can use the following six-J reduction [61]:

$$\begin{aligned} &\langle (J'I)F'\|\mu^1\|(JI)F\rangle \\ &\qquad = (-1)^{J'+I+F+1}\sqrt{(2F'+1)(2F+1)} \begin{Bmatrix} J' & I & F' \\ F' & 1 & J \end{Bmatrix} \langle J'\|\mu^1\|J\rangle. \end{aligned} \tag{A.6}$$

This reduces the dipole moment matrix element to the J-basis so that all the D_2 matrix elements are calculable. Using the result of (A.2) we can solve for $\langle J'\|\mu^1\|J\rangle$ and use it to calculate the remaining F-basis reduced matrix elements.

The J-basis reduced matrix element can be further reduced to the L-basis by using (A.6). This then allows the calculation of the D_1 matrix elements. The results of the entire calculation are presented in Figures 3.3 and 3.4 on pages 57 and 58.

Bibliography

[1] S. Chu, L. Hollberg, J.E. Bjorkholm, A. Cable, and A. Ashkin. Three-dimensional viscous confinement and cooling of atoms by resonance radiation pressure. *Phys. Rev. Lett.*, 55:48–51, 1985.

[2] W. D. Philips and H. Metcalf. Laser deceleration of an atomic beam. *Phys. Rev. Lett.*, 8:596–9, 1982.

[3] J. V. Prodan, W. D. Philips, and H. Metcalf. Laser production of a very slow monoenergetic atomic beam. *Phys. Rev. Lett.*, 49:1149–53, 1982.

[4] A. L. Migdall, J. V. Prodan, W. D. Phillips, T. H. Bergeman, and H. J. Metcalf. First observation of magnetically trapped neutral atoms. *Phys. Rev. Lett.*, 54:2596–9, 1985.

[5] W. D. Phillips, J. V. Prodan, and H. J. Metcalf. Laser cooling and electromagnetic trapping of neutral atoms. *J. Opt. Soc. Am. B*, 2:1751–67, 1985.

[6] P. D. Lett, R. N. Watts, C. I. Westbrook, W. D. Phillips, P. L. Gould, and H. J. Metcalf. Observation of atoms laser cooled below the doppler limit. *Phys. Rev. Lett.*, 61:169–72, 1988.

[7] P. D. Lett, W. D. Phillips, S. L. Rolston, C. E. Tanner, R. N. Watts, and C. I. Westbrook. Optical molasses. *J. Opt. Soc. Am. B*, 6:2084–107, 1989.

[8] S. Chu, J. E. Bjorkholm, A. Ashkin, and A. Cable. Experimental observation of optically trapped atoms. *Phys. Rev. Lett.*, 57:314–17, 1986.

[9] E. L. Raab, M. Prentiss, A. Cable, S. Chu, and D. E. Pritchard. Trapping of neutral sodium atoms with radiation pressure. *Phys. Rev. Lett.*, 59:2631–4, 1987.

[10] D. S. Weiss, E. Riis, Y. Shevy, P. J. Ungar, and S. Chu. Optical molasses and multilevel atoms: experiment. *J. Opt. Soc. Am. B*, 6:2072–83, 1989.

[11] P. J. Ungar, D. S. Weiss, E. Riis, and S. Chu. Optical molasses and multilevel atoms: theory. *J. Opt. Soc. Am. B*, 6:2058–71, 1989.

[12] M. Kasevich and S. Chu. Laser cooling below a photon recoil with three-level atoms. *Phys. Rev. Lett.*, 69:1741–4, 1992.

[13] K. E. Gibble, S. Kasapi, and S. Chu. Improved magneto-optic trapping in a vapor cell. *Opt. Lett.*, 17:526–8, 1992.

[14] J. Dalibard and C. Cohen-Tannoudji. Laser cooling below the doppler limit by polarization gradients: simple theoretical models. *J. Opt. Soc. Am. B*, 6:2023–45, 1989.

[15] A. Aspect, E. Arimondo, R. Kaiser, N. Vansteenkiste, and C. Cohen-Tannoudji. Laser cooling below the one-photon recoil energy by velocity- selective coherent population trapping: theoretical analysis. *J. Opt. Soc. Am. B*, 6:2112–24, 1989.

[16] M. H. Anderson, J. R. Ensher, M. R. Matthews, C. E. Wieman, and E. A. Cornell. Observation of Bose-Einstein condensation in a dilute atomic vapor. *Science*, 269:198–201, 1995.

[17] K. B. Davis, M.-O. Mewes, M. R. Andrews, N. J. van Druten, D. S. Durfee, D. M. Kurn, and W. Ketterle. Bose-Einstein condensation in a gas of sodium atoms. *Phys. Rev. Lett.*, 75:3969–73, 1995.

[18] C. C. Bradley, C. A. Sackett, J. J. Tollett, and R. G. Hulet. Evidence of Bose-Einstein condensation in an atomic gas with attractive interactions. *Phys. Rev. Lett.*, 75:1687–90, 1995.

[19] C. C. Bradley, C. A. Sackett, and R. G. Hulet. Bose-Einstein condensation of lithium: observation of limited condensate number. *Phys. Rev. Lett.*, 78:985–9, 1997.

[20] M. R. Andrews, D. S. Durfee, S. Inouye, D. M. Stamper-Kurn, H.-J. Miesner, and W. Ketterle. Studies of Bose-Einstein condensates. *J. Low Temp. Phys.*, 110:153–66, 1998.

[21] C. E. Wieman. The creation and study of Bose-Einstein condensation in a dilute atomic vapour. *Philosophical Transactions of the Royal Society London, Series A*, 355:2247–57, 1997.

[22] K. Burnett, editor. *Ultracold Atoms and Bose-Einstein Condensation*, volume 7 of *OSA Trends in Optics and Photonics Series.* Optical Society of America, Washington, D.C., 1996.

[23] M.-O. Mewes, M. R. Andrews, D. M. Kurn, D. S. Durfee, C. G. Townsend, and W. Ketterle. Output coupler for Bose-Einstein condensed atoms. *Phys. Rev. Lett.*, 78:582–5, 1997.

[24] G. Grynberg and C. Triché. Atoms in optical lattices. In Aspect et al. [88], pages 246–84.

[25] A. Hemmerich, M. Weidemüller, and T. W. Hänsch. Atomic lattices bound by light. In Aspect et al. [88], pages 503–28.

[26] S. Friebel, C. D'Andrea, J. Walz, M. Weita, and T. W. Hänsch. CO_2-laser optical lattice with cold rubidium atoms. *Phys. Rev. A*, 57:R20–3, 1998.

[27] C. S. Adams and E. Riis. Laser cooling and trapping of neutral atoms. *Prog. Quant. Electr.*, 21:1–79, 1997.

[28] Z.-T. Lu, K. L. Corwin, K. R. Vogel, C. E. Wieman, T. P. Dinneen, J. Maddi, and H. Gould. Efficient collection of ^{221}Fr into a vapor cell magneto-optical trap. *Phys. Rev. Lett.*, 79:994–7, 1997.

[29] W. Z. Zhao, J. E. Simsarian, L. A. Orozco, W. Shi, and G. D. Sprouse. Measurement of the 7p $^2P_{3/2}$ level lifetime in atomic francium. *Phys. Rev. Lett.*, 78:4169–72, 1997.

[30] J.I. Cirac, M. Lewenstein, and P. Zoller. Quantum statistics of a laser cooled ideal gas. *Phys. Rev. A*, 72:2977–80, 1994.

[31] D.A. Butts and D.S. Rokhsar. Trapped fermi gases. *Phys. Rev. A*, 55:4346–50, 1997.

[32] L.I. Plimak and D.F. Walls. Nonclassical spatial and momentum distributions in a bose- condensed gas. *Phys. Rev. A*, 54:652–5, 1996.

[33] J. Schneider and H. Wallis. Mesoscopic Fermi gas in a harmonic trap. *Phys. Rev. A*, 57:1253–9, 1998.

[34] J. E. Thomas. Measuring the position of moving atoms with uncertainty-principle-limited precision. *Contemporary Physics*, 35:257–67, 1994.

[35] J. E. Thomas and L. J. Wang. Precision position measurement of moving atoms. *Phys. Rep.*, 262:311–66, 1995.

[36] J. E. Thomas and L. J. Wang. Quantum theory of correlated-atomic-position measurements by resonance imaging. *Phys. Rev. A*, 49:558–69, 1994.

[37] D. W. Sesko, T. G. Walker, and C. E. Wieman. Behavior of neutral atoms in a spontaneous force trap. *J. Opt. Soc. Am. B*, 8:946–58, 1991.

[38] T. Walker, D. Sesko, and C. Wieman. Collective behavior of optically trapped neutral atoms. *Phys. Rev. Lett.*, 64:408–11, 1990.

[39] K. Lindquist, M. Stephens, and C. Wieman. Experimental and theoretical study of the vapor-cell Zeeman optical trap. *Phys. Rev. A*, 46:4082–90, 1992.

[40] V. S. Bagnato, L. G. Marcassa, M. Oria, G. I. Surdutovich, R. Vitlina, and S. C. Zilio. Spatial distribution of atoms in a magneto-optical trap. *Phys. Rev. A*, 48:3771–5, 1993.

[41] C. G. Townsend, N. H. Edwards, C. J. Cooper, K. P. Zetie, C. J. Foot, A. M. Steane, P. Szriftgiser, H. Perrin, and J. Dalibard. Phase-space density in the magneto-optical trap. *Phys. Rev. A*, 52:1423–40, 1995.

[42] J. A. Kim, K. I. Lee, H. R. Noh, W. Jhe, and M. Ohtsu. Atom trap in an axicon mirror. *Opt. Lett.*, 22:117–19, 1997.

[43] W. Petrich, M. H. Anderson, J. R. Ensher, and E. A. Cornell. Behavior of atoms in a compressed magneto-optic trap. *J. Opt. Soc. Am. B*, 11:1332–5, 1994.

[44] W. Ketterle, K. B. Davis, M. A. Joffe, A. Martin, and D. E. Pritchard. High densities of cold atoms in a dark spontaneous-force optical trap. *Phys. Rev. Lett.*, 70:2253, 1993.

[45] J. Werver, H. Wallis, and W. Ertmer. Atoms with anomalous zeeman effect in a 1d-magneto-optical molasses. *Optics Communications*, 94:525–9, 1992.

[46] A. M. Steane, G. Hillenbrand, and C. J. Foot. Polarization gradient cooling in a one-dimensional $\sigma^+ - \sigma^-$ configuration for any atomic transition. *J. Phys. B: At. Mol. Opt. Phys.*, 25:4721–43, 1992.

[47] E. Hecht. *Optics*. Addison-Wesley, Reading, MA, third edition, 1998.

[48] M. R. Andrews, M.-O. Mewes, N. J. Van Druten, D. S. Durfee, D. M. Kum, and W. Ketterle. Direct, nondestructive observation of a Bose condensate. *Science*, 273:84–7, 1996.

[49] M. R. Andrews, C. G. Townsend, H.-J. Miesner, D. S. Durfee, D. M. Kurn, and W. Ketterle. Observation of interference between two Bose condensates. *Science*, 275:637–41, 1997.

[50] K. Helmerson, A. Martin, and D. E. Pritchard. Laser and rf spectroscopy of mangetically trapped neutral atoms. *J. Opt. Soc. Am. B*, 9:483–92, 1992.

[51] V. Vuletic, T. Fischer, M. Praeger, T. W. Hänsch, and C. Zimmermann. Microscopic magnetic quadrupole trap for neutral atoms with extreme adiabatic compression. *Phys. Rev. Lett.*, 80:1634–7, 1998.

[52] K. D. Stokes, C. Schnurr, J. R. Gardner, M. Marable, G. R. Welch, and J. E. Thomas. Precision position measurement of moving atoms using optical fields. *Phys. Rev. Lett.*, 67:1997–2000, 1991.

[53] J. R. Gardner, M. L. Marable, G. R. Welch, and J. E. Thomas. Suboptical wavelength position measurement of moving atoms using optical fields. *Phys. Rev. Lett.*, 70:3404–7, 1993.

[54] M. L. Marable, T. A. Savard, and J. E. Thomas. Adaptive atom-optics in atom interferometry. *Opt. Comm.*, 135:14–18, 1997.

[55] J. E. Thomas. Uncertainty-limited position measurement of moving atoms using optical fields. *Opt. Lett.*, 14:1186–8, 1989.

[56] J. E. Thomas. Quantum theory of atomic position measurement using optical fields. *Phys. Rev. A*, 42:5652–66, 1990.

[57] J. R. Gardner. *Ultra-High Resolution Atom Imaging in a Light-Shift Gradient.* PhD thesis, Duke University, 1993.

[58] C. Cohen-Tannoudji, J. Dupont-Roc, and G. Grynberg. *Atom-Photon Interactions: Basic Processes and Applications.* John Wiley & Sons, New York, 1992.

[59] M. L. Marable. *Adaptive Resonance Imaging and All-Optical Interferometry.* PhD thesis, Duke University, 1995.

[60] G. R. Welch. Private communication.

[61] A. R. Edmonds. *Angular Momentum in Quantum Mechanics.* Princeton University Press, Princeton, NJ, 1974.

[62] C. Monroe, W. Swann, H. Robinson, and C. Wieman. Very cold trapped atoms in a vapor cell. *Phys. Rev. Lett.*, 65:1571–4, 1991.

[63] Z. Lin, K. Shimizu, M. Zhan, F. Shimizu, and H. Takuma. Laser cooling and trapping of Li. *Jpn. J. Appl. Phys.*, 30:L1324–6, 1991.

[64] A. N. Nesmeyanov. *Vapor Pressure of the Chemical Elements.* Elsevier Publishing Company, Amsterdam, 1963.

[65] R. Hulet. Private communication.

[66] L. Vályi. *Atom and Ion Sources.* Wiley, New York, 1977.

[67] G. Scoles. *Atomic and Molecular Beam Methods.* Oxford University Press, New York, 1987.

[68] J. H. Moore, C. C. Davis, and M. A. Coplan. *Building Scientific Apparatus: A Practical Guide to Design and Construction.* Addison-Wesley Publishing Company, Reading, MA, 1989.

[69] Varian Vacuum Products. *Varian Vacuum Products Catalog*, 1995-96.

[70] Coherent Laser Group, Palo Alto. *Operator's Manual: The Coherent INNOVA 310/320 Series Ion Laser*, 1990.

[71] Coherent Laser Division, Palo Alto. *Coherent CR-699-21 Ring Dye Laser Manual*, 1981.

[72] Coherent Laser Corp., Palo Alto. *Coherent CR-699-21/03 Scientific Service Manual*, 1980.

[73] P. Hammond and D. Cooke. Continuous-wave dye lasers in the DCM region. *Appl. Opt.*, 31:7095–9, 1992. In this paper, LD688 dye is referred to as D3.

[74] H. Concannon. *Two-Photon Raman Gain in a Laser-Driven Potassium Vapor.* PhD thesis, Duke University, 1996.

[75] D. Sukow. *Experiment Control of Instabilities and Chaos in Fast Dynamical Systems.* PhD thesis, Duke University, 1997.

[76] V. S. Letokhov and V. G. Minogin. Laser radiation pressure on free atoms. *Phys. Rep.*, 73:1–65, 1981.

[77] H. Metcalf and P. van der Straten. Cooling and trapping of neutral atoms. *Phys. Rep.*, 244:203–86, 1994.

[78] C. J. Foot. Laser cooling and trapping of atoms. *Contemporary Physics*, 32:369–81, 1991.

[79] V. I. Balykin, V. S. Letokhov, and V. I. Mushin. Observation of free Na atom cooling in a resonant laser field at scanning frequency. *JETP Lett.*, 29:560–4, 1979.

[80] W. Ertmer, R. Blatt, J. L. Hall, and M. Zhu. Laser manipulation of atomic beam velocities: Demonstration of stopped atoms and velocity reversal. *Phys. Rev. Lett.*, 54:996–9, 1985.

[81] C. A. Baird. Design and characterization of a multi-coil Zeeman slower. Master's thesis, Duke University, 1996.

[82] M. R. Spiegel. *Mathematical Handbook of Formulas and Tables.* Schaum's Outline Series. McGraw-Hill Book Company, New York, 1968.

[83] R. Serway. *Physics for Scientists and Engineers—with Modern Physics.* Saunders College Publishing, Fort Worth, third edition, 1990.

[84] W. H. Press et. al. *Numerical Recipes in C: The Art of Scientific Computing.* Cambridge University Press, New York, second edition, 1992.

[85] X. Hui-Rong, S. V. Benson, and T. W. Hänsch. A 'toy train' wavemeter. *Laser Focus*, 55, 1981.

[86] T. Bergman, G. Erez, and H.J. Metcalf. Magnetostatic trapping fields for neutral atoms. *Phys. Rev. A*, 35:1535– 46, 1987.

[87] G. Arfken. *Mathematical Methods for Physicists.* Academic Press, New York, third edition, 1985.

[88] A. Aspect, W. Barletta, and R. Bonifacio, editors. *Coherent and Collective Interactions of Particles and Radiation Beams*, Proceedings of the International School of Physics Enrico Fermi. Italian Physical Society, 1995.

Biography

Thomas Alan Savard was born in Edina, Minnesota on June 30, 1969. He grew up in Apple Valley and Brooklyn Park, Minnesota and graduated from Osseo Senior High School in 1987. He majored in physics at St. John's University in Collegeville, Minnesota and graduated *Egregia Cum Laude* in 1991 with All-College Honors with Distinction in Physics. In the fall of 1991, he enrolled in the graduate physics program at Duke University with a Townes-Perkin Elmer Fellowship. While at Duke, he also received the Walter Gordy Fellowship for his work in optical physics under the direction of Professor John E. Thomas. His research at Duke University focused on developing techniques for imaging ultracold atomic vapors. In 1994, he married Lynda, whom he had met while attending St. John's University. He received his A.M. in 1995 and a Ph.D. in 1998, both in Physics.

Publications

T. A. Savard, K. M. O'Hara, S. R. Granade, M. E. Gehm, J. E. Thomas. Raman Induced Magnetic Resonance Imaging of Trapped Atoms in a MOT, 1998 Annual Meeting of the Division of Atomic, Molecular, and Optical Physics (DAMOP) (May 1998)

T.A. Savard, K.M. O'Hara, and J.E. Thomas. Laser-noise-induced heating in far-off resonance optical traps. *Physical Review A*, 56(2):R1095–8, 1997.

T. A. Savard, K. M. O'Hara, and J. E. Thomas. Laser Noise Induced Heating in Far Off Resonance Optical Traps, conference on Quantum Electronics and Laser Science QELS ' 97 (May 1997)

T. A. Savard, C. A. Baird, K. M. O'Hara and J. E. Thomas. A Multi-coil Zeeman Slower, conference on Quantum Electronics and Laser Science QELS ' 97 (May 1997)

M.L. Marable, T.A. Savard, and J.E. Thomas. Adaptive atom-optics in atom interferometry. *Optics Communications*, 135(1-3):14–18, 1997.

C. Schnurr, T.A. Savard, L.J. Wang, and J.E. Thomas. Atomic wavefunction imaging via optical coherence. *Physical Review Letters*, 74(8):1331–4, 1995.

C. Schnurr, T. Savard, L.J. Wang, and J.E. Thomas. Detection of atomic interference through collective radiation. *Optics Letters*, 20(4):413–15, 1995.

M. L. Marable, T. A. Savard, and J. E. Thomas. Adaptive Imaging of Atomic Interference Patterns, conference on Quantum Electronics and Laser Science QELS ' 95, Technical Digest Series 16, 156 (May, 1995)

Z. Pan, T. Savard, and J.P. Wicksted. Raman studies of crystalline and amorphous poly(p-phenylene sulfide) films. *Journal of Raman Spectroscopy*, 23(11):615–19, 1992.

T. Savard, Z. Pan, J. P. Wicksted. Raman Spectroscopy of Amorphous and Crystalline Poly-(p-phenylene sulfide), Meeting of the American Physical Society, San Antonio, TX (January 1991)